



HAL
open science

The numerics of hydrostatic structured-grid coastal ocean models: state of the art and future perspectives

Knut Klingbeil, Florian Lemarié, Laurent Debreu, Hans Burchard

► To cite this version:

Knut Klingbeil, Florian Lemarié, Laurent Debreu, Hans Burchard. The numerics of hydrostatic structured-grid coastal ocean models: state of the art and future perspectives. *Ocean Modelling*, 2018, 10.1016/j.ocemod.2018.01.007 . hal-01443357v2

HAL Id: hal-01443357

<https://inria.hal.science/hal-01443357v2>

Submitted on 5 Feb 2018 (v2), last revised 5 Feb 2018 (v3)

HAL is a multi-disciplinary open access archive for the deposit and dissemination of scientific research documents, whether they are published or not. The documents may come from teaching and research institutions in France or abroad, or from public or private research centers.

L'archive ouverte pluridisciplinaire **HAL**, est destinée au dépôt et à la diffusion de documents scientifiques de niveau recherche, publiés ou non, émanant des établissements d'enseignement et de recherche français ou étrangers, des laboratoires publics ou privés.

The numerics of hydrostatic structured-grid coastal ocean models: state of the art and future perspectives

Knut Klingbeil^a Florian Lemarié^b Laurent Debreu^b
Hans Burchard^c

^a*Dept. of Mathematics, University of Hamburg, Germany*

^b*Inria, Univ. Grenoble Alpes, CNRS, LJK, Grenoble F-38000, France*

^c*Leibniz Institute for Baltic Sea Research Warnemünde, Seestraße 15, D-18119 Rostock, Germany*

Abstract

The state of the art of the numerics of hydrostatic structured-grid coastal ocean models is reviewed here. First, some fundamental differences in the hydrodynamics of the coastal ocean, such as the large surface elevation variation compared to the mean water depth, are contrasted against large scale ocean dynamics. Then the hydrodynamic equations as they are used in coastal ocean models as well as in large scale ocean models are presented, including parameterisations for turbulent transports. As steps towards discretisation, coordinate transformations and spatial discretisations based on a finite-volume approach are discussed with focus on the specific requirements for coastal ocean models. As in large scale ocean models, splitting of internal and external modes is essential also for coastal ocean models, but specific care is needed when wetting and drying of intertidal flats is included. As one obvious characteristics of coastal ocean models, open boundaries occur and need to be treated in a way that correct model forcing from outside is transmitted to the model domain without reflecting waves from the inside. Here, also new developments in two-way nesting are presented. Single processes such as internal inertia-gravity waves, advection and turbulence closure models are discussed with focus on the coastal scales. Some overview on existing hydrostatic structured-grid coastal ocean models is given, including their extensions towards non-hydrostatic models. Finally, an outlook on future perspectives is made.

Key words: coastal ocean models, hydrostatic models, adaptive coordinates, mode splitting, wetting and drying, two-way nesting

1 Introduction

This review paper presents the state of the art numerics of the hydrodynamic cores of coastal ocean models, with focus on structured-grid hydrostatic models. Here, we define the coastal ocean as ranging from estuaries and shallow coastal areas to the shelf break region. On the small scale end, near-shore

5 (e.g., Stockdon et al., 2006) and coastal engineering (Rennau et al., 2012) scales are not resolved, but
6 parameterised, if needed. On the large scale end, the dynamics of the ocean basins will not be explicitly
7 treated, since their effects are introduced by means of lateral boundary conditions (see, e.g., Holt et al.
8 (2009)).

9 The coastal ocean as defined here, is strongly affected by the superposition of direct human impacts
10 and climate change and variability (Halpern et al., 2008). Direct human impacts include for example
11 eutrophication (Conley et al., 2009), fishery (Jackson et al., 2001), large scale constructions (such as
12 offshore wind farms (Carpenter et al., 2016)), dredging and dumping of material (Winterwerp et al., 2013),
13 discharges (e.g., of cooling water (Hofmeister et al., 2013)) and pollution (Gao and Chen, 2012). Aspects
14 of natural and anthropogenic climate change and variability impacting on the coastal ocean are relative sea
15 level rise (global and local, e.g., Wahl et al. (2013)), global warming (e.g., Wiltshire and Manly, 2004),
16 changes of the water cycle (precipitation, evaporation, run-off, e.g., Meier et al. (2006)), and changed wind
17 forcing (e.g., Sydeman et al., 2014). These local, regional and global forcings may lead to severe changes
18 in the coastal environment, such as coastal erosion (Feagin et al., 2005), flooding of low-laying coastal
19 regions (Nicholls et al., 1999), increase of oxygen minimum zones (Diaz and Rosenberg, 2008), shifts in
20 biodiversity and invasion of alien species (Lotze et al., 2006), and many more. Changes are strong in many
21 coastal regions around the world (see, e.g., BACC II Author Team (2015) for the Baltic Sea and Quante
22 and Colijn (2016) for the North Sea), but specifically serious in the Arctic where the warming is strongly
23 accelerated (Screen and Simmonds, 2010).

24 Coastal ocean models can be applied on various scales to simulate scenarios to test management op-
25 tions, such as for example for nutrient reduction experiments (Neumann et al., 2002; Lenhart et al., 2010),
26 or for coastal engineering scenarios (Rennau et al., 2012; Van Maren et al., 2016).

27 To understand the changing coastal oceans, numerical modelling is one of the most effective tools,
28 allowing for reconstructions of historic states, hindcasts and analysis of the dynamics in the last decades,
29 short term forecasts of coastal ocean states, as well as for coastal climate projections and possible fu-
30 ture scenarios. One core requirement for the predictability of such model exercises is the way how basic
31 hydrodynamic processes are reproduced.

32 Main aspects which need to be resolved are exchanges of matter (such as salt, heat, oxygen, nutrients
33 and particulate matter) in vertical and lateral directions. In the lateral direction, the coast-to-ocean ex-
34 change is mediated by estuarine dynamics, tidal dispersion, tidal fronts, river plumes, and meso-scale and
35 submeso-scale dynamics (see, e.g., Huthnance (1995); Wheless and Klinck (1995); Capet et al. (2008);
36 Horner-Devine et al. (2015); Burchard and Badewien (2015)). In the vertical, critical interfaces play a cru-
37 cial role, such as the sediment-water interface, the *clines* (lucloine, halocline, thermocline, redoxcline),
38 the surface and bottom wave-affected layers as well as the air-sea interface (Ross and Mehta, 1989; Bur-
39 chard et al., 2008). Internal waves play a special role for linking horizontal and vertical scales (Scotti and
40 Pineda, 2004). All these features need to be properly resolved.

41 In this paper, we discuss specific requirements for models of the coastal ocean. The coupling of the hy-
42 drodynamic core with models for other compartments such as atmospheric models, surface wave models,
43 sea ice models, hydrological models and bottom sediment models is not discussed in detail, as each of these
44 topics deserves and requires an in-depth review on its own. Scales where resolution of non-hydrostatic
45 effects become relevant will be parameterised such that we focus on hydrostatic models. The inclusion of
46 the non-hydrostatic pressure contribution into an existing hydrostatic kernel is outlined. Furthermore, we
47 restrict ourselves to the class of structured-grid models, since the numerical methods in unstructured-grid
48 modelling differ significantly from the structured-grid methods. Due to their flexible grids, unstructured-

49 grid models are known to be specifically suitable for investigating multi-scale dynamics in the ocean. We
50 will here discuss how also structured-grid models combined with nesting strategies are able to resolve
51 multiple scales.

52 The paper is structured as follows: After this introduction, the specific properties of the coastal ocean
53 are discussed in section 2. The class of mathematical equations on which coastal ocean models are gener-
54 ally based is presented in section 3, including momentum and tracer equations (section 3.1) and turbulence
55 closures (section 3.2). Based on these equations, the most common coordinate transformations and related
56 spatial discretisation methods are introduced (section 4), while temporal discretisation including mode
57 splitting and wetting and drying is presented in section 5. Section 6 is then dedicated to open boundary
58 conditions and model nesting. The numerical treatment of single processes is discussed in section 7. Fi-
59 nally, the most common coastal ocean community models are presented in section 8 and an outlook is
60 given in section 9.

61 **2 Characteristics of coastal ocean dynamics**

62 The coastal ocean has a number of characteristics which discriminate it from the global ocean in a
63 way that specific physical and numerical treatment is required. In the following, these characteristics are
64 expressed in terms of characteristic horizontal and vertical length scales H and L , respectively, and the
65 time scale T .

66 *2.1 Relatively thick mixed layers*

67 In temperate shelf seas, the surface and bottom mixed layers may occupy a considerable fraction of
68 the water depth. In summer, when stratification shows a maximum, they may still cover 60%-80% of the
69 water column, while in autumn and winter they may completely merge into a vertically homogeneous
70 water column (Bolding et al., 2002). In contrast to this, surface and bottom mixed layers in ocean basins,
71 which may have a comparable absolute thickness to shelf seas may cover only a small portion of the total
72 depth of several thousands of metres (Martin (1985)).

73 With H being the local time-averaged water depth, and D_s and D_b denoting surface and bottom mixed
74 layer thickness, respectively, this characteristics of coastal seas can be expressed as

$$75 \quad \frac{D_s + D_b}{H} = \mathcal{O}(1) \quad (2.1)$$

76 The major consequence of this is that turbulence closure models are needed which resolve the vertical
77 structure of the mixed layers including the interaction of vertical stratification and mixing (see Section
78 3.2.1). For the relatively thick bottom boundary layers, another implication is that the bed friction generates
79 relatively strong dissipation of kinetic energy in the water column. The latter may be enhanced in shallow
80 water, when the wave length of surface waves becomes comparable to the water depth, such that the orbital
81 wave motion adds to the bed stress. Due to the dynamic importance of the bottom boundary layer it is
82 required that it is vertically well-resolved everywhere. Considering the generally strongly variable bottom
83 bathymetry of the coastal ocean, this can be best achieved by *bottom-following vertical coordinates* (see
84 section 4.2).

85 2.2 Relatively high surface elevation amplitude

86 Coastal ocean models need to accurately predict the temporally and spatially varying free surface
87 elevation η . The sea surface elevation variability due to tides and storm surges is strongly enhanced in the
88 shallow coastal ocean, adding an important non-linearity to the dynamics, which cannot be neglected in the
89 model numerics. When denoting the standard deviation of the surface elevation as $\sigma(\eta)$, this characteristics
90 of the coastal ocean could be formulated as

$$91 \quad \frac{\sigma(\eta)}{H} = \mathcal{O}(1). \quad (2.2)$$

92 Furthermore, the relatively high surface elevation variation requires the use of *surface-following vertical*
93 *coordinates* to ensure sufficient vertical resolution of the near surface region.

94 An extreme case occurs when the surface elevation variability is larger than the mean water depth, such
95 that the sea bed is falling dry at times:

$$96 \quad \frac{\sigma(\eta)}{H} > 1. \quad (2.3)$$

97 In such cases, wetting and drying algorithms must be implemented to prevent unphysical negative water
98 depths (see Section 5.2).

99 2.3 Relatively strong horizontal and vertical gradients

100 In all eddy-resolving ocean models significant gradients due to detached eddies or upwelling can be
101 found. However, by definition, all global riverine input is discharged into coastal seas. Since the exchange
102 between the coasts and the interior of the adjacent shelf seas is limited, strong gradients build up in the
103 coastal ocean. Therefore, salinity in coastal ocean models may vary from river concentration (almost zero)
104 to ocean concentration within a few kilometres in the horizontal. It is this almost zero salinity that demands
105 not only for accurate, but also positive-definite numerical transport schemes. Strong stratification may be
106 generated in the vicinity of freshwater discharge such that also vertical gradients may be strong. In addition
107 to the salinity, also other tracers such a nutrients or suspended matter discharged by rivers may show strong
108 gradients. Let c be a relevant tracer (e.g., salinity), then the fact that horizontal or vertical gradients may
109 be relative strong in coastal seas can be expressed as

$$110 \quad \frac{\Delta c}{|\partial_{[x,y]}c|} \ll L, \quad \frac{\Delta c}{|\partial_z c|} \ll H, \quad (2.4)$$

111 with $\partial_{[x,y,z]}$ denoting horizontal and vertical derivatives.

112 2.4 Relatively short response time

113 Due to the shallow depth and the limited extension the coastal ocean typically reacts much stronger and
114 on much shorter time scales on external forcing than the global ocean. The key time scales in the coastal
115 ocean are tidal, inertial, diurnal or synoptic, i.e. $\mathcal{O}(1 \text{ day})$. One relevant time scale in the open ocean is
116 the life time of mesoscale eddies, i.e. order of week(s). Large scale ocean studies often concentrate on
117 much longer time scales by parameterising effects of tides, inertial oscillations or storms (see, e.g., Eden
118 et al. (2014)). In estuaries and coastal regions, complex dynamical changes will occur during a tidal cycle

119 with strong tidal asymmetries in mixing and secondary circulation, and substantial impact on transport
120 e.g. of salt and suspended matter (see, MacCready and Geyer (2010)). One example for this is the strain-
121 induced periodic stratification (SIPS, see Simpson et al. (1990)) due to horizontal density gradients as
122 often observed in regions of freshwater influence (see, e.g., Rippeth et al., 2001). Interior mixing in shelf
123 seas is often caused by inertial shear caused by episodic storm events combined with coastal coupling
124 (Craig (1989); van Haren et al. (1999); Knight et al. (2002)), a process which cannot be parameterised
125 in the coastal ocean due to its complex bathymetry and coastline. Therefore, different model physics e.g.
126 in terms of turbulence closure models (see the discussion at the end of section 3.2.1) requiring different
127 numerical schemes are needed for coastal ocean models.

128 2.5 *Relatively small spatial scales*

129 Probably the most obvious characteristics of the coastal ocean is its limited spatial extent:

$$130 \quad L \ll r_{Earth}, \quad (2.5)$$

131 with the Earth's radius r_{Earth} . Even if the entire coastal ocean is considered as one single global object (see
132 concepts by Holt et al. (2009)), large scale global or regional drivers need to be transferred to the coastal
133 ocean. For the remote meteorological forcing (weather systems) this is typically done by one-way or two-
134 way nesting to a regional atmospheric model which itself is coupled to a global model. For the remote
135 oceanic impact (tides, surges, planetary waves, etc.) this has to be done via lateral boundary conditions
136 coming from external models. Therefore, the problem of *open boundary conditions (OBCs) and model*
137 *nesting* is characteristic for coastal ocean models (as well as for the basin-scale ocean models), see the
138 discussions in Section 6. As for horizontal scales, also vertical scales are often smaller in the coastal ocean
139 than in the global ocean. Typically, the aspect ratio (depth to width ratio) is also sufficiently small in the
140 coastal ocean to justify application of the hydrostatic approximation. Since the Rossby radii in the coastal
141 ocean are often smaller than in the global ocean (see, e.g., Fennel et al. (1991)), only higher horizontal
142 resolution allows for eddy resolving simulations.

143 3 Basic equations

144 3.1 *Momentum and tracer equations*

145 Coastal and large scale ocean models typically use a common set of dynamic equations, which is based
146 on the Reynolds-averaged primitive equations including hydrostatic and Boussinesq approximations. De-
147 tailed derivations of these equations are e.g. found in Griffies and Adcroft (2008).

148 These equations are derived from the Navier-Stokes equations on the rotating Earth by first adopting
149 the Boussinesq approximation which includes the use of a constant reference density ρ_0 (instead of the
150 density ρ) in all terms except in the gravity term. This has the consequence that mass conservation is re-
151 placed by volume conservation. In a next step, the effects of small-scale turbulent fluctuations on the larger
152 scales are considered in a parameterised way without the necessity to numerically resolve them. This pro-
153 cedure assumes an ensemble averaging of the Navier-Stokes equations resulting in the Reynolds-averaged
154 Navier-Stokes equations which now include unknown turbulent stresses which need to be parameterised
155 (see section 3.2). Finally, a scaling analysis assuming a small aspect ratio (vertical scales are much smaller

156 than horizontal scales) motivates the degeneration of the vertical component of the momentum equation to
 157 the hydrostatic balance, neglecting vertical acceleration, the non-linear and the stress divergence terms and
 158 the effects of Earth rotation (see the discussion in Kanarska et al., 2007; Klingbeil and Burchard, 2013).
 159 The hydrostatic approximation enforces the traditional approximation for the Coriolis terms, neglecting the
 160 horizontal contributions of Earth rotation in the horizontal momentum equations. The dynamic equations
 161 are here for simplicity expressed in local Cartesian coordinates (see section 4 for spherical and curvilinear
 162 coordinates). After inserting the Boussinesq approximation into the mass conservation equation, the
 163 incompressibility condition remains:

$$164 \quad \partial_x u + \partial_y v + \partial_z w = 0, \quad (3.1)$$

165 with the Cartesian coordinates (x, y, z) (eastwards, northwards, upwards), and (u, v, w) being the Carte-
 166 sian components of the three-dimensional velocity vector \mathbf{u} .

167 Applying the incompressibility condition (3.1) and the hydrostatic condition (with pressure p and grav-
 168 itational acceleration $g = 9.81 \text{ m s}^{-2}$),

$$169 \quad \partial_z p = -g\rho, \quad (3.2)$$

170 (remainder of the vertical component of the Navier-Stokes equations) into the horizontal momentum equa-
 171 tions, the resulting dynamic equations are of the following form:

$$172 \quad \begin{aligned} & \partial_t u + \partial_x (u^2) + \partial_y (uv) + \partial_z (uw) \\ & = \partial_x T_{xx} + \partial_y T_{yx} + \partial_z T_{zx} + fv - \frac{1}{\rho_0} \partial_x p_a - g \partial_x \eta + \partial_x \int_z^\eta b \, dz' \end{aligned} \quad (3.3)$$

173 and

$$174 \quad \begin{aligned} & \partial_t v + \partial_x (vu) + \partial_y (v^2) + \partial_z (vw) \\ & = \partial_x T_{xy} + \partial_y T_{yy} + \partial_z T_{zy} - fu - \frac{1}{\rho_0} \partial_y p_a - g \partial_y \eta + \partial_y \int_z^\eta b \, dz', \end{aligned} \quad (3.4)$$

175 with time t , the local Coriolis frequency $f = 2\Omega \sin(\phi)$ (with the angular speed of Earth rotation $\Omega =$
 176 $7.29 \cdot 10^{-5} \text{ s}^{-1}$ and the latitude ϕ), the surface elevation η , and the surface pressure p_a . $T_{??}$ are the Cartesian
 177 components of the viscous stress tensor \mathbf{T} . The terms on the left hand sides of (3.3) and (3.4) are the
 178 tendency term, the three components of the advection terms (written in so-called integral form), the stress
 179 divergence terms, and the Coriolis term. The terms on the right hand side form the horizontal pressure
 180 gradient components $\partial_x p / \rho_0$ and $\partial_y p / \rho_0$. The formulation in the last line splits the pressure gradient into
 181 the external pressure gradient (composed of the atmospheric pressure gradient and the surface slope) and
 182 the internal pressure gradient, where $b = -(g/\rho_0)(\rho - \rho_0)$ is the buoyancy. In (3.3) and (3.4), the flux
 183 form for the advective terms is used, which results for any quantity q from the incompressibility condition

184 (3.1):

$$185 \quad u\partial_x q + v\partial_y q + w\partial_z q = \partial_x(uq) + \partial_y(vq) + \partial_z(wq), \quad (3.5)$$

186 which is the preferred form for coastal models in contrast to large-scale models sometimes based on the
 187 vector-invariant form for nonlinear terms, which facilitates the conservation of quantities like potential
 188 vorticity, enstrophy and/or kinetic energy (e.g. Arakawa and Lamb, 1977) (see section 7.1).

189 Equations (3.3) and (3.4) are valid for $-H(x, y) \leq z \leq \eta(x, y, t)$ (with the bottom coordinate $z =$
 190 $-H$). Dynamic boundary conditions at the free surface are

$$191 \quad \nabla(z - \eta) \cdot \mathbf{T} \Big|_{z=\eta} = \boldsymbol{\tau}^s, \quad (3.6)$$

192 with the horizontal Cartesian components of the surface stress vector (τ_x^s, τ_y^s) , calculated from meteorological
 193 data using bulk formulae (e.g., Kondo (1975); Fairall et al. (1996))¹. At the bottom, the dynamic
 194 boundary conditions are the no-slip conditions

$$195 \quad \nabla(z + H) \cdot \mathbf{u} \Big|_{z=-H} = 0. \quad (3.7)$$

196 For numerical reasons, however, generally an equivalent flux boundary condition is applied,

$$197 \quad \nabla(z + H) \cdot \mathbf{T} \Big|_{z=-H} = \boldsymbol{\tau}^b, \quad (3.8)$$

198 with the horizontal Cartesian components of the bed stress vector (τ_x^b, τ_y^b) reconstructed from a logarithmic
 199 velocity profile (see Section 7.6)².

200 Kinematic surface and bottom boundary conditions are:

$$201 \quad w \Big|_{z=\eta} = \partial_t \eta + u \Big|_{z=\eta} \partial_x \eta + v \Big|_{z=\eta} \partial_y \eta + (E - P), \quad (3.9a)$$

$$202 \quad w \Big|_{z=-H} = -u \Big|_{z=-H} \partial_x H - v \Big|_{z=-H} \partial_y H, \quad (3.9b)$$

204 with the evaporation rate E and the precipitation rate P . River run-off can be treated in various ways, e.g.
 205 as lateral boundary condition.

206 There is a large variety of lateral boundary conditions, which will be further discussed in section 6.

207 Within the Boussinesq approximation, the budget equation for internal energy reduces to a conservation
 208 equation for conservative temperature Θ :

$$209 \quad \partial_t \Theta + \partial_x(u\Theta) + \partial_y(v\Theta) + \partial_z(w\Theta) = -\partial_x J_x^\Theta - \partial_y J_y^\Theta - \partial_z J_z^\Theta + \frac{1}{C_p \rho_0} \partial_z I, \quad (3.10)$$

210 with the horizontal and vertical turbulent fluxes of Θ given by $J_{[x,y,z]}^\Theta$, the specific heat capacity of water
 211 at constant pressure, C_p , and irradiance in water, I . The positive vertical gradient of irradiance depends on
 212 the light absorption model applied. A classical model would be the model by Paulson and Simpson (1977),
 213 but often more complex models taking into account water colour, suspended matter and biogeochemical
 214 components are used. In (3.10), the heating due to viscous dissipation of turbulent kinetic energy is ne-
 215 glected, since in comparison to other terms in the local heat budget of the ocean this is a very small term

¹ Note that the physical stress in units of Pa is obtained as $\rho_0 \boldsymbol{\tau}^s$. The vertical component can be absorbed into the surface pressure.

² The vertical component is not needed in hydrostatic models.

216 (in contrast to conditions in the higher atmosphere). The surface boundary condition for the turbulent flux
 217 of temperature is formulated as

$$218 \quad \nabla(z - \eta) \cdot \mathbf{J}^\Theta \Big|_{z=\eta} = \frac{Q_s + Q_l + Q_b}{C_p \rho_0}, \quad (3.11)$$

219 with the sensible heat flux Q_s (due to the air-sea temperature difference), the latent heat flux Q_l (due to
 220 evaporation), and the long-wave back radiation Q_b . Note that upward (positive) fluxes of temperature
 221 lead to cooling at the surface. For the parameterisation of these heat fluxes various models are available,
 222 with the bulk formulae by Kondo (1975) and Fairall et al. (1996) being the most common ones for coastal
 223 applications.

224 The conservation equation for the absolute salinity S is of similar form as the temperature conservation
 225 equation, but without source term:

$$226 \quad \partial_t S + \partial_x (uS) + \partial_y (vS) + \partial_z (wS) = -\partial_x J_x^S - \partial_y J_y^S - \partial_z J_z^S. \quad (3.12)$$

227 In order to guarantee that no salt crosses the free surface, the diffusive salinity flux at the surface must
 228 compensate the advective salinity flux associated with (3.9a),

$$229 \quad \nabla(z - \eta) \cdot \mathbf{J}^S \Big|_{z=\eta} = -(E - P)S, \quad (3.13)$$

230 see Beron-Vera et al. (1999) for details. In contrast to this analytical formulation, in the discrete model
 231 equations the salinity of the surface freshwater flux simply can be set to zero and no compensating diffusive
 232 salinity flux is necessary, see discussion after (4.2). The density is calculated by means of an empirical
 233 equation of state as function of temperature Θ , salinity S and pressure p :

$$234 \quad \rho = \rho(\Theta, S, p). \quad (3.14)$$

235 A recent and accurate formulation for Boussinesq models has been provided by Roquet et al. (2015).

236 3.2 Turbulence closure

237 Turbulence closure modelling involves complex theories. For an overview, the reader is referred to
 238 text books (Kantha and Clayson, 2000b; Griffies, 2004; Cushman-Roisin and Beckers, 2011; Olbers et al.,
 239 2012). In most ocean models, vertical and horizontal turbulent fluxes of scalars are parameterised by a
 240 down-gradient approximation of the form

$$241 \quad \mathbf{J}^c = -(A_c \mathbf{R} + K_c \hat{\mathbf{z}} \hat{\mathbf{z}}) \cdot \nabla c, \quad (3.15)$$

242
 243
 244 using lateral and vertical eddy diffusivities A_c and K_c for any scalar c . Whereas the vertical diffusivity is
 245 defined in the direction of the vertical unit vector $\hat{\mathbf{z}}$, the lateral diffusivity acts in a direction depending on
 246 the rotation tensor \mathbf{R} (see Section 7.5.1). In the simplest case, the turbulent tracer fluxes are given by
 247 $J_{[x,y]}^c = -A_c \partial_{[x,y]} c$ and $J_z^c = -K_c \partial_z c$.

248 For the vertical turbulent momentum fluxes, an equivalent formulation is generally used:

$$249 \quad T_{z[x,y]} = K_M \partial_z [u, v], \quad (3.16)$$

250 with the vertical eddy viscosity K_M . The parameterisation of the horizontal turbulent momentum fluxes is
 251 usually based on transverse isotropy, yielding:

252

$$253 \quad \begin{bmatrix} T_{xx} & T_{yx} \\ T_{xy} & T_{yy} \end{bmatrix} (u, v) = A_M \begin{bmatrix} 2\partial_x u & \partial_y u + \partial_x v \\ \partial_y u + \partial_x v & 2\partial_y v \end{bmatrix}, \quad (3.17)$$

254

255 or

$$256 \quad \begin{bmatrix} T_{xx} & T_{yx} \\ T_{xy} & T_{yy} \end{bmatrix} (u, v) = A_M \begin{bmatrix} \partial_x u - \partial_y v & \partial_y u + \partial_x v \\ \partial_y u + \partial_x v & -(\partial_x u - \partial_y v) \end{bmatrix}, \quad (3.18)$$

257

258 with the horizontal eddy viscosity A_M and (3.18) being also valid for compressible fluids. An alterna-
 259 tive to the resulting Laplacian friction operators is biharmonic friction, which more selectively acts on the
 260 smaller scales.

261 In (3.17) and (3.18) the turbulent fluxes are oriented in the horizontal direction. Since the transforma-
 262 tion of the stress divergence to general vertical coordinates is cumbersome, the momentum diffusion is
 263 usually simply carried out along coordinate surfaces. Whereas this treatment is justified for the anyhow
 264 highly empirical momentum fluxes, more care is necessary for tracer fluxes (see Section 7.5.1).

265 3.2.1 Vertical turbulence modelling

266 Due to the dominance of surface and bottom mixed layers in coastal ocean dynamics (see section 2.1),
 267 vertical eddy viscosity and diffusivity must be carefully parameterised. For this, two basic approaches are
 268 commonly used in ocean models.

269 One of them is based on direct algebraic computation of the eddy parameters from bulk properties
 270 (boundary fluxes, mixed layer depth, bulk Richardson number) of the surface and bottom mixed layers,
 271 the so-called K-profile parameterisation (KPP) which has been originally proposed for large-scale ocean
 272 models by Large et al. (1994). In addition to the down-gradient fluxes, also counter-gradient flux compo-
 273 nents (for example for convectively unstable boundary layers) are included in the KPP model. Many mod-
 274 ifications of the original KPP model have been proposed (see, e.g., Smyth et al., 2002; Durski et al., 2004;
 275 Uchiyama et al., 2010) to extend its applicability also to coastal ocean applications (see, e.g., Blaas et al.,

276 2007). The KPP model assumes that the boundary layer turbulence is in equilibrium with the surface or
 277 bottom fluxes, respectively. For large scale ocean models, this might often be an adequate approximation.
 278 In many coastal model applications however, the deviation from this equilibrium is a first-order process
 279 which cannot be neglected.

280 The other closure approach, which in contrast to the KPP model considers high temporal and spatial
 281 variability in boundary layers, is based on a dynamic equation for the turbulent kinetic energy (TKE), k ,
 282 which can be derived from the Navier-Stokes equations by means of Reynolds-averaging (Wilcox, 1998;
 283 Burchard, 2002a):

$$284 \quad \partial_t k + \partial_x (uk) + \partial_y (vk) + \partial_z (wk) - \partial_z \left(\frac{K_M}{S_{C_k}} \frac{\partial k}{\partial z} \right) = P + B - \varepsilon, \quad (3.19)$$

285 with the shear production, $P = K_M M^2$ including the vertical shear squared, M^2 , and the buoyancy
 286 production, $B = -K_c N^2$, with the buoyancy frequency (or Brunt-Väisälä frequency) squared, N^2 , and
 287 the dissipation rate, ε . The shear production P transfers kinetic energy lost from the mean flow due to
 288 vertical stress divergence to the turbulent kinetic energy, whereas the buoyancy production B exchanges
 289 energy between the mean potential energy to the turbulent kinetic energy. Note, that in (3.19) the down-
 290 gradient approximation has been adopted with the turbulent Schmidt number S_{C_k} , which is of order unity.
 291 Horizontal turbulent fluxes are generally neglected for the TKE budget (Delhez et al., 1999). This may also
 292 be the case for the advective terms, but in tidally energetic regimes, such a neglect might lead to significant
 293 errors or instabilities. In addition to the TKE, also the length scale of the energy containing eddies, l , needs
 294 to be approximated to obtain an estimate for the vertical eddy viscosity and eddy diffusivity. Once k and l
 295 are known, the vertical eddy coefficients can be calculated as

$$296 \quad K_M = S_M k^{1/2} l, \quad K_c = S_c k^{1/2} l, \quad (3.20)$$

297 with the non-dimensional stability functions S_M and S_c . The dissipation rate ε can be calculated from l via
 298 the cascading relation, derived from integration of the kinetic energy spectrum over the inertial subrange,

$$299 \quad \varepsilon = c_\varepsilon \frac{k^{3/2}}{l} \quad (3.21)$$

300 with the empirical constant c_ε .

301 Surface and bottom boundary conditions are typically derived from the law of the wall, resulting in k
 302 being proportional to the surface or bed stress, respectively, and the length scale to be proportional to the
 303 respective roughness length. Equivalent flux conditions, which proved to be numerically more stable have
 304 been proposed (Burchard and Petersen, 1999). To parameterise effects of breaking surface waves, injection
 305 of TKE at the surface is applied (Burchard, 2001). Effects of Langmuir Circulation on the dynamics of the
 306 surface mixed layer may be parameterised as well (see, e.g., Harcourt, 2014). Additional frictional effects
 307 of surface waves on wave drag in shallow water can also be considered in the bottom boundary condition
 308 (Mellor, 2002).

309 Various methods are used in ocean modelling to calculate the length scale l . In one-equation turbulence
 310 closure models (the one equation is for the computation of the TKE), l is calculated from combinations
 311 of geometric length scales (such as the distance from the surface or the bottom) or from hydrodynamic
 312 length scales (such as the Ozmidov scale), see e.g., Mellor and Yamada (1982); Gaspar et al. (1990).
 313 More common in coastal ocean models are however two-equation turbulence closure models which in
 314 addition to the TKE equation calculate a budget equation for an independent length-scale related quantity.

315 Most commonly, a budget equation for the dissipation rate ε (k - ε models, see Rodi, 1987; Burchard
316 and Baumert, 1995) is constructed and closed by the assumption that the source and sink terms can be
317 modelled as a linear combination of P , B and ε . Instead of ε , also other length-scale-related properties
318 could be budgeted (Mellor and Yamada, 1982; Wilcox, 1998; Umlauf and Burchard, 2003). However,
319 when properly calibrated, all these two-equation models which differ only in the turbulent transport term
320 perform similarly (Burchard et al., 1998; Umlauf and Burchard, 2003; Warner et al., 2005).

321 Two-equation turbulence closure models including algebraic second-moment closures as outlined here
322 (see also the review by Umlauf and Burchard, 2005) have proven in many applications as a good com-
323 promise between computational efficiency and realistic representation of relevant processes in the coastal
324 ocean.

325 There is a number of reasons, why such second-moment turbulence closure models are an important
326 feature of coastal ocean models. First of all, as discussed in section 2.1, a large portion of water columns
327 in the coastal ocean (if not the entire water column) are covered by surface or bottom boundary layers.
328 These boundary layers have a vertical structure which locally influences the mixing coefficients. One
329 example is tidal straining in coastal regions of freshwater influence, where flood shear destabilises and
330 ebb shear stabilises the water water column, leading to asymmetric eddy coefficients and residual currents
331 (Jay and Musiak, 1994; Rippeth et al., 2001). Therefore, boundary layer models reacting on local forcing
332 instead of surface or bottom fluxes only are required. Secondly, relevant times scale in the coastal ocean
333 are much shorter than in the global ocean (see section 2.4). Therefore, the turbulence closure models need
334 to react on correct time scales to rapid time changes in surface or bottom stress instead of instantaneously
335 adjusting the eddy coefficients in the entire mixed layers such as in the KPP model. Such requirements are
336 only fulfilled by carefully calibrated second-moment turbulence closure models. Nonetheless, successful
337 implementations of extended KPP models to coastal ocean scenarios on shelf sea scale have been reported
338 (Durski et al., 2004; Wilkin et al., 2005).

339 There are a few global ocean models using low-level second-moment closures (see, e.g., Oschlies
340 (2002); Danabasoglu et al. (2014)), which typically are based on the Gaspar et al. (1990) one-equation
341 model, where the turbulent length scale l is algebraically computed. Two-equation turbulence closure
342 models are typically not used in global ocean models. For climate models, this is mainly due to the
343 large baroclinic time steps (about 1 hour) and the coarse resolution in boundary layers. In high-resolution
344 global models, temporal and spatial resolution of boundary layers may be sufficiently high for applying
345 two-equation turbulence closure models, but there, the focus is still more on bulk effects of the boundary
346 layers on transmitting fluxes between ocean and atmosphere or ocean and sea floor, rather than resolving
347 their dynamics. Therefore, in large-scale ocean models, the KPP model (see above) or other models with
348 reduced dynamics (see, e.g., Jackson et al. (2008)) are used.

349 3.2.2 *Horizontal subgrid-scale closure*

350 Whereas in ocean models a consistent theoretical framework for the vertical turbulent fluxes exists,
351 such a rigorous closure for the horizontal turbulent fluxes due to meso-scale and submeso-scale eddies
352 is still missing. For large scale ocean models which do not resolve meso-scale eddies, closures have
353 been proposed, such as the Gent and McWilliams (1990) closure for isopycnal mixing or the dynamic
354 meso-scale eddy closure by Eden and Greatbatch (2008). In addition, for high-resolution global models
355 submeso-scale eddy closures (Fox-Kemper et al., 2011) and flow-dependent subgrid-scale closures (Pear-
356 son et al., 2017) have been investigated. Coastal ocean models usually do not deal with sophisticated eddy
357 parameterisations. This practice is motivated by the high horizontal resolution, and the difficult treatment

358 of isopycnal eddy-induced fluxes in well-mixed coastal areas and their rotation in vertically boundary-
 359 following coordinates.

360 Two simplistic common approaches used in the coastal ocean modelling community are to either ne-
 361 glect horizontal turbulent fluxes (and then rely on the diffusive fluxes associated with monotone, upstream-
 362 biased advection schemes, see section 7) or to set A_M and A_c to constant values. In the latter case, the
 363 proper choice of the horizontal exchange coefficients is then determined by sensitivity studies. A phys-
 364 ically more sound, resolution-dependent parameterisation of horizontal momentum fluxes has been pro-
 365 posed by Smagorinsky (1963). Consistent with (3.17) or (3.18) the horizontal eddy viscosity can be derived
 366 as

$$367 \quad A_M = C_M(\Delta x \Delta y) \sqrt{(\partial_x u)^2 + \frac{1}{2}(\partial_y u + \partial_x v)^2 + (\partial_y v)^2}, \quad (3.22)$$

368 or

$$369 \quad A_M = C_M(\Delta x \Delta y) \sqrt{\frac{1}{2}(\partial_x u - \partial_y v)^2 + \frac{1}{2}(\partial_y u + \partial_x v)^2}, \quad (3.23)$$

370 with the horizontal grid sizes Δx and Δy , and with the empirical parameter C_M . The latter has been
 371 estimated for (3.22) by Holt and James (2006) in a shelf sea application as $C_M \approx 0.2$. The same approach
 372 as (3.22) can also be applied for horizontal tracer diffusivities (see, e.g., Gräwe et al., 2015), using a
 373 different value for the empirical parameter.

374 **4 Coordinate transformations and spatial discretisation**

375 The set of governing equations, consisting of the continuity equation (3.1), the hydrostatic momentum
 376 equations (3.3) and (3.4), and the prognostic equations for temperature (3.10) and salinity (3.12), so far
 377 has been formulated in a local Cartesian reference frame at the Earth surface for simplicity. However, the
 378 transformation to coordinate systems that align with the geometry of the domain is often advantageous.

379 Most coastal ocean models support orthogonal curvilinear coordinates in the horizontal to offer the
 380 formulation in spherical coordinates and to some extent the alignment with coastlines. Orthogonal curvi-
 381 linear coordinates also provide some flexibility to increase the horizontal resolution in certain parts of the
 382 domain such as estuaries or towards the coast as required to resolve the typically strong near-coastal hori-
 383 zontal gradients, see (2.4). In this way also structured-grid models can be used for multi-scale applications.
 384 The corresponding basis transformation to orthogonal curvilinear coordinates introduces additional metric
 385 coefficients (see, e.g. Kantha and Clayson (2000a)). For clarity, the governing equations in the remainder
 386 of this review will be kept in horizontal Cartesian coordinates.

387 In the vertical the alignment with the boundaries (free surface and bottom topography) and proper res-
 388 olution (of e.g. the boundary layers and pycnoclines) is even more critical than in the horizontal. A general
 389 description that supports various types of vertical coordinates is given by the s -coordinates of Kasahara
 390 (1974). The general vertical coordinate $s(x, y, z, t)$ must be strictly monotone in z in order to guarantee
 391 a unique inverse transformation $z(x, y, s, t)$ and a well-defined Jacobian $\partial_s z = (\partial_z s)^{-1}$ for the transfor-
 392 mation of the governing equations. For isopycnal coordinates $s = \rho$ this precludes the representation of
 393 unstable stratification. The horizontal coordinates and time do not change under the transformation and, if
 394 necessary for the purpose of clarity, derivatives with respect to constant s and z will be distinguished by
 395 $(\cdot)_s$ and $(\cdot)_z$, respectively. With the Lagrangian derivative D/Dt the dia-surface velocity component (see,

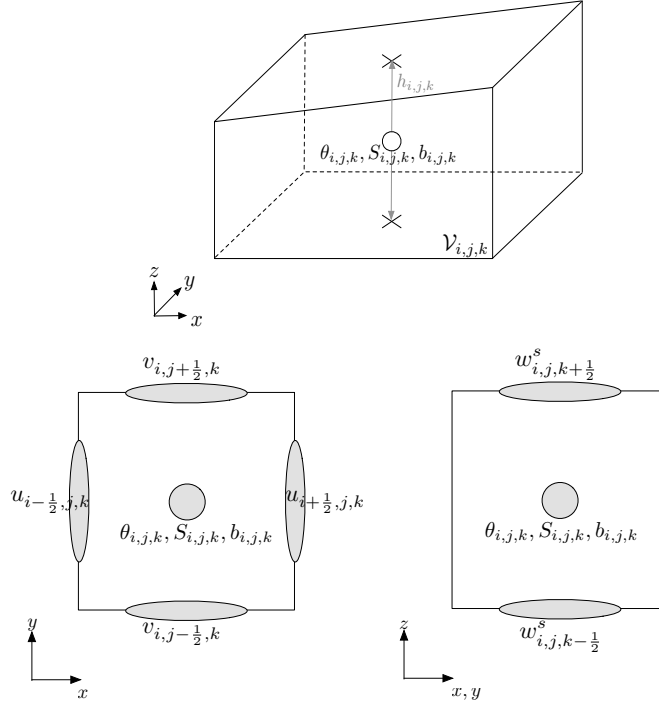


Fig. 1. Control volume for cell-centered tracer variables (top), staggering showing the location of the dependent variables in the horizontal (bottom, left) and in the vertical (bottom, right).

e.g., Griffies (2004)) is given by

$$w^s = \partial_s z \frac{Ds}{Dt} = w - (\partial_t z)_s - u (\partial_x z)_s - v (\partial_y z)_s. \quad (4.1)$$

Coastal ocean models traditionally discretise the governing equations on an Arakawa C-grid (Arakawa and Lamb, 1977), as the Rossby radius of deformation is usually properly resolved and the C-grid arrangement offers a better representation of small coastal inlets. In the vertical the corresponding variable arrangement is known as Lorenz grid (Lorenz, 1960). This fully staggered arrangement of velocities between tracer points also naturally fits to a conservative Finite-Volume discretisation around tracer cells (see Fig. 1). The corresponding discrete equations can be derived from the continuous ones by integration over a discrete control volume cell. Thereby divergence terms are cast into differences of fluxes through opposite cell interfaces. In order to demonstrate the procedure, in the following only the integration along the vertical dimension is carried out.

4.1 Layer-integrated equations

The vertical discretisation of the transformed space into k_{\max} layers with interfaces at fixed levels $s_{k+1/2}$ (independent of x , y , t and with $k \in [0, k_{\max}]$) is equivalent to a discretisation of the physical space into k_{\max} layers with interfaces at variable levels $z_{k+1/2}(x, y, t) = z(x, y, s_{k+1/2}, t)$ and $z_{k+1/2} > z_{k-1/2}$, see Burchard and Petersen (1997).

With layer heights $h_k(x, y, t) = \int_{s_{k-1/2}}^{s_{k+1/2}} \partial_s z ds = z_{k+1/2} - z_{k-1/2}$, layer-averaged prognostic quantities $q_k(x, y, t) = h_k^{-1} \int_{z_{k-1/2}}^{z_{k+1/2}} q dz$, for $k \in [1, k_{\max}]$ and $q \in \{1, u, v, \Theta, S\}$, and $w_{k+1/2}^s(x, y, t) =$

416 $w^s(x, y, z_{k+1/2}, t)$, the layer-integration of (3.1), (3.3), (3.4), (3.10) and (3.12) yields the prototype equa-
 417 tion:

418
 419
$$\partial_t (h_k q_k) + \partial_x (h_k u_k q_k) + \partial_y (h_k v_k q_k) + \left(w_{k+1/2}^s \tilde{q}_{k+1/2} - w_{k-1/2}^s \tilde{q}_{k-1/2} \right)$$

 420
$$= -\partial_x (h_k J_{x,k}^q) - \partial_y (h_k J_{y,k}^q) - \left(J_{z,k+1/2}^q - J_{z,k-1/2}^q \right) + h_k F_k^q. \quad (4.2)$$

 421

422 In (4.2) the interfacial values $\tilde{q}_{k+1/2}$ with $q \in \{u, v, \Theta, S\}$ are approximated by the vertical advection
 423 scheme, see Sec. 7.1. According to (4.1) the kinematic boundary conditions (3.9a) and (3.9b) transform
 424 to $w_{k_{\max}+1/2}^s = E - P$ and $w_{1/2}^s = 0$.

425 The full set of layer-integrated equations can be found in A. The layer-integrated continuity equation
 426 (A.1) can be obtained from (4.2) with $q = 1$ and $\mathbf{J}_k^1 = F_k^1 = 0$.

428 Within the layer-integrated momentum equations (A.2) and (A.3) the momentum fluxes through the
429 interfaces, i.e. the vertical shear stresses, are defined as

$$430 \quad -J_{z,k+1/2}^{[u,v]} = \tau_{[x,y],k+1/2} = \begin{cases} \tau_{[x,y]}^s(u_{k_{\max}}, v_{k_{\max}}), & k = k_{\max} \\ K_{M,k+1/2} \frac{[u,v]_{k+1} - [u,v]_k}{z_{k+1} - z_k}, & k \in [1, k_{\max} - 1], \\ \tau_{[x,y]}^b(h_1, u_1, v_1), & k = 0 \end{cases} \quad (4.3)$$

432 based on (3.16) with the dynamic boundary conditions (3.6) and (3.8), and with centre positions $z_k =$
433 $\frac{1}{2}(z_{k-1/2} + z_{k+1/2})$. Following the discussion at the end of Section 3.2, the lateral contributions of the
434 stress tensor are often approximated according to Mellor and Blumberg (1985) and Kantha and Clayson
435 (2000a):

$$436 \quad \tilde{F}_{[x,y]}^h(h, u, v) = \frac{1}{h} \left(\partial_x \left(h T_{x[x,y]}(u, v) \right) + \partial_y \left(h T_{y[x,y]}(u, v) \right) \right), \quad (4.4)$$

438 i.e. $J_{[x,y]}^u = -T_{[x,y]x}$ and $J_{[x,y]}^v = -T_{[x,y]y}$, with $T_{??}$ given by (3.17) or (3.18) and all gradients calculated
439 along layer k . In case of diffusion along directions not aligned with constant s , additional terms due to
440 non-diagonal elements of the diffusion tensor would occur (Griffies (2004)). One numerically demanding
441 contribution to $F_k^{[u,v]}$ is the internal pressure gradient force given by

$$442 \quad F_{[x,y],k}^{\text{IPG}} = \frac{1}{h_k} \int_{z_{k-1/2}}^{z_{k+1/2}} \left(\partial_{[x,y]} \right)_z \int_z^\eta b(x, y, z') dz' dz, \quad (4.5)$$

444 and approximated in terms of the layer-averaged buoyancies b_k (see Section 7.2).

445 Within the layer-integrated temperature and salinity equations (A.4) and (A.5) the turbulent fluxes
446 $J_{[x,y,z]}^{[\Theta,S]}$ are based on (3.15). The surface temperature flux is given according to (3.11) by $J_{z,k_{\max}+1/2}^\Theta =$
447 $\frac{Q_s + Q_l + Q_b}{C_p \rho_0}$ and the source term by the divergence of the interfacial irradiance $F_k^\Theta = \frac{1}{C_p \rho_0} \frac{I_{k+1/2} - I_{k-1/2}}{h_k}$.

448 As mentioned in the context of the boundary condition for salt fluxes (3.13), the surface salinity fluxes
449 are zero, i.e. $\tilde{S}_{k_{\max}+1/2} = 0$ and $J_{z,k_{\max}+1/2}^S = 0$.

450 4.2 Examples for vertical coordinates

451 The almost arbitrary choice of the transformation function $s = s(x, y, z, t)$ or equivalently of the
452 moving layer interfaces $z_{k+1/2}(x, y, t)$ allows for a high degree of freedom for the vertical layout which
453 can be exploited to improve the model performance.

454 4.2.1 Geopotential coordinates

455 Geopotential (or z -) coordinates (see Figure 2d) are based on globally defined z -levels $z_{k+1/2}$ which do
456 not depend on location or time, except for the uppermost coordinate level $z_{k_{\max}+1/2} = \eta$ which is identical
457 to the free surface. Vertical resolution is typically increased near the surface to properly reproduce the
458 dynamics of the surface mixed layer. Since for too fine near-surface vertical resolution the moving and
459 sloping free surface might intersect with one or more coordinate levels, the fixed geopotential coordinate
460 level $z_{k_{\max}-1/2}$ must be chosen such that it is below the minimum surface elevation. For models of shelf
461 seas with a large maximum tidal range (see Sec. 2.2) this would result in a large mean thickness of the

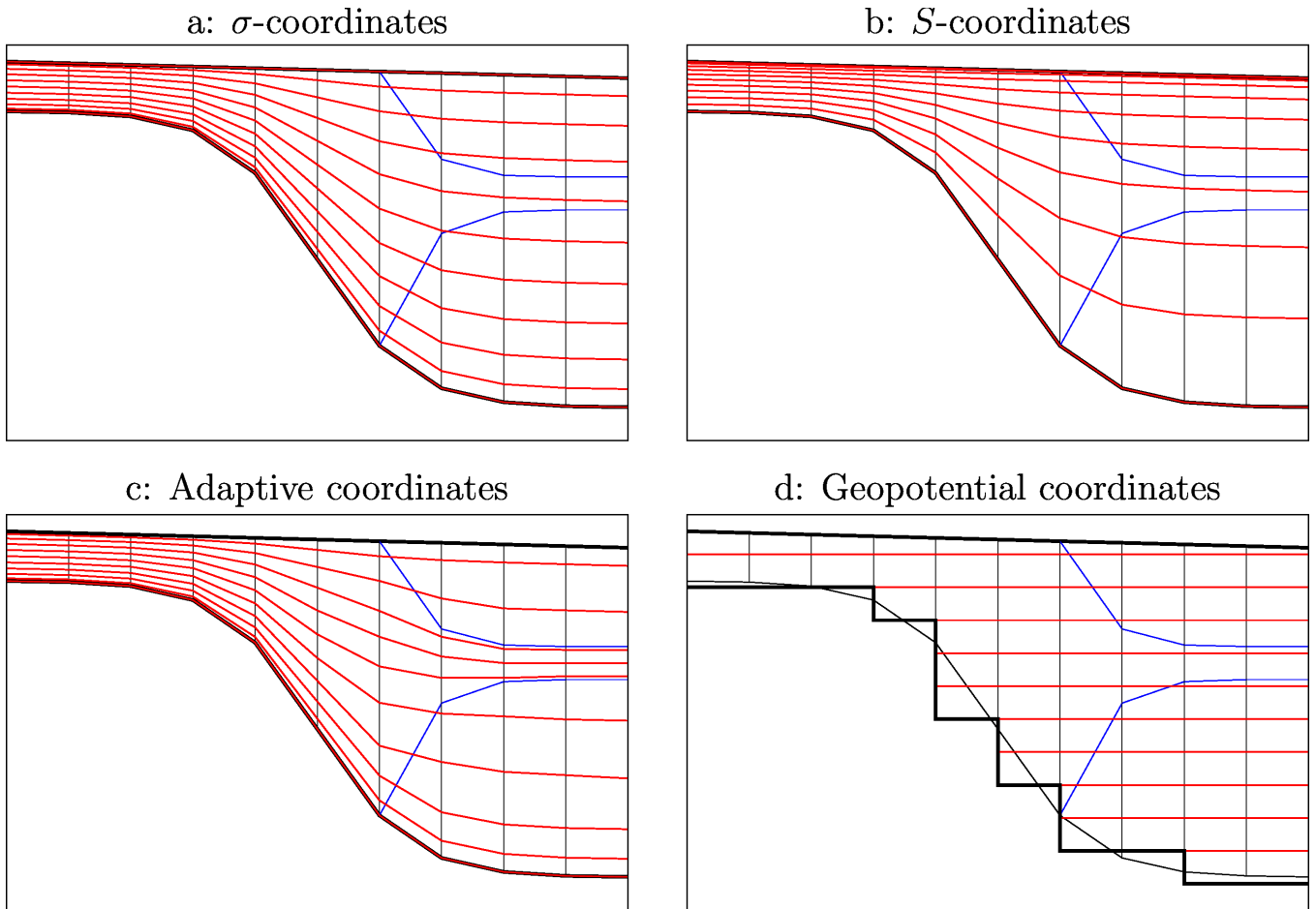


Fig. 2. Sketch showing a vertical transect through a coastal ocean model domain including four different vertical coordinates. The blue lines indicate two selected isopycnals representing a tidal front with a stratified shelf sea region to the right and a well-mixed coastal region to the left. The vertical lines indicate the horizontal discretisation, the red lines show the vertical coordinate surfaces and the bold black lines show the bottom and surface representation of the coordinates. a: σ -coordinates with zooming towards the surface and the bottom; b: S -coordinates with high near-surface resolution; c: Adaptive coordinates with increased resolution in the stratified region; d: Geopotential coordinates (note that shaved cells would remove the staircase representation of the bottom topography).

462 upper layer of $\mathcal{O}(10\text{m})$, such that near-surface processes are not well-resolved (see, e.g., Mathis et al.
 463 (2015)). For simulations of shallow coastal regions including drying and flooding this would mean that
 464 all areas with intertidal flats are not vertically resolved. One solution to this problem has been proposed
 465 by Casulli and Cheng (1992) and Burchard and Baumert (1998): Layers at the surface are locally added
 466 or removed when the surface layer becomes too thick or too thin, respectively. This problem can also be
 467 solved by applying so-called z^* -coordinates (Adcroft and Campin (2004)), where geopotential coordinates
 468 are obtained for $\eta = 0$ everywhere, and all layer thicknesses are then locally multiplied by $(\eta + H)/H$,
 469 such that the layers are squeezed or expanded with the changing water depth. Another advantage of these
 470 surface-following coordinates is a reduced vertical transport across the moving layer interfaces and thus
 471 significantly reduced numerical mixing caused by advection schemes (see Sections 4.2.3 and 7.5.2). In
 472 particular near the surface the tidal elevation triggers a large oscillating vertical velocity relative to the
 473 fixed z -coordinate levels which generates strong numerical mixing .

474 At the bottom geopotential layers will be intersecting with the sloping bottom. This leads to a stair-case
 475 type of discretisation of bottom slopes which leads to low accuracy in resolving bottom parallel currents

476 such as dense bottom currents (Ezer and Mellor, 2004). A partial solution to this problem has been pro-
 477 posed by Beckmann and Döscher (1997) by coupling an empirical terrain-following bottom boundary
 478 layer model to the geopotential model grid, allowing for bottom-parallel down-slope flow. Another ap-
 479 proach to improve representation of along-bottom flow has been proposed by Adcroft et al. (1997): to
 480 introduce *shaved cells* at the bottom to better fit the bottom topography. Geopotential coordinates over
 481 sloping topography have one other inherent problem: practically they do not allow a high vertical reso-
 482 lution near the bottom. A resolution of the bottom layer of 1 m would require equidistant geopotential
 483 coordinates over the entire water column, which is often computationally not affordable.

484 Given all these disadvantages of geopotential coordinates they can generally not be recommended for
 485 coastal ocean simulations. There is however one potential problem of vertical coordinates which is not
 486 relevant for geopotential coordinates: the internal pressure gradient problem, see Sec. 7.2. Furthermore,
 487 in strongly stratified systems isopycnal surfaces can align well with geopotential levels, and in this case
 488 diapycnal mixing is not artificially increased by any along-layer mixing. Therefore, models with geopo-
 489 tential coordinates are still applied for problems with strong stratification such as the Baltic Sea (Wang
 490 et al. (2015)).

491 The numerical treatment of geopotential coordinates fits into the concept of general vertical coordinates
 492 by formally allowing layers of zero thickness at the bottom and, in the case of removable surface layers,
 493 also at the surface.

494 4.2.2 Terrain-following coordinates

495 A transformation function of the form

$$496 \quad z(x, y, s, t) - \eta = S(x, y, s, t)D \quad (4.6)$$

498 with the local water depth $D = \eta + H$, the stretching function S being strictly monotone in s , $S(s_{1/2}) =$
 499 -1 and $S(s_{k_{\max}+1/2}) = 0$ generates terrain-following coordinates with $z_{1/2} = -H$ and $z_{k_{\max}+1/2} = \eta$.
 500 In addition to the free surface being a coordinate surface (as for the z^* -coordinates), also the bottom is
 501 a coordinate surface. Thus, in every watercolumn k_{\max} layers are active and masking of layers is not
 502 necessary. A classical option for coastal ocean model simulations are σ -coordinates defined by $S = s =$
 503 σ (Nihoul et al. (1986); Blumberg and Mellor (1987)), see Figure 2a. They result in layer thicknesses
 504 proportional only to the local water depth, which is a disadvantage especially in deeper waters (where
 505 layers may become too thick and thus resolution in critical parts of the water column too coarse) or
 506 above steep bottom slopes (where coordinate slopes are relatively steep throughout the water column, see
 507 Deleersnijder and Beckers (1992)). One other problem of terrain-following coordinates is the intersection
 508 of sloping coordinate surfaces with isopycnals. For the calculation of the internal pressure gradient, this
 509 results in a balance of two large terms which typically results in large truncation errors and thus artificial
 510 currents (see Sec. 7.2 for a detailed discussion).

511 Some of these problems can be reduced by using non-equidistant σ -levels $\sigma_{k+1/2}$ (equivalent to non-
 512 linear stretching functions $S(s)$) and modified stretching functions $S(x, y, s)$ that rescale the near-surface
 513 layer heights proportional to a fixed critical water depth instead of to the local water depth (Song and
 514 Haidvogel, 1994; Shchepetkin and McWilliams, 2009b), see Figure 2b.

515 An alternative transformation function that maintains high resolution at the surface or at the bottom
 516 independently of the local water depth has been developed by Burchard and Petersen (1997) and Burchard
 517 and Bolding (2002).

518 In order to obtain higher accuracy, hybridisations between s - and z -coordinates have been proposed,
 519 leading to less steep coordinate slopes than for s coordinates and smaller bottom steps than for z -coordinates,
 520 see Gerdes (1993), Burchard and Petersen (1997), Dukhovskoy et al. (2009) or O’Dea et al. (2012) for
 521 details.

522 4.2.3 Arbitrary Lagrangian-Eulerian (ALE) coordinates

523 For geopotential and terrain-following coordinates the transformation function $z(s)$ is explicitly pre-
 524 scribed. The temporal evolution of the corresponding interface positions $z_{k+1/2}(x, y, t)$ and layer heights
 525 $h_k(x, y, t)$ is fully determined by a prognostic equation for the sea surface elevation $\eta(x, y, t)$ (see Sec.
 526 5.1). In this case the continuity equation (A.1) does not serve as a prognostic equation for h_k , but as a
 527 diagnostic equation for the grid-related vertical velocity $w_{k+1/2}^s$. Following Adcroft and Hallberg (2006),
 528 this is the Eulerian treatment of the vertical direction (EVD).

529 In contrast, the Lagrangian treatment of the vertical direction (LVD) is based on a Lagrangian vertical
 530 coordinate, formally defined by $\frac{Ds}{Dt} = 0$ (Starr, 1945). In this case the grid-related vertical velocity vanishes
 531 $w^s = 0$, see (4.1), and the continuity equation (A.1) serves as a prognostic equation for the layer heights
 532 h_k . Numerical mixing (induced by truncation errors of discrete advective fluxes; see Section 7.5.2) is
 533 significantly reduced in Lagrangian vertical coordinates because of the missing advective transport through
 534 the coordinate surfaces. However, a pure Lagrangian movement of the layers is prone to grid distortion
 535 and possibly vanishing layers, which complicates the numerical treatment.

536 Therefore, a combination of LVD and EVD gains increasingly popularity. Originally Hirt et al. (1974)
 537 defined the Arbitrary Lagrangian-Eulerian (ALE) method by a Lagrangian mesh movement (LVD step)
 538 followed by an optional readjustment of the mesh associated with grid-related advective transports (EVD
 539 step). The advection during the EVD step can be replaced by instantaneous ”remapping” (monotone and
 540 conservative interpolation, see e.g. White and Adcroft, 2008) which relaxes the strict CFL constraint to a
 541 less severe Lipschitz type criteria of the form $\Delta t \max |\nabla \mathbf{u}| < 1$.

542 Another approach is to consider Lagrangian tendencies in the calculation of the layer heights used in
 543 EVD algorithms. As the treatment of the full motion in a Lagrangian way is prone to grid distortion,
 544 only particular contributions are considered. Separable terrain-following coordinates of the form $z -$
 545 $\eta = S(s)D(x, y, t)$ inherently imply a Lagrangian treatment of merely barotropic motions (Shchepetkin
 546 and McWilliams, 2009b). Non-separable terrain-following coordinates with time-independent stretching
 547 functions $S(x, y, s)$ do not exactly treat barotropic motions in a Lagrangian way, but also significantly
 548 reduce the corresponding grid-related vertical transports by scaling the layer heights according to $h_k =$
 549 $\frac{D}{H} h_k^{(\eta=0)}$. The same holds for the z^* -coordinates of Adcroft and Campin (2004), see Section 4.2.1. Recently,
 550 Leclair and Madec (2011) proposed to also treat fast oscillating baroclinic currents in a Lagrangian way
 551 by introducing the so-called \tilde{z} -coordinate.

552 4.2.4 Adaptive coordinates

553 In order to further optimise the vertical grid layout in 3D models, Hofmeister et al. (2010) presented
 554 adaptive coordinates, see Figure 2c. These do not only consider Lagrangian tendencies, but also a zoom-
 555 ing of layers towards boundaries, stratification and shear. This zooming is based on a vertical diffusion
 556 equation for the interface positions,

$$557 \quad \partial_t z_{k+1/2} - \left(D_{k+1}^{\text{grid}}(z_{k+3/2} - z_{k+1/2}) - D_k^{\text{grid}}(z_{k+1/2} - z_{k-1/2}) \right) = 0, \quad (4.7)$$

559 with boundary conditions $z_{1/2} = -H$ and $z_{k_{\max}+1/2} = \eta$ (Burchard and Beckers, 2004). A vertically
560 constant layer "diffusion" coefficient D^{grid} (unit s^{-1}) tends to generate equidistant layers, whereas locally
561 increased coefficients (e.g. proportional to stratification and shear) increase the local concentration of layer
562 interfaces and thus the vertical resolution. Improved vertical resolution decreases the truncation errors of
563 vertical advective fluxes and thus reduces vertical numerical mixing. The layer distribution in adjacent
564 water columns is coupled by lateral adjustment of layer heights and interface positions.

565 In addition, an optional isopycnal tendency, based on estimating the positions \hat{z} of prescribed target
566 densities $\hat{\rho}$ from a truncated Taylor series $\hat{z} = z + (\hat{\rho} - \rho) / \partial_z \rho$, aligns the layers with isopycnals and thus
567 reduces the spurious diapycnal mixing of tracers due to explicit and numerical along-layer mixing in the
568 model. Furthermore, an isopycnal alignment of the layers reduces internal pressure gradient errors (see
569 Sec. 7.2). It should be noted, that pure isopycnal coordinates are not appropriate for coastal ocean models,
570 because of the relatively large mixed layers according to (2.1).

571 Gräwe et al. (2015) demonstrated the clear advantages of adaptive coordinates compared to σ -coordinates
572 in a realistic state-of-the-art model application with different dynamical regimes (tidal/non-tidal parts, sea-
573 sonal thermocline / permanent halocline).

575

576 **5 Choices for barotropic-baroclinic mode-splitting and wetting & drying**

577 Due to the presence of a free surface, fast surface gravity waves are part of the numerical solution,
578 and in shallow areas of the domain drying and flooding is possible, see (2.2). Both issues require special
579 numerical techniques that will be outlined in the following two subsections.

580 *5.1 Barotropic-baroclinic mode splitting*

581 Within the EVD-treatment (see Section 4.2.3) the layer-integrated continuity equation (A.1) serves as a
582 diagnostic equation for the grid-related vertical velocities $w_{k+1/2}^s$, and the layer heights h_k are determined
583 in terms of the total water depth D and the free surface elevation η . In this case a prognostic equation for
584 the free surface elevation must be derived from the vertical sum of the layer-integrated continuity equation
585 (A.1) and consideration of the kinematic boundary conditions (3.9a) and (3.9b):

$$586 \quad \partial_t(\eta + H) = \partial_t D = \partial_t \left(\sum_{k=1}^{k_{\max}} h_k \right) = -\partial_x \left(\sum_{k=1}^{k_{\max}} h_k u_k \right) - \partial_y \left(\sum_{k=1}^{k_{\max}} h_k v_k \right) - (E - P). \quad (5.1)$$

587 The direct numerical integration of the set (5.1) and (A.1)–(A.5) is possible. However, the compu-
588 tational costs can be significantly reduced by a barotropic-baroclinic mode-splitting, based on different
589 time-stepping of the barotropic mode associated with fast surface gravity waves, and the remaining baro-
590 clinic dynamics. Within an explicit temporal discretisation the time step of the barotropic mode is strongly
591 constrained by the celerity of shallow water surface gravity waves (Beckers and Deleersnijder, 1993),
592 whereas the much slower baroclinic motions can be integrated with an $\mathcal{O}(10^1)$ times larger time step.
593 Therefore, a split-explicit mode-splitting (see e.g. Simons, 1974, and Section 5.1.2) is based on the prog-
594 nostic integration of the barotropic mode by a series of smaller time steps carried out during one baroclinic
595 time step. Alternatively, a (formal) split-implicit mode-splitting (see e.g. Madala and Piacsek, 1977, and
596 Section 5.1.1) avoids the explicit time step constraint due the fast surface gravity waves by treating the
597 transports in (5.1), and the surface slopes in (A.2) and (A.3) implicitly.

598

599

600 Both methods have their own merits and complications.

601 *5.1.1 Split-implicit mode-splitting*

602 Following the θ -scheme of Casulli and Cattani (1994) the set (5.1), (A.2) and (A.3) can be solved
603 simultaneously, with the transports in (5.1) being temporally weighted such that they are between the

604 levels of the old and the new surface elevation, and equivalently, with η in (A.2) and (A.3) being temporally
605 between the old and new transports. Insertion of (A.2) and (A.3) into (5.1) gives an elliptic system for η
606 with a matrix of dimension $N \times N$ with N denoting the number of free-surface grid boxes. Depending on
607 the treatment of the Coriolis terms (explicit or implicit), each row of the matrix has 5 or 9 non-zero entries,
608 such that the matrix is very sparse. One of the challenges for solving these large systems of equations is to
609 find accurate (typically iterative) solvers which are efficient also on massively parallel high-performance
610 computers. An early example for a semi-implicit coastal ocean model including semi-implicit treatment
611 of the Coriolis term has been presented by Backhaus (1985).

612 To avoid the requirement of solving one large elliptic system, a directional-split method had been intro-
613 duced by Peaceman and Rachford (1955), in which in an alternating manner the equations are solved along
614 one and then along the other coordinate direction implicitly. This method is called Alternating Directions
615 Implicit (ADI). Many models in coastal engineering had adopted this approach (see, e.g., Pietrzak et al.,
616 2002). While ADI is easier to handle computationally, additional errors due to the directional splitting
617 have to be considered.

618 The advantage of the (formal) split-implicit mode-splitting is the relatively easy coupling between the
619 modes, since both are computed with the same time step. In case of ADI, the baroclinic equations (A.1),
620 (A.4), (A.5) and other tracer equations must be stepped forward consistent to the directional-split stepping
621 of (5.1). A disadvantage of implicit schemes is the demanding computation of large and sparse linear
622 system on parallel computers. While the scheme with $\theta = 0.5$ is energy-conserving (but still sensitive to
623 instabilities arising from the discretisation of other terms), a larger degree of implicitness ($\theta \rightarrow 1$) stabilises
624 the scheme, a procedure which however for larger time steps might become too dissipative (Walters et al.
625 (2009)). In tidal or tsunami simulations this sets a practical limitation to the overall model time step.

626 5.1.2 Split-explicit mode-splitting

627 In order to prognostically integrate the barotropic mode in a series of smaller time steps constrained by
628 the celerity of shallow water surface gravity waves, an additional set of equations must be derived. Usually
629 the slightly depth-dependent barotropic mode is approximated by the depth-integrated equations (also
630 called external mode), given by (5.1) and the vertical sum of the layer-integrated momentum equations
631 (A.2) and (A.3):

$$632 \quad \partial_t \eta + \partial_x (D\bar{u}) + \partial_y (D\bar{v}) = -(E - P), \quad (5.2a)$$

$$633 \quad \partial_t (D\bar{u}) + \partial_x (D\bar{u}\bar{u}) + \partial_y (D\bar{v}\bar{u}) \\ 634 \quad = D\tilde{F}_x^h(D, \bar{u}, \bar{v}) + \tau_x^s(\bar{u}, \bar{v}) - \tau_x^b(D, \bar{u}, \bar{v}) + fD\bar{v} - gD\partial_x \eta - D\frac{1}{\rho_0}\partial_x p_a + S_x, \quad (5.2b)$$

$$637 \quad \partial_t (D\bar{v}) + \partial_x (D\bar{u}\bar{v}) + \partial_y (D\bar{v}\bar{v}) \\ 638 \quad = D\tilde{F}_y^h(D, \bar{u}, \bar{v}) + \tau_y^s(\bar{u}, \bar{v}) - \tau_y^b(D, \bar{u}, \bar{v}) - fD\bar{u} - gD\partial_y \eta - D\frac{1}{\rho_0}\partial_y p_a + S_y, \quad (5.2c)$$

641 with the water depth,

$$642 \quad D \equiv \sum_{k=1}^{k_{\max}} h_k, \quad (5.3)$$

643 the barotropic transports,

$$644 \quad [D\bar{u}, D\bar{v}] \equiv \sum_{k=1}^{k_{\max}} [h_k u_k, h_k v_k], \quad (5.4)$$

645 and the barotropic-baroclinic interaction terms:

$$\begin{aligned}
646 \quad S_{[x,y]} = & \quad \partial_x (D\bar{u}[\bar{u}, \bar{v}]) & - \sum_{k=1}^{k_{\max}} \partial_x (h_k u_k [u_k, v_k]) \\
647 & + \partial_y (D\bar{u}[\bar{u}, \bar{v}]) & - \sum_{k=1}^{k_{\max}} \partial_y (h_k u_k [u_k, v_k]) \\
648 & - D\tilde{F}_{[x,y]}^h(D, \bar{u}, \bar{v}) & + \sum_{k=1}^{k_{\max}} h_k \tilde{F}_{[x,y]}^h(h_k, u_k, v_k) \\
649 & - \tau_{[x,y]}^s(\bar{u}, \bar{v}) & + \tau_{[x,y]}^s(u_{k_{\max}}, v_{k_{\max}}) \\
650 & + \tau_{[x,y]}^b(D, \bar{u}, \bar{v}) & - \tau_{[x,y]}^b(h_1, u_1, v_1) \\
651 & & + \sum_{k=1}^{k_{\max}} h_k F_{[x,y],k}^{\text{IPG}}. \quad (5.5) \\
652 & &
\end{aligned}$$

653 The remaining 3D equations (A.1)–(A.5), as well as the turbulence closure equations (section 3.2) and
654 other tracer equations such as biogeochemical model equations represent the internal (baroclinic) mode.
655 With (5.3), (5.4) and (5.5) the splitting into external and internal mode equations is exact. But, as men-
656 tioned above, it does not exactly separate the slightly depth-dependent fast barotropic dynamics from the
657 slow baroclinic ones. Therefore, the time-stepping of the internal mode might still be constrained by some
658 fast dynamics. Besides that, since the surface elevation and the barotropic transports are provided by the
659 external mode, an explicit temporal discretisation of the internal mode is not constrained by the celerity of
660 the fastest surface gravity waves anymore.

661 In order to provide a reasonable free surface elevation and barotropic transports for updating the internal
662 mode from stage n to stage $n+1$, the external mode is integrated explicitly within a subcycle of M_{\max} time
663 steps from stage $n,0$ to stage n, M_{\max} . The timestep of the external mode is Δt_{2D} , whereas the internal mode
664 is integrated with a larger internal timestep $\Delta t_{3D} = M \Delta t_{2D}$ with $M \leq M_{\max}$.

665 It is easy and accurate to discretise the external mode (5.2a)–(5.2c) with an explicit-in-time solver.
666 In the following a time-staggered two-level scheme is outlined. Staggering in time between the surface
667 elevations and the barotropic transports would still guarantee second-order in time accuracy. This would
668 be achieved by subsequently calculating the surface elevation and the barotropic transports with using
669 the newly updated transports and elevations on the right hand sides (except for the barotropic-baroclinic
670 interaction terms; see below). In the following the focus will be on volume and tracer mass conservation.
671 Therefore, the discretisation of the momentum equations will be not presented in detail. A time-staggered
672 discretisation of the free-surface equation (5.2a) is given by:

$$\begin{aligned}
673 \quad & \frac{\eta^{n,m+1} - \eta^{n,m}}{\Delta t_{2D}} + \partial_x (D\bar{u})^{n,m+1/2} + \partial_y (D\bar{v})^{n,m+1/2} \\
674 & & = - (E - P)^{n,m+1/2} \quad (5.6) \\
675 & & \\
676 & &
\end{aligned}$$

677 Following Shchepetkin and McWilliams (2005) a filtered surface elevation is provided to the internal

678 mode,

$$679 \quad \langle \eta \rangle^{n+1} \equiv \sum_{m=0}^{M_{\max}} a_m \eta^{n,m}, \quad (5.7)$$

681 with normalised filter weights $\sum_{m=0}^{M_{\max}} a_m = 1$. If the initial surface elevation of each external mode cycle
682 is reset to $\eta^{n,0} \equiv \langle \eta \rangle^n$, the compatible surface elevation equation resolved by the internal mode can be
683 derived from (5.6) as

$$684 \quad \frac{\langle \eta \rangle^{n+1} - \langle \eta \rangle^n}{\Delta t_{3D}} + \partial_x \langle \langle D\bar{u} \rangle \rangle^{n+1/2} + \partial_y \langle \langle D\bar{v} \rangle \rangle^{n+1/2}$$

$$685 \quad \quad \quad = - \langle \langle E - P \rangle \rangle^{n+1/2} \quad (5.8)$$

688 with

$$689 \quad \langle \langle \psi \rangle \rangle^{n+1/2} \equiv \sum_{m=0}^{M_{\max}-1} b_m \psi^{n,m+1/2} \quad (5.9)$$

691 and $b_m \equiv \frac{1}{M} \sum_{m'=m+1}^{M_{\max}} a_{m'}$. The general filter applied in (5.7) offers different types of filtering. Deleer-
692 snijder (1993) proposed to provide the instantaneous surface elevation $\langle \eta \rangle^{n+1} = \eta^{n,M}$ and averaged
693 barotropic transports $\langle \langle [D\bar{u}, D\bar{v}] \rangle \rangle^{n+1/2} = \sum_{m=0}^{M-1} [D\bar{u}, D\bar{v}]^{n,m+1/2}$ to the internal mode. This treatment
694 corresponds to $M_{\max} = M$, $a_m = \delta_{mM}$, $b_m = 1$ and involves no reset of the external quantities, i.e.
695 $\eta^{n+1,0} = \eta^{n,M}$ and $[D\bar{u}, D\bar{v}]^{n+1,0-1/2} = [D\bar{u}, D\bar{v}]^{n,M-1/2}$. In order to stabilise the retained fast dynamics
696 within the internal mode and to prevent aliasing errors Griffies (2007) suggested to provide an averaged
697 surface elevation $\langle \eta \rangle^{n+1} = \frac{1}{2M+1} \sum_{m=0}^{2M} \eta^{n,m}$ to the internal mode, obtained by $M_{\max} = 2M$, $a_m = \frac{1}{2M+1}$
698 and $b_m = \frac{2M-m}{M(2M+1)}$. Non-uniform filter weights, centered around $m = M < M_{\max}$, were presented by
699 Shchepetkin and McWilliams (2005) to offer more frequency-selective filtering.

700 Volume conservation requires that the layer-integrated continuity equation (A.1) in the internal mode,

$$701 \quad \frac{h_k^{n+1} - h_k^n}{\Delta t_{3D}} + \partial_x (h_k u_k)^{n+1/2} + \partial_y (h_k v_k)^{n+1/2} + (w_{k+1/2}^{s,n+1/2} - w_{k-1/2}^{s,n+1/2}) = 0, \quad (5.10)$$

703 recovers (5.8) when vertically summed. Thus

$$704 \quad \sum_{k=1}^{k_{\max}} h_k^{n+1} \equiv \langle \eta \rangle^{n+1} + \langle H \rangle^{n+1} = \langle D \rangle^{n+1}, \quad (5.11a)$$

$$705 \quad \sum_{k=1}^{k_{\max}} [h_k u_k, h_k v_k]^{n+1/2} \equiv \langle \langle [D\bar{u}, D\bar{v}] \rangle \rangle^{n+1/2}, \quad (5.11b)$$

$$706 \quad w_{k_{\max}+1/2}^{s,n+1/2} \equiv \langle \langle E - P \rangle \rangle^{n+1/2}. \quad (5.11c)$$

708 Compatibility condition (5.11b) is fulfilled by shifting the velocity profiles $[u_k, v_k]^{n+1/2,*}$ obtained from
709 the baroclinic momentum equations (A.2) and (A.3):

$$711 \quad [u_k, v_k]^{n+1/2} = [u_k, v_k]^{n+1/2,*}$$

$$712 \quad + \left(\langle \langle [D\bar{u}, D\bar{v}] \rangle \rangle^{n+1/2} - \sum_{k=1}^{k_{\max}} [h_k u_k, h_k v_k]^{n+1/2,*} \right) / \langle D \rangle^{n+1/2}. \quad (5.12)$$

713

714 It should be noted again, that for tracer mass conservation the discrete tracer equations must recover
715 (5.10) for constant tracers. Therefore, the shifting of velocity profiles must be done before the grid-related
716 vertical velocity is diagnosed from (5.10) and the tracer equations are integrated. At the end of each in-
717 ternal timestep, the interaction-terms (5.5) can be updated in terms of $\langle\langle[D\bar{u}, D\bar{v}]\rangle\rangle^{n+1/2}$, $[h_k u_k, h_k v_k]^{n+1/2}$
718 and $F_{[x,y],k}^{\text{IPG},n+1}$. Since these interaction-terms are held constant over the next external subcycle, integrating
719 the barotropic transports from $(D\bar{u})^{n+1,0-1/2}$ to $(D\bar{u})^{n+1,M_{\text{max}}-1/2}$, a time lag is introduced. It should be
720 noted that the barotropic-baroclinic interaction terms provide a correction to the corresponding temporally-
721 resolved barotropic terms in (5.2b) and (5.2c). Thus, the barotropic terms updated during the external sub-
722 cycle only provide a tendency, whereas the interaction terms consider the more accurate estimates based
723 on the vertically resolved quantities from the last internal time stage. Due to the strong non-linearity (see
724 Section 2.2) and fast response time (see Section 2.4) of the coastal ocean, in particular the advection and
725 drag terms in (5.2b) and (5.2c) are not kept constant (in contrast to many large-scale ocean models).

726 5.2 Drying and flooding

727 In many coastal areas intertidal flats are an important topographic feature. During high water those
728 areas are inundated and during ebb tide they may fall dry, approaching zero water depth $D \rightarrow 0$, but never
729 becoming negative. To understand how this is reflected in the mathematical formulations for coastal ocean
730 dynamics, it is instructive to reformulate the depth-integrated continuity equation (5.2a) :

$$731 \quad \partial_t D + \bar{u} \partial_x D + \bar{v} \partial_y D = -(\partial_x \bar{u} + \partial_y \bar{v}) D - (E - P). \quad (5.13)$$

732 The form (5.13) demonstrates positivity of the water depth, because its total derivative depends on a sink
733 term which vanishes for decaying water depth. The divergence stays bounded, because for frictionally
734 dominated regimes the depth-integrated momentum equations (5.2b) and (5.2c), and the quadratic bed
735 friction (7.15) guarantee bounded depth-mean velocities. The evaporation E which reduces the water
736 depth also vanishes for vanishing water depth.

737 Various ways have been proposed in coastal ocean models to guarantee the two major properties (i)
738 volume conservation (for incompressible flow) according to (5.2a) and (ii) positivity according to (5.13),
739 also numerically.

740 Volume conservation can easily be achieved by a Finite-Volume discretisation of (5.2a). Positivity
741 of the water depth requires some more care. Since any direct manipulation (e.g. clipping) of the water
742 depth violates volume and tracer conservation, in most coastal ocean models the barotropic transports in
743 (5.2a) are modified in a physical sound and reasonable way instead. For a semi-implicit barotropic model
744 Stelling and Duinmeijer (2003) suggested to treat (5.2a) as an advection equation for the water depth and
745 to approximate D at the interfaces of a water column according to positive-definite advection schemes.
746 However, in an explicit discretisation as (5.6) this treatment seems to be inconsistent, as the barotropic
747 transports are already known.

748 Therefore various approaches have been developed, all of them leaving a thin film of water in dry water
749 columns, where the dynamics is manipulated in some way to avoid further drying towards zero or negative
750 water depth. Of course any manipulation to the barotropic momentum equations must also be considered
751 in the baroclinic ones in order to guarantee consistency of the barotropic and baroclinic transports. In early
752 coastal ocean models (Flather and Heaps, 1975; Backhaus, 1976, 1985; Junglauss and Backhaus, 1994), a
753 number of rules were defined on how to reduce fluxes out of a water column when the application of these
754 fluxes would lead to negative water depth (or the undercut of a prescribed minimum water depth). Also

755 the wetting and drying schemes of Oey (2005) and Warner et al. (2013) are based on this principle. The
 756 method works reliably, but it has to be taken into account that reduction or shut-off of fluxes around one
 757 water column would change the net fluxes into the neighboring columns, such that an iterative procedure
 758 might become necessary. This problem has been partially solved by Warner et al. (2013), by shutting off
 759 transports around a water column when the water depth at the old time step is below the critical depth,
 760 see also Defne and Ganju (2015) who simulated a large lagoonal back-barrier estuary at the US east coast
 761 including extensive intertidal flats. Moreover, the direct correction of fluxes might in some models lead
 762 to spatially and temporally oscillating patterns of dry and wet water columns. Furthermore, shutting on
 763 and off transports instantaneously could lead to complications in turbulence closure models, since the bed
 764 stress which largely determines the eddy viscosity profiles (via the turbulent kinetic energy and the macro
 765 length scale of turbulence, see section 3.2.1) would be suddenly switched on or shut off regularly.

766 In some models (e.g., Casulli and Cattani, 1994) the water depth at the transport points of a C-grid is
 767 chosen as the minimum depth between the adjacent pressure points, with the consequence that velocities
 768 feel the shallow water and bed friction strongly reduces the volume transport. This however might lead to
 769 significantly delayed drying and flooding processes (Burchard and Bolding, 2002).

770 In order to avoid explicit switching on or off of transports in drying water columns, Burchard et al.
 771 (2004) (see also Burchard and Bolding, 2002) proposed the following measures when calculating the
 772 layer-integrated momentum equations:

- 773 • A critical water depth D_{crit} , and a minimum water depth, D_{min} are defined with $D_{\text{crit}} > D_{\text{min}}$ (see
 774 fig. 3). Typical values would be $D_{\text{crit}} = 0.2 \text{ m}$ and $D_{\text{min}} = 0.05 \text{ m}$. To simplify the dynamics in
 775 very shallow water with $D < D_{\text{crit}}$, many terms in the momentum equations are reduced by a factor
 776 linearly decreasing between 1 (for $D = D_{\text{crit}}$) and 0 (for $D = D_{\text{min}}$), which basically reduces the
 777 local dynamics to an external pressure gradient - friction balance. Such a balance supports reduction
 778 of local transports, since the friction coefficient calculated from the law of the wall increases towards
 779 infinity for the water depth converging towards zero, see equation (7.15).
- 780 • Additionally, when the surface elevation in one water column is below the bottom coordinate plus
 781 the minimum depth in any adjacent column (which often happens at steep bathymetry in shallow
 782 water and relatively coarse horizontal resolution, see fig. 3, where $\eta_{i+1,j} < -H_{i,j} + D_{\text{min}}$), a virtual
 783 surface elevation is defined from which the external pressure gradient ($\partial_x \eta, \partial_y \eta$) is calculated. In
 784 that case, $\tilde{\eta}_{i+1,j} = \max\{\eta_{i+1,j}, -H_{i,j} + D_{\text{min}}\}$, and the surface elevation gradient is calculated as
 785 $(\tilde{\eta}_{i+1,j} - \eta_{i,j})/\Delta x$. In the extreme case shown in fig. 3 water volume would actually flow against the
 786 elevation gradient, because $\eta_{i,j} < -H_{i,j} + D_{\text{min}}$.
- 787 • Despite the above measures, direct reduction or shut-off of transports surrounding a water column
 788 may still be necessary at singular locations. To stabilise the drying and flooding algorithm, increasing
 789 the minimum and critical water depth is often a preferred option.

790 Using these algorithms Gräwe et al. (2016) could carry out a stable and multi-annual simulation of the
 791 entire Wadden Sea of the South-Eastern North Sea at a horizontal resolution of 200 m.

792 **6 Treatment of open boundary conditions and model nesting**

793 Coastal ocean models focus on limited areas of interest and thus data are needed to force the models at
 794 open boundaries, see Section 2.5. The data can typically come from an external source (e.g. climatology,
 795 coarser resolution run on a wider domain) following a one-way (coarse \rightarrow fine) approach. In comparison,

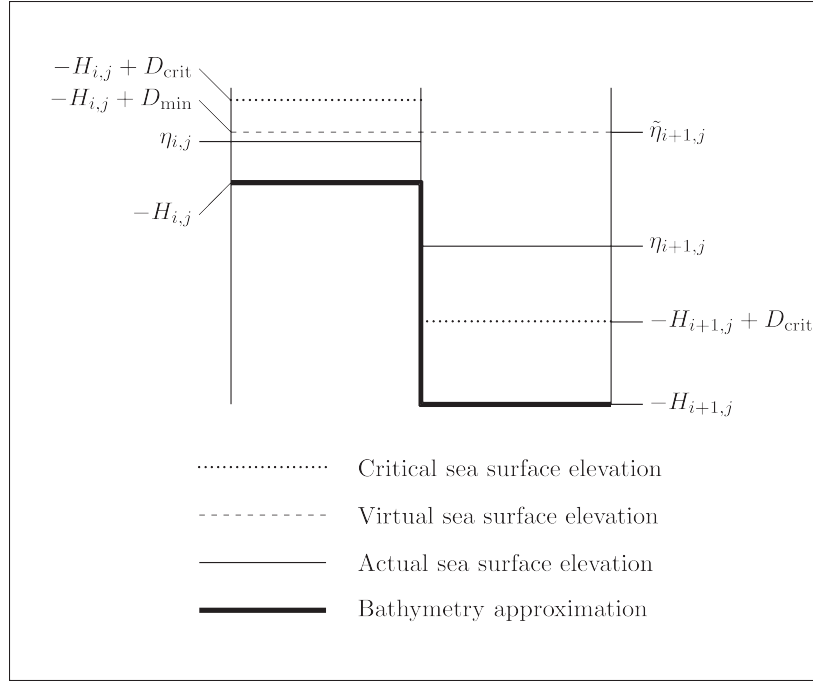


Fig. 3. Sketch explaining the geometry of bathymetry and surface elevation approximations for drying and flooding measures. This figure has been modified from Burchard et al. (2004).

796 in a two-way approach, the external data (a numerical model) feel the local coastal solution through a feed-
 797 back term. Local and external models generally differ on several key points among them grid resolution
 798 (in space and time) and physics. Across the interface, inflow and outflow can occur. In the case of inflow
 799 conditions, the quality of the local solution is strongly dependent on the quality of external data while in
 800 the case of outflow, the main issue is to prevent wave reflection at the interface. A two-way approach helps
 801 in maintaining some consistency between local and external solutions, at least when the physics of the
 802 two models are close. In both one-way and two-way approaches, the design of the boundary conditions
 803 must be carefully done. Due to the complexity of the physics, the scale heterogeneity in space and time,
 804 ideal boundary conditions are not achievable and a reasonable choice relies on a compromise between
 805 accuracy and robustness. Section 6.1 briefly introduces the general framework. Section 6.2 treats the prob-
 806 lem of model forcing in a one-way approach (open boundary conditions). Section 6.3 introduces two-way
 807 approaches.

808 6.1 General framework

We consider a domain Ω_{loc} embedded in a domain Ω_{ext} as shown in Figure 4. The local and external solutions, ϕ_{loc} and ϕ_{ext} , are integrated according to

$$\partial_t \phi_{loc} + L_{loc}(\phi_{loc}) = f_{loc} \text{ in } \Omega_{loc}, \quad \partial_t \phi_{ext} + L_{ext}(\phi_{ext}) = f_{ext} \text{ in } \Omega_{ext}.$$

L_{loc} and L_{ext} are spatial differential operators, f_{loc} and f_{ext} model forcings. ϕ is the vector of prognostic state variables. The models interact through a transition area Γ that, depending on the boundary conditions, may be restricted to a single interface γ .

Let Δx_{loc} and Δx_{ext} (resp. Δt_{loc} and Δt_{ext}) be the grid (resp. time) steps on Ω_{loc} and Ω_{ext} . Today, the availability of global/regional operational or reanalysis products allows to consider the case where typical

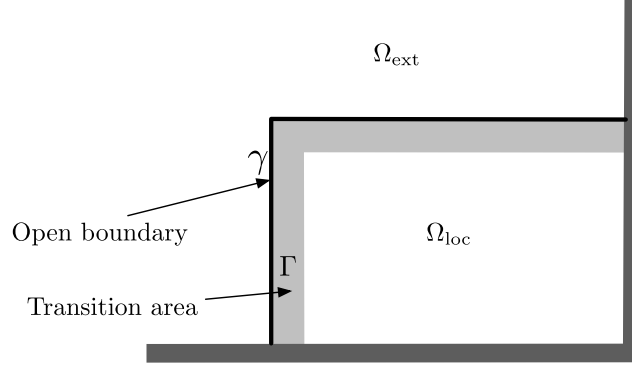


Fig. 4. The local domain Ω_{loc} embedded in the exterior domain Ω_{ext} . Ω_{loc} has an artificial interface γ and possibly a transition area Γ on which boundary conditions are prescribed.

values of time/grid steps obey:

$$\frac{\Delta x_{\text{ext}}}{\Delta x_{\text{loc}}} \approx \frac{\Delta t_{\text{ext}}}{\Delta t_{\text{loc}}} \approx 2 - 10.$$

809 Note that we won't consider the case where the vertical extent of the local domain does not cover the
 810 whole water column. Indeed, vertical parameterizations (see Section 3.2.1), coupling between barotropic
 811 and baroclinic modes (see Section 5.1) become cumbersome if only part of the water column is computed
 812 on the local grid.

813 The model interactions across the interface γ and/or within the transition area Γ are described in the
 814 next Sections.

815 6.2 Open boundary conditions (OBC) and one-way interaction

816 We start with a description of the two main classes of OBC methods: relaxation methods which aim
 817 to relax the local solution towards the external solution within the transition area Γ and radiation methods
 818 which propagate out the information to prevent waves reflection. Simple radiation methods are appropri-
 819 ate only for a first-order scalar equation, the extension to general hyperbolic systems using a character-
 820 istic variables approach is explained in Section 6.2.2. Advanced open boundary conditions like Perfectly
 821 Matched Layer (PML) and Absorbing Boundary Conditions (ABC) (see Nataf, 2013) will not be discussed
 822 here since their derivations require very simplified problems and they have still to be validated in realis-
 823 tic applications. For a review of open boundary conditions, the reader is referred to Palma and Matano
 824 (2000); Blayo and Debreu (2005).

825 The open boundary conditions presented in the next paragraphs can also be used for one-way nested mod-
 826 els (i.e. when the external data comes from a coarse resolution run). One-way nesting may be performed
 827 online (Penven et al., 2006) or offline (Mason et al., 2010). The key element for a choice between these
 828 two approaches is the spatio-temporal variability of the boundary conditions. When this variability is high,
 829 online nesting, with high frequency / high resolution exchanges between local and external domains, is
 830 more efficient. Indeed storage and performance issues limit the frequency/resolution of the outputs made
 831 during the coarse resolution run. However in an offline approach, the obvious advantage is that the area

832 covered by the local (high resolution) domain does not have to be known in advance, i.e. before running
 833 the external (coarse resolution) model.

834 6.2.1 Relaxation and radiation methods

6.2.1.1 Relaxation methods Basic Dirichlet (a.k.a. clamped) boundary conditions do not perform well (except for certain basic equations): this abrupt forcing generates inconsistencies and discontinuities near the interface γ . The flow relaxation scheme (FRS) (Davies, 1976) relaxes the interior solution towards external data in the transition area Γ near the boundary and can be written under the following relaxation (or nudging) form (Martinsen and Engedahl, 1987) (considering ϕ as a scalar variable and omitting the model forcing):

$$\partial_t \phi_{\text{loc}} + L_{\text{loc}}(\phi_{\text{loc}}) = -\frac{1}{\tau}(\phi_{\text{loc}} - \phi_{\text{ext}}) \quad \text{in } \Omega_{\text{loc}}, \quad (6.1)$$

835 The right hand side of (6.1) is the relaxation term. τ is a relaxation time scale. $\lambda = \frac{1}{\tau}$ is a positive function,
 836 which decreases away from the lateral boundary γ and vanishes outside of Γ . At the discrete level, the
 837 right hand side of (6.1) can be discretized implicitly in time to remove associated stability constraints.
 838 It is difficult to prescribe the size of the transition area Γ and the variation of λ within Γ , since they
 839 depend on the space and time scales of the phenomena (Kållberg, 1977). Typical profiles of λ are based
 840 on quadratically or exponentially decreasing functions of the distance to the boundary γ .

Due to the smallness of the coastal model domain, it may also happen that the large scales of the solution are better reproduced in the external domain Ω_{ext} . It is particularly the case when the external model makes use of data assimilation techniques (reanalysis product or operational forecast). In this situation, there is a potential benefit to relax the large scales of the local solution to the ones computed by the external model while the small scales features are still governed by the coastal model evolution. To this aim, spectral nudging methods (Waldron et al., 1996) can be viewed as a FRS scheme which acts on the whole local domain on specified (large) scales. It can be written under the following form:

$$\partial_t \phi_{\text{loc}} + L_{\text{loc}}(\phi_{\text{loc}}) + \Lambda(\phi_{\text{loc}} - \phi_{\text{ext}}) = 0 \quad \text{in } \Omega_{\text{loc}}, \quad (6.2)$$

841 where the operator Λ is now a low pass filter acting on the whole Ω_{loc} domain. The expression of Λ may
 842 be based on Fourier transform of $(\phi_{\text{loc}}, \phi_{\text{ext}})$ (with relaxation coefficients fixed in the Fourier space), on
 843 Gaussian correlation kernels and more simply on iterative Laplacian smoothing. When applied to coastal
 844 modelling, the nudging term is usually reduced near the coast where the external model may have a coarser
 845 representation of the coastline.

Finally, most of the time, the FRS scheme is associated to a sponge layer that damps the small scales near the boundary using increased viscosity/diffusivity ν :

$$\partial_t \phi_{\text{loc}} + L_{\text{loc}}(\phi_{\text{loc}}) = -\frac{1}{\tau}(\phi_{\text{loc}} - \phi_{\text{ext}}) + \nu_{\Gamma} \Delta \phi_{\text{loc}} \quad \text{in } \Omega_{\text{loc}}, \quad (6.3)$$

846 where Δ is the Laplacian operator.

6.2.1.2 Radiation methods In the case of outflow conditions, the FRS scheme will only behave well (and in particular will prevent waves reflection) when the external data is already an accurate representation of the solution. In other cases, radiation methods can be used to propagate out the disturbances. The basic

radiation methods solve the Sommerfeld radiation condition (6.4) at the interface,

$$\partial_t \phi_{\text{loc}} + c \partial_n \phi_{\text{loc}} = 0 \quad \text{on } \gamma, \quad (6.4)$$

and corresponds to the transport of ϕ through γ at the phase speed projected to the boundary, c (∂_n denotes a derivative perpendicular to and towards the outside of the boundary). Obviously this boundary condition is only exact for a transport equation and when c is known. In practice, c ($= -\partial_t \phi_{\text{loc}} (\partial_n \phi_{\text{loc}})^{-1}$) is estimated at the discrete level using internal values (Orlanski, 1976), leading to different implementations, including, in two dimensions, variants taking into account tangential derivatives (Raymond and Kuo, 1984). Besides the evaluation of the phase speed c , the relevancy of this type of boundary condition for non-monochromatic and/or dispersive waves is questionable.

The radiation condition is valid only for outflow conditions (e.g. $c > 0$ at an eastern boundary). In other cases, relaxation methods as described in the previous paragraph are more appropriate. Radiation and relaxation methods can be combined to give:

$$\partial_t \phi_{\text{loc}} + c \partial_n \phi_{\text{loc}} = -\frac{\phi_{\text{loc}} - \phi_{\text{ext}}}{\tau_\gamma} \quad \text{on } \gamma. \quad (6.5)$$

847 where τ_γ , the relaxation time scale, has different values $\tau_{\text{in}}, \tau_{\text{out}}$ according to inflow ($\tau_\gamma = \tau_{\text{in}}$) or outflow
 848 ($\tau_\gamma = \tau_{\text{out}}$) conditions (Marchesiello et al., 2001). During inflow conditions c is set to zero and τ_{in} is small
 849 leading to a strong relaxation towards external solution. τ_{out} is large but not infinity in order to prevent
 850 the internal solution to drift for external data. Note that even if (6.5) is written at the interface γ , it is
 851 most of the time associated to a relaxation term active on the whole transition area Γ . For consistency, the
 852 boundary value of the relaxation time scale τ defined in (6.1) should be greater than τ_{out} .

853 6.2.2 Characteristic methods

As mentioned previously, radiation methods are only valid when the temporal evolution of the state variable is governed by a first-order hyperbolic equation. They can be extended to more general cases by looking at the hyperbolic parts of the equations. By definition hyperbolic systems can be decomposed into a series of first-order scalar hyperbolic equations whose solutions are the characteristic variables. The problem is then well posed if the incoming characteristics variable are specified and the outgoing characteristic extrapolated from internal values.

Considering a one-dimensional version of the linearised barotropic equation

$$\partial_t \eta = -H \partial_x \bar{u}, \quad \partial_t \bar{u} = -g \partial_x \eta,$$

the two characteristics are given by

$$w_\pm = \bar{u} \pm \sqrt{\frac{g}{H}} \eta$$

and propagate with speeds $c_\pm = \pm \sqrt{gH}$ (i.e. $\partial_t w_\pm + c_\pm \partial_x w_\pm = 0$). At open boundaries, the incoming characteristics are prescribed ($w_{\text{loc}} = w_{\text{ext}}$) and the outgoing characteristic are computed from internal values. The computation of outgoing characteristic variables at the boundary can be based on simple extrapolation techniques or on the application of upwind biased schemes. It is well known that the specification of the incoming characteristics of the barotropic equations is equivalent to the Flather boundary condition (Flather, 1976) (which can also be obtained by a Sommerfeld radiation condition for \bar{u} , with $c = \sqrt{gH}$, and a 1D version of the continuity equation). At an eastern boundary where $w_- = \bar{u} - \sqrt{\frac{g}{H}} \eta$

must be prescribed, the Flather boundary condition reads

$$\bar{u} = \bar{u}_{\text{ext}} + \sqrt{\frac{g}{H}} (\eta - \eta_{\text{ext}}) \quad (6.6)$$

and η is given by another boundary condition (e.g. $\partial_x \eta = 0$).

The use of the full characteristic method gives instead:

$$\bar{u} = \frac{1}{2} (w_{+, \text{int}} + w_{-, \text{ext}}) = \frac{1}{2} (\bar{u}_{\text{ext}} + \bar{u}_{\text{int}}) + \frac{1}{2} \sqrt{\frac{g}{H}} (\eta_{\text{int}} - \eta_{\text{ext}}) \quad (6.7)$$

and

$$\eta = \frac{1}{2} \sqrt{\frac{H}{g}} (w_{+, \text{int}} - w_{-, \text{ext}}) = \frac{1}{2} (\eta_{\text{ext}} + \eta_{\text{int}}) + \frac{1}{2} \sqrt{\frac{H}{g}} (\bar{u}_{\text{int}} - \bar{u}_{\text{ext}}), \quad (6.8)$$

854 where $w_{+, \text{int}} = \bar{u}_{\text{int}} + \sqrt{\frac{g}{H}} \eta_{\text{int}}$ is computed from internal values. The Flather type boundary condition
 855 (6.6), or some of its variants, is used in most of the coastal ocean models where it is assumed that surface
 856 gravity waves are indeed dominant for the specification of the boundary conditions. If \bar{u}_{ext} is not known
 857 but only η_{ext} (e.g. tidal conditions), a reduced model (e.g. geostrophic balance) may be used to deduce
 858 \bar{u}_{ext} .

859 At the discrete level, the computation (extrapolation) of $\bar{u}_{\text{int}}, \eta_{\text{int}}$ in (6.7) has to be done with care. A
 860 stable implementation of (6.7) on a staggered C -grid is described in Mason et al. (2010).

861 6.2.3 3D models

862 The 3D primitive equation models support the propagation of internal gravity waves. In an idealized
 863 framework, their characteristics can be obtained through a vertical normal mode decomposition. Setting
 864 3D boundary conditions on the original state variables without taking into account these propagations
 865 renders the problem ill-posed (Oliger and Sundström, 1978). A remedy can be to add a small vertical
 866 viscosity in the hydrostatic balance equations (3.2) (Témam and Tribbia, 2003). Characteristics-based
 867 methods can formally be extended to 3D-based on a vertical mode decomposition (Jensen, 1998; Blayo
 868 and Debreu, 2005) resulting into a series of shallow water models. However the number of assumptions
 869 used in their derivations (in particular the linearisation around a horizontally constant background density
 870 field and a constant background state velocity field, typically the barotropic solution) make them difficult
 871 to apply in practice. That is why, in 3D primitive equation models, the preceding relaxation/radiation
 872 boundary conditions are usually applied on each of the prognostic variables (u, v, Θ, S), with a Flather-
 873 like boundary condition for the barotropic part.

874

875 6.3 Two-way interaction

876 We consider now a two-way interaction between the external and local models. The external model
 877 feels the local model by a feedback of the local solution. We differentiate between traditional two-way
 878 nesting algorithms where the local domain corresponds to a local grid refinement of the external domain
 879 and more general two-way coupling algorithms.

880 We will not detail here the interpolation/update operators between the two models. The reader is referred
 881 to Debreu and Blayo (2008) for their design, in particular in terms of scale selectivity and conservation.

882 6.3.1 Two-way nesting

883 Two-way nesting algorithms have been reviewed in Debreu and Blayo (2008). In this paragraph, we
884 describe strongly coupled models which eventually can be viewed as a single model with an abrupt change
885 of resolution at the high/coarse resolution grids interface γ .

6.3.1.1 Grid interactions In two-way nesting applications, the feedback from the high to the coarse resolution grid prevents the two solutions to drift. In the limit of equal local and external grid resolutions ($L_{\text{ext}} = L_{\text{loc}}$) the original solution (without nesting) should be recovered. This implies a strong criterion on the forcing of the local model: the boundary conditions have to act on the difference between external and local solutions. We will call this a consistency condition. Typically, the sponge layer in (6.3) should now be written

$$\partial_t \phi_{\text{loc}} + \dots = \nu_{\Gamma} \Delta(\phi_{\text{loc}} - \phi_{\text{ext}}) \quad \text{in } \Omega_{\text{loc}}, \quad (6.9)$$

and if radiation conditions are used, (6.5) should be replaced by:

$$\partial_t(\phi_{\text{loc}} - \phi_{\text{ext}}) + c \partial_n(\phi_{\text{loc}} - \phi_{\text{ext}}) = -\frac{\phi_{\text{loc}} - \phi_{\text{ext}}}{\tau}. \quad (6.10)$$

886 In a sense, in these equations, the temporal and spatial scales of the external solutions are not assumed to
887 be much larger than those of the local domain so that the simplification occurring in (6.3) and (6.5) cannot
888 be made. Condition (6.10) was used in Perkins et al. (1997).

889 6.3.1.2

6.3.1.3 Vertical grids In coastal applications, the capacity to change locally the vertical coordinate systems (see Section 4.2) can become crucial for some applications. Indeed, mesh refinement along coastal areas with very small water depths may require some local adaptation of the parameters of the vertical coordinate systems (parameters of the terrain-following coordinates, number of layers, ...). In that case, vertical remapping has to be applied between coarse and fine grids.

6.3.1.4 Time refinement In traditional applications, horizontal mesh refinement is most of the time coupled with time refinement in order to satisfy stability conditions. If the main stability constraint is given by external gravity waves propagation (cf 5.1), at a velocity of \sqrt{gH} , we may expect that, when refining the grid near the coast and so with smaller depths, the time step does not have to be reduced. This is certainly the case for some applications, but generally having the possibility to refine the time steps may become important when the actual time step is constrained by other phenomena (e.g. drying and flooding, advection ...).

902 6.3.2 Two-way coupling

903 Less strong local/external coupling may also be of interest, particularly when the space and time re-
904 finement factors are large and/or if the models L_{ext} and L_{loc} have different physics. In that case, two-way
905 relaxation methods may also be of interest. The spectral nudging method introduced in Section 6.2.1.1
906 can be extended to two-way interactions. The smooth semi-prognostic method (Sheng et al., 2005) is
907 an example of such a technique. More generally, grids interactions can be (weakly) incorporated in any
908 assimilation scheme coupling at the same time the assimilation of observations and the grid interactions.

913 **7 Numerical treatment of single terms and processes**

914 This section discusses discrete algorithms that are commonly used for the solution of the governing
 915 equations formulated in Sec. 3 and 4. Originally, coastal ocean models were discretised using numerical
 916 methods loosely inherited from large scale ocean models, namely second-order in space and Leapfrog-in-
 917 time schemes (Blumberg and Mellor, 1987). However, over the years, the numerics of those models have
 918 evolved toward the use of more advanced discretisation techniques, more similar to techniques used in
 919 other fields of computational fluid dynamics, in order to accommodate to the specific constraints of coastal
 920 applications (see Sec. 2). The diversity of methods in use in coastal models is large so that the discussion
 921 can only focus on techniques which are more widely used or are expected to become more widely used. For
 922 the sake of simplicity and since the numerical requirements for each process can be rather different, this
 923 section considers separately sub-systems of the full system of primitive equations. However, it should not
 924 overshadow the fact that a numerical kernel must be designed as a whole, not just as an advection or a wave
 925 propagation equation since interferences between numerical methods used for different processes exist ;
 926 e.g. the numerics for pure gravity waves must be chosen under the constraint to be stable for the Coriolis
 927 term (Beckers and Deleersnijder, 1993; Walters et al., 2009), or time-stepping optimized for gravity waves
 928 are not always the best for advection and Coriolis, and inversely (e.g Shchepetkin and McWilliams, 2005).

929 Generally speaking, discretisation techniques in most existing structured-grid oceanic coastal models
 930 can be classified as finite volume discretisations. The arrangement on the computational grid is shown in
 931 Fig. 1. We now give more details on the specifics of different terms.

932 *7.1 Tracer and momentum advection*

933 In coastal ocean models, tracers must be interpreted in a finite-volume sense, meaning that for a given
 934 quantity q the discrete quantity $q_{i,j,k}$ is the average over a control volume $\mathcal{V}_{i,j,k}$ (Fig. 1). As far as momen-
 935 tum advection is concerned, in contrast to large-scale models which generally prefer a vector invariant
 936 form for nonlinear advection terms (which facilitates the conservation of quantities like potential vorticity,
 937 enstrophy and/or kinetic energy; see e.g. Arakawa and Lamb (1977)), coastal models generally adopt a
 938 conservative form inherited from Lilly (1965). Momentum advection terms in Lilly (1965) can be viewed
 939 as a finite-volume discretisation provided that proper horizontal metric terms are added. We, thus, con-
 940 sider here a generic advection equation written in a conservative way for a layer-averaged quantity q_k
 941 (q can either represent a tracer or horizontal momentum components) according to (4.2) along with the

942 continuity equation (A.1)

$$\partial_t(h_k q_k) + \partial_x(h_k u_k q_k) + \partial_y(h_k v_k q_k) + \delta_k(w^s q) = 0,$$

943

(7.1)

$$\partial_t h_k + \partial_x(h_k u_k) + \partial_y(h_k v_k) + \delta_k(w^s) = 0,$$

944 using the notations introduced in Sec. 4 and the definition of a vertical difference located at the centre of
945 the cell k , $\delta_k(a) = a_{k+1/2} - a_{k-1/2}$ for any quantity a . We retain the continuity equation here to emphasize
946 that the advection equation must be conservative while satisfying a constancy preservation property (i.e.
947 if q is initialised with a constant, it remains so). An overview of the time and space discretisations of (7.1)
948 used in large and mesoscales oceanic models can be found in Griffies et al. (2000) or Lemarié et al. (2015).

949 7.1.1 Method of lines vs coupled space and time approach

950 In practice, several strategies to discretize (7.1) coexist in the coastal community. A first choice is
951 to consider simple second-order centered schemes supplemented by an explicit diffusion and a non-
952 dissipative time-stepping algorithm in order to ensure energy consistency of the whole code at a dis-
953 crete level (Marsaleix et al., 2008). A second choice is to rely exclusively on standard high-order upwind
954 schemes in the horizontal direction and weakly-dispersive centered advection schemes in the vertical (e.g.
955 fourth-order compact schemes), without any explicit dissipation, combined with a high-order predictor-
956 corrector time-stepping algorithm using a method of lines (e.g. Shchepetkin and McWilliams, 2005). In
957 this case, it is accepted that strong gradients will generate overshoots and undershoots and that there is
958 an uncontrolled sink of kinetic energy and tracer variance in the model caused by dissipative truncation
959 errors. As an alternative to the method of lines, where space and time discretisations are considered sepa-
960 rately, a coupled space-time approach³ could be used for advective terms (e.g. Hundsdorfer and Trompert,
961 1994; Daru and Tenaud, 2004). This type of approach can be viewed as a conservative semi-Lagrangian
962 approach where the characteristics are tracked in space-time. The resulting schemes are one-step schemes
963 with interfacial fluxes depending on the local Courant number $\alpha = \mathbf{u}\Delta t/(\Delta x, \Delta y, \Delta z)$, with \mathbf{u} the veloc-
964 ity vector. They have the property to be free of computational mode, and to be easily extended to arbitrary
965 high-order of accuracy with minimum stencil (e.g. Daru and Tenaud, 2004). Examples of such schemes
966 are the first-order upwind scheme, the Lax-Wendroff scheme or the QUICKEST scheme which are re-
967 spectively first, second and third order accurate in space and time. Whatever the strategy used (method of
968 lines or coupled space and time), it is generally preferable to prevent spurious numerical oscillations by
969 imposing non-oscillatory constraints which are computationally demanding but provide a way to ensure
970 nonlinear stability, as described in the next paragraph.

971 7.1.2 Nonlinear stability and flux correcting/limiting methods

972 Since non-oscillatory schemes, which are seldom used in large-scale models, are expected to be in-
973 creasingly used to simulate coastal flows at very high-resolution, we provide comments on this point to
974 highlight the associated delicacies. Numerical methods with an order of accuracy larger than one are prone
975 to numerical oscillations. A nonlinear stability criteria often considered is that the numerical solution must
976 not oscillate without bounds. Using the notion of total variation (TV) as a measure of the overall amount of

³ The coupled space and time approach is also known in the literature as flux-form semi-Lagrangian approach, as well as transient interpolation method, or direct space-time discretisation.

977 oscillations, numerical schemes have been constructed to ensure that the total variation is either bounded
 978 (TVB) or diminishing (TVD) (Harten, 1983; Shu, 1987). Since TVD schemes necessarily degenerate to
 979 first order accuracy near smooth extrema, they are prone to clipping errors manifested by the appearance of
 980 a flat plateau in the solution due to an excess of diffusion. To avoid this type of error, a less stringent con-
 981 straint is the monotonicity-preservation (MP) which relaxes the TVD constraint near extrema (e.g. Suresh
 982 and Huynh, 1997; Daru and Tenaud, 2004). Flux correcting/limiting is generally used to impose the TVD,
 983 TVB or MP stability conditions (e.g. Durran, 2010). Historically, the flux limiting/correcting methods
 984 were derived in a coupled space and time framework using the second-order Lax-Wendroff scheme. They
 985 can be easily extended to higher-order accuracy using one-step coupled time-space approach of arbitrary
 986 high order (e.g. Daru and Tenaud, 2004). However if a method of lines is used the time and space dimen-
 987 sions are decoupled therefore the constraints on total variation must be imposed both in time and space.
 988 For this purpose, a family of Runge-Kutta (RK) schemes satisfying the TVD property has been derived
 989 by Shu (1988) and Gottlieb and Shu (1998). Note that a consequence of the TVD, TVB and MP stability
 990 constraints is a better control of numerical oscillations hence those constraints could be used not only for
 991 momentum advection as a way to limit spurious mixing by reducing the grid Reynolds number (Ilicak
 992 et al., 2012), but also for the advection of tracers and layer thickness subject to monotonicity or posi-
 993 tivity constraints. There is an abundant literature on the comparison of different flux limiting/correcting
 994 strategies, see Mohammadi-Aragh et al. (2015) for a recent study in the oceanic modelling context.

995 7.1.3 Multidimensional aspects and stability constraints

996 The properties of advection schemes in terms of stability and accuracy are generally studied in 1D. The
 997 extension of one-dimensional schemes to multi-dimensions in the context of a method of lines is straight-
 998 forward since the necessary transverse terms are discretised in a transparent way. If a quasi-Eulerian ver-
 999 tical coordinate is used, the stability constraint in three dimensions reads

$$1000 \quad \alpha^x + \alpha^y + \beta\alpha^z \leq \alpha^*, \quad (\alpha^x, \alpha^y, \alpha^z) = \mathbf{u}\Delta t / (\Delta x, \Delta y, \Delta z) \quad (7.2)$$

1001 where α^* is the CFL stability constraint associated to the numerical schemes used for the time and space
 1002 , and β a coefficient arising from the fact that different advection schemes with different stability criteria
 1003 may be used in the horizontal and vertical directions. As far as the coupled space and time approach is
 1004 concerned, a simple application of the one-dimensional fluxes in each spatial direction would result in a
 1005 scheme that can be at most first-order accurate, whatever the order of accuracy of the 1D fluxes, and the
 1006 scheme would be unconditionally unstable. To overcome this issue a directional splitting can be used to
 1007 introduce the necessary transverse terms in the discretisation. A simple method to introduce transverse
 1008 terms while preserving constancy (e.g. Bott, 2010) corresponds to the following steps to advance from
 1009 time n to time $n + 1$

$$\begin{aligned}
 (h_k q_k)^* &= (h_k q_k)^n - \Delta t \delta_k (w^s q_k^n) \\
 h_k^* &= h_k^n - \Delta t \delta_k (w^s) \\
 (h_k q_k)^{**} &= (h_k q_k)^* - \Delta t \partial_x (u_k (h_k q_k)^*) \\
 h_k^{**} &= h_k^* - \Delta t \partial_x (h_k^* u_k) \\
 (h_k q_k)^{n+1} &= (h_k q_k)^{**} - \Delta t \partial_y (v_k (h_k q_k)^{**}) \\
 h_k^{n+1} &= h_k^{**} - \Delta t \partial_y (h_k^{**} v_k)
 \end{aligned}$$

1010

where the discrete form of the ∂_x and δ_k operator is given by any coupled space and time scheme. The order of integration in the different direction must be permuted at each time-step to further reduce splitting errors. With this type of approach the stability constraint is given by

$$\max \{\alpha^x, \alpha^y, \alpha^z\} \leq 1$$

1011 which is less stringent than (7.2).

1012 For coastal applications, Shchepetkin (2015) has emphasised the severe stability constraint potentially
 1013 imposed by an explicit treatment of vertical advection. Several ways can be used to mitigate this issue: (i)
 1014 use a semi-implicit advection scheme; (ii) use a local time-step for vertical advective terms based on the
 1015 maximum vertical Courant number in each water column; (iii) use a quasi-Lagrangian vertical coordinate
 1016 which is subject to a gentle Lipschitz stability condition rather than the usually severe CFL condition (e.g.
 1017 James, 2000; White et al., 2009). This last remark applies to models using rezoning/remapping strategies
 1018 because models using a transport algorithm instead of remapping (e.g. Hofmeister et al., 2010) will still
 1019 be subject to a CFL type stability constraint.

1020 7.2 Internal pressure gradient term

1021 In coastal ocean models with bottom-following coordinates (see Sec. 2.1 and Sec. 4.2.2), the coor-
 1022 dinate surfaces may intersect with isopycnal or geopotential surfaces at a relatively large angle when the
 1023 bathymetry is steep. This makes it significantly harder to accurately compute the internal pressure gra-
 1024 dient force $F_{[x,y],k}^{\text{IPG}}$ defined in (4.5) since the buoyancy integrals $I_b(z) = \int_z^\eta b(x, y, z') dz'$ are not directly
 1025 available along constant horizontal surfaces. Using the notations introduced in Sec. 4, for a generalised
 1026 vertical coordinate s , the x -component of the corresponding gradient can be alternatively expressed using
 1027 the chain rule

$$1028 \quad (\partial_x I_b)_z = (\partial_x I_b(z))_s + b (\partial_x z)_s. \quad (7.3)$$

1030 The subscript s is denoting differentiation with respect to constant s . In an arbitrary general coordinate the
 1031 two terms in rhs are nontrivial, of opposite sign and may be large compared to the order of magnitude of
 1032 their difference.. The second term in the rhs in (7.3) is sometimes referred to as compensating hydrostatic
 1033 term which vanishes for geopotential coordinates ($s = z$).

1034 7.2.1 Discretization of horizontal pressure gradient term

1035 At a discrete level, unbalanced truncation errors in the computation of the two large terms in the rhs
 1036 of (7.3) will interfere with each other and give rise to a possibly large pressure-gradient error leading to
 1037 hydrostatic inconsistency manifested by unphysical spontaneous motions. A very large body of literature is
 1038 dedicated to this subject (e.g. Blumberg and Mellor, 1987; Mellor et al., 1994; McCalpin, 1994; Burchard
 1039 and Petersen, 1997; Lin, 1997; Shchepetkin and McWilliams, 2003; Adcroft et al., 2008; Marsaleix et al.,
 1040 2011; Berntsen, 2011) where different strategies have been followed to reformulate (7.3) in a way more
 1041 convenient for the discretisation. Those strategies are generally motivated either by achieving a high-
 1042 order accuracy to cancel the two terms in (7.3) in the case of a flat stratification (e.g. McCalpin, 1994;
 1043 Shchepetkin and McWilliams, 2003) or by ensuring an energetic consistency (e.g. Marsaleix et al., 2008).
 1044 In this latter case, the aim is to make sure in a discrete sense that the change of kinetic energy due to the

1045 work of pressure forces is balanced by the change of potential energy due to buoyancy forces. This balance
 1046 occurs only with a linear equation of state and involves the discrete advection for density (e.g. Shchepetkin
 1047 and McWilliams, 2003, App. A).

Mainly three strategies have been followed in practical applications to reformulate and discretise (7.3).
 (i) A first strategy is to directly use (7.3).

When discretising this form of pressure gradient, averaging of $I_b(z)$ in the vertical and b in the horizontal
 are needed since the only term computed at its natural position is $(\partial_x z)_s$. According to Shchepetkin and
 McWilliams (2003) this explains why this approach is often prone to large hydrostatic inconsistencies.
 However, high-order schemes have been proposed in McCalpin (1994) to compute the horizontal deriva-
 tives and horizontal averaging of b combined with a spectral representation in the vertical. (ii) a second
 and intuitive approach consists in computing $I_b(z)$ and then to vertically interpolate the result at an hori-
 zontal surface of reference before differentiating (e.g. Lin, 1997; White et al., 2009). This is the preferred
 option in atmospheric models. In Lin (1997) a flux-form finite-volume approach based on this concept is
 adopted. (iii) the preferred approach for most oceanic models is to use a *density-Jacobian* discretisation.
 With the Leibniz rule we easily obtain that

$$(\partial_x I_b)_z = b(\eta)\partial_x \eta + \int_z^\eta \underbrace{[(\partial_x b)_s - \partial_{z'} b (\partial_x z')_s]}_{\mathcal{J}_{x,z'}(b,z')} dz'. \quad (7.4)$$

1048 Compared to the straight-forward approach (7.3) differentiation comes first and integration then. The
 1049 density-Jacobian formulation clearly shows that if $s = \rho$ only one term is nonzero and the pressure gradient
 1050 term can be computed accurately provided that proper care is taken to the equation of state (Adcroft et al.,
 1051 2008). The Jacobian in (7.4) must be computed at cell corners, if we refer to Fig. 5 a standard second-order
 1052 discretisation reads

$$(\mathcal{J}_{x,z})_{i+1/2,k+1/2} = \frac{1}{2\Delta x} \left\{ (1+r_x)b_{i+1,k+1} + (1-r_x)b_{i+1,k} \right. \\ \left. - (1-r_x)b_{i,k+1} - (1+r_x)b_{i,k} \right\} \quad (7.5)$$

1053
 1054 with $r_x = -\frac{z_{i+1,k+1/2} - z_{i,k+1/2}}{z_{i+1/2,k+1} - z_{i+1/2,k}} = -(\Delta x/\Delta z)(\partial_x z)_s$ the grid slope. This discretisation of the Jacobian has
 1055 been widely used in coastal models for years. It can be shown that the standard second-order Jacobian
 1056 discretisation corresponds to a discrete form of Green's theorem since (7.5) can be written as the sum of
 1057 four line integrals discretised using a simple trapezoidal rule. Shchepetkin and McWilliams (2003) have
 1058 introduced a high-order (cubic) discretisation for those line integrals. The resultant scheme turned out to
 1059 be a significant step forward compared to existing approaches.

1060 Besides the imbalance in the truncation errors in (7.3) there is an other source of pressure gradient error
 1061 stemming from the use of a nonlinear equation of state including compressibility of seawater (Dukowicz,
 1062 2001). Ways to remove this source of error by rearranging the terms in the equation of state are presented
 1063 in Shchepetkin and McWilliams (2003), Adcroft et al. (2008) or Marsaleix et al. (2011). This latter source
 1064 of error is sometimes overlooked, however it must be stressed that the careless inclusion of compressibility
 1065 terms into the equation of state would have significant dynamic consequences.

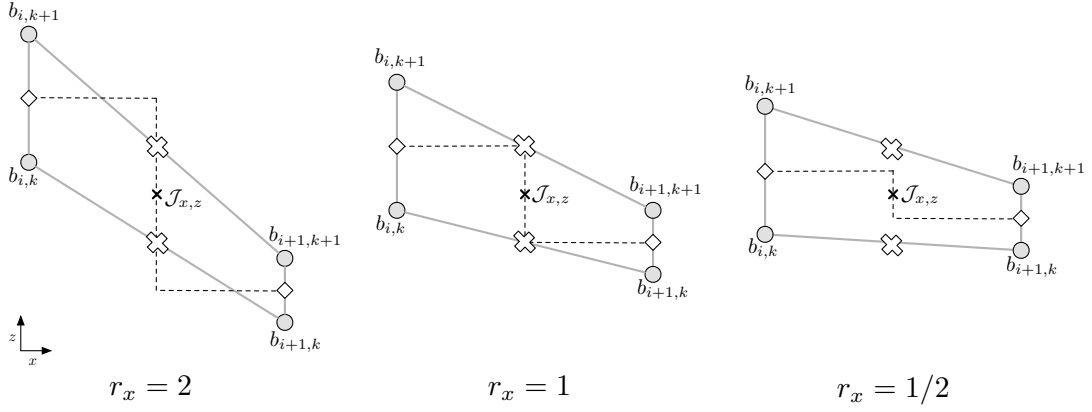


Fig. 5. Elementary computational stencil of the standard second-order density Jacobian $\mathcal{J}_{x,s}$ for different values of the grid slope r_x . The quantity $|r_x|$ geometrically corresponds to the vertical distance between the two white diamonds (located at $z_{i,k+1/2}$ and $z_{i+1,k+1/2}$) divided by the distance between the two white crosses (located at $z_{i+1/2,k}$ and $z_{i+1/2,k+1}$).

1066 7.2.2 Control of pressure gradient discretization errors

Following Mellor et al. (1994), a simple form of the truncation error, neglecting the horizontal derivatives involving buoyancy, associated to discretization (7.5) can be expressed as

$$\mathcal{E}_{\text{ipg}} = \frac{(\partial_x H)_s}{4H} \left\{ \Delta z^2 - \Delta x^2 (\partial_x z)_s^2 \right\} \left(\partial_z^2 b + \frac{1}{3} z \partial_z^3 b \right) + \mathcal{O}(\Delta x^4, \Delta z^4, \Delta x^2 \Delta z^2) \quad (7.6)$$

1067 in the case of a separable σ coordinate. The expression for \mathcal{E}_{ipg} shows that the leading order error vanishes for $r_x = \pm 1$ (i.e. $\Delta z = \pm \Delta x (\partial_x z)_s$), for $r_x = 0$ (i.e. $\partial_x H = 0$) and for a linear buoyancy profile
1068 $(\partial_z^m b = 0, m \geq 2)$. Provided that sufficient computational power is available, (7.6) also shows that refining
1069 jointly the horizontal and vertical resolution is an obvious way to reduce IPG errors. More generally,
1070 the value of the parameter r_x in (7.5) is usually considered a good qualitative indicator of discretisation
1071 errors. For $|r_x| \leq 1$ the discretisation is expected to be fairly accurate since it is based on vertical inter-
1072 interpolations, this is the so-called "hydrostatic consistency" situation (Fig. 5). Values of $|r_x|$ greater than
1073 1 generally lead to a degradation of the accuracy due to the need of vertical extrapolation to compute the
1074 pressure gradient term. This corresponds to a situation of "hydrostatic inconsistency", see Haney (1991).
1075 However, this notion of "hydrostatic consistency" has to be considered with care since in general the actual
1076 discretization error of IPG discretizations does not behave monotonically with r_x . As emphasized by
1077 Mellor et al. (1994), the error compensation between the two terms in curly brackets in (7.6) can lead
1078 to smaller errors in hydrostatic inconsistency situations (typically for $|r_x|$ slightly larger than 1) than in
1079 hydrostatic consistency situations (for r_x around 1/2). A usual requirement to avoid the emergence of
1080 spurious motions is to keep the value of r_x and/or of the slope parameter $\Delta x |(\partial_x H)_s|$ at a reasonable level.
1081 To do so several ways are commonly used concurrently: (i) bathymetry smoothing (e.g. Martinho and
1082 Batteen, 2006) is systematically used in terrain-following coordinates to limit the maximum slopes; (ii)
1083 the function responsible for the vertical placement of grid points is designed in such a way to minimise
1084 the departure of the vertical coordinate isosurfaces from the horizontal direction (e.g. Schär et al., 2002;
1085 Shchepetkin and McWilliams, 2009b; Berntsen, 2011; Lemarié et al., 2012b) or alternatively use a mixed
1086 z - s coordinate transformation to flatten the vertical levels in predefined sub-domains (e.g. Deleersnijder
1087 and Beckers, 1992; Burchard and Petersen, 1997; Shapiro et al., 2013); (iii) a quasi-Lagrangian vertical
1088 coordinate whose layer distribution in the rezoning step can be chosen to reduce grid slopes or to fol-
1089

1090 low isopycnals (e.g. White et al., 2009; Hofmeister et al., 2010; Leclair and Madec, 2011). Besides the
 1091 approaches discussed so far, we could imagine alternative strategies. For example, the coordinate system
 1092 could be determined using only the low-frequency variations in the bathymetry and high frequencies could
 1093 be handled using an immersed boundary method (e.g. Lundquist et al., 2010). Other alternatives could be
 1094 the use of well-balanced discretisations (Botta et al., 2004) or to express horizontal momentum using
 1095 the covariant velocity components instead of the usual contravariant components (Weller and Shahrokhi,
 1096 2014). Eventually, as emphasised by Mellor et al. (1994), the interaction between pressure gradient and
 1097 other terms in the equations should be further clarified, especially the interaction with active tracers ad-
 1098 vection.

1099

1100

1101 7.3 Coriolis term (inertial oscillations)

1102 In the absence of other terms but Coriolis terms in (A.2) and (A.3) we obtain the equations of free
 1103 motion on a rotating plane

$$1104 \quad \partial_t(h_k u_k) = f h_k v_k; \quad \partial_t(h_k v_k) = -f h_k u_k. \quad (7.7)$$

1105 A characteristic of the Coriolis acceleration is that it is directed perpendicular to the velocity direction.
 1106 Hence, it does not play any role in the kinetic energy budget, which forms an important constraint for the
 1107 discretisation (e.g. Arakawa and Lamb, 1977). In (7.7), the quantity $f h_k v_k$ must be given at u -points and
 1108 $f h_k u_k$ at v -points. If (7.7) is semi-discretised in space, this constraint is trivially satisfied locally on an
 1109 Arakawa B-grid, since u and v are collocated, but can only be satisfied globally on an Arakawa C-grid.
 1110 Considering that the Coriolis frequency f is cell centered ⁴, the following discretisation of the rhs in (7.7)

$$1111 \quad (f h_k v_k)_{i+1/2,j} = \overline{f_{i,j} h_{i,j,k} v_k^y}^x, \quad (f h_k u_k)_{i,j+1/2} = \overline{f_{i,j} h_{i,j,k} u_k^x}^y, \quad (7.8)$$

1112 where $\overline{\quad}^m$ is an averaging operator in the direction m ($m = x, y$), ensures that all the terms associated to the
 1113 Coriolis force cancel when a kinetic energy equation is derived from (A.2) and (A.3) (Sec. III.C in Arakawa
 1114 and Lamb, 1977). In (7.8), the horizontal variations of the curvature metric terms have been ignored for
 1115 clarity. An alternative energetically-neutral discretisation providing a different logic for the cancellation
 1116 of the terms when the kinetic energy budget is formed at the discrete level has been introduced in Espelid
 1117 et al. (2000) and reads

$$1118 \quad (f h_k v_k)_{i+1/2,j} = f_{i+1/2,j} \overline{(h_k v_k)_{i+1/2,j}}^w; \quad (f h_k u_k)_{i,j+1/2} = f_{i,j+1/2} \overline{(h_k u_k)_{i,j+1/2}}^w, \quad (7.9)$$

1119 where $\overline{\quad}^w$ is a weighted average defined as

$$1120 \quad \overline{(h_k v_k)_{i+1/2,j}}^w = \frac{w_{i+1/2,j,k}}{4} \sum_{n=0}^{n=1} \sum_{m=0}^{m=1} \frac{(h v)_{i+n,j-m+1/2,k}}{w_{i+n,j-m+1/2,k}}; \quad w_{i+1/2,j,k} = \sqrt{\frac{g h_{i+1/2,j,k}}{|f_{i+1/2,j}|}}$$

⁴ In most coastal models, the Coriolis frequency is cell-centered while in large-scale models it is often located at cell-corners since it is required to use potential enstrophy conserving discretization schemes.

1121 for each layer k , same rationale applies to $\overline{(h_k u_k)}_{i,j+1/2}^w$. Compared to (7.8), this formulation requires the
 1122 Coriolis parameter to be defined at u and v points and allows more freedom in the way to define the
 1123 thickness layer h_k at cell interfaces.

1124 When the time dimension is discretised, a simple forward Euler step to integrate (7.7) would be uncon-
 1125 ditionally unstable. The use of a (semi)-implicit scheme would remove stability constraints. This approach
 1126 is essentially adopted in models which treat the gravity waves in a semi-implicit way (e.g. Walters et al.,
 1127 2009). In general, for coastal applications, the baroclinic time-step is much smaller than the inertial period
 1128 meaning that the Coriolis term is not expected to impose any limitation on the time-step. For this reason
 1129 explicit schemes are generally preferred. To circumvent the stability issues of the Euler forward step, a
 1130 Forward-Backward in Time (FBT) approach is often used (Bleck and Smith, 1990)

$$(h_k u_k)_{i+1/2,j}^{n+1} = (h_k u_k)_{i+1/2,j}^n + \Delta t (f h_k v_k)_{i+1/2,j}^{n+m} \quad (7.10)$$

$$(h_k v_k)_{i+1/2,j}^{n+1} = (h_k v_k)_{i+1/2,j}^n - \Delta t (f h_k u_k)_{i,j+1/2}^{n+1-m},$$

1132 and is stable for $f \Delta t \leq 2$. In (7.10), m is either 0 if n is even or 1 otherwise. Other popular explicit
 1133 schemes to integrate (7.7) include the third-order Adams-Bashforth scheme (stable for $f \Delta t \leq 0.72$) and
 1134 the leapfrog scheme (stable for $f \Delta t \leq 1$).

1135 1136 7.4 Internal gravity waves

1137 Elements about the temporal discretization of external gravity waves are introduced in Sec. 5.1 so that
 1138 we focus here on internal gravity waves. The numerical integration of those waves can be studied using
 1139 the following two-dimensional subsystem of equations (3.1), (3.3), (3.10), (3.12)

$$\begin{aligned} \partial_x u + \partial_z w &= 0 \\ \partial_t u + (g/\rho_0) \partial_x \left(\int_z^0 \rho \, dz' \right) &= 0 \\ \partial_t \rho + \partial_x (u \rho) + \partial_z (w \rho) &= 0 \end{aligned} \quad (7.11)$$

1141 which represents the interactions between momentum and tracer equations, assuming a linear equation
 1142 of state. Historically, in large-scale and coastal models based on leapfrog time-stepping a very popular
 1143 scheme to integrate (7.11) was the pressure gradient averaging (a.k.a. Shuman averaging) approach of

1144 Brown and Campana (1978) which corresponds to the following steps

$$\begin{aligned}
 w^n &= \int_{-H}^z \partial_x u^n dz' \\
 \rho^{n+1} &= \rho^{n-1} - 2\Delta t \partial_x (u^n \rho^n) - 2\Delta t \partial_z (w^n \rho^n) \\
 u^{n+1} &= u^{n-1} - 2(\Delta t / \rho_0) \partial_x \left(\int_z^0 \left[\frac{1}{2} \rho^n + \frac{1}{4} (\rho^{n-1} + \rho^{n+1}) \right] dz' \right)
 \end{aligned}
 \tag{7.12}$$

1146 where the weights in the averaging are chosen to allow the larger stability constraint. For coastal models
 1147 based on 2-level (one-step) time-stepping the simpler strategy is the so-called forward-backward approach
 1148 (e.g. Mesinger and Arakawa, 1976)

$$\begin{aligned}
 w^n &= \int_{-H}^z \partial_x u^n dz' \\
 \rho^{n+1} &= \rho^n - \Delta t \partial_x (u^n \rho^n) - \Delta t \partial_z (w^n \rho^n) \\
 u^{n+1} &= u^n - (\Delta t / \rho_0) \partial_x \left(\int_z^0 \rho^{n+1} dz' \right)
 \end{aligned}
 \tag{7.13}$$

1150 In the same spirit as (7.13), the time staggering of tracers and momentum equations (e.g. Backhaus, 1985)
 1151 provides an efficient scheme since it allows some implicitness in the coupling between the two equations.
 1152 All the schemes discussed so far are second-order accurate and lead to the following stability constraint
 1153 on a staggered C-grid

$$\alpha_{\text{igw}} = \Delta t \sqrt{c_1^2 \left(\frac{1}{\Delta x^2} + \frac{1}{\Delta y^2} \right)} \leq 1$$

where c_1 is the speed of the fastest internal wave which can be as large as 3.8 m s^{-1} . Same stability
 constraint is obtained if the order of integration between momentum and tracer equations is reversed in
 (7.12) and (7.13).

1155 The forward-backward and pressure gradient averaging approaches provide a good combination of ef-
 1156 ficiency, simplicity and large stability range for internal gravity waves integration, with less emphasis on
 1157 accuracy. However, as resolution keeps increasing in coastal models, a wider spectrum of internal waves
 1158 can be explicitly represented and accuracy in time and space should also be considered a priority. Better
 1159 accuracy in time can be achieved by using either high-order predictor-corrector schemes (e.g. Shchepetkin
 1160 and McWilliams, 2005), or 2-level schemes (e.g. Rueda et al., 2007; Shchepetkin and McWilliams, 2009a)
 1161 with forward-backward feedbacks between momentum and tracers equations.

1162 As far as the spatial discretisation is concerned, the overwhelming majority of oceanic models con-
 1163 sider simple second-order schemes to compute the horizontal divergence ($\partial_x u$ in (7.11)) in the continuity
 1164 equation and the horizontal pressure gradient ($\partial_x \int_z^0 \rho dz'$ in (7.11)). However studies by Blayo (2000)
 1165 and Demange et al. (2014) emphasised that higher-order approximations of those two terms would al-
 1166 low a significantly better representation of internal waves propagation, compared to standard algorithmic
 1167 choices.

1168 7.5 Orientation of diffusion tensor and numerically-induced mixing

1169 7.5.1 Orientation of diffusion tensor

1170 In (3.15), (3.17) and (3.18) the horizontal turbulent fluxes are oriented in the horizontal direction. For
1171 simplicity, in some models the diffusion terms are not transformed to non-orthogonal vertical coordinates,
1172 but replaced by diffusion along the model layers. However, in the case of a stratified flow, if the vertical
1173 coordinate $s \neq \rho$ it is well known that maintaining the tracer diffusion tensor along the coordinate lines
1174 can be responsible for non-physical mixing of water masses and associated spurious baroclinic currents
1175 (e.g. Barnier et al., 1998). It is thus relatively common for non-isopycnic models to implement a rotation of
1176 the diffusion tensor (via the rotation tensor \mathbf{R} in (3.15)) in a direction non-aligned with the computational
1177 grid (e.g. Stelling and Van Kester, 1994; Griffies et al., 1998). Since for a generalized coordinate it is
1178 expected that the slope between the isopycnal direction and the direction of the computational grid is
1179 larger than for a classical z coordinate, a good compromise is generally to rotate the explicit diffusion
1180 in the geopotential direction rather than the physically correct isopycnal direction. This allows to avoid
1181 delicacies associated with the computation of isopycnal slopes in unstratified regions and at the intersection
1182 with the surface and the bottom. Compared to standard implementations available in climate models, a
1183 rotation of the diffusion along isopycnals is not straight-forward in coastal models for several reasons,
1184 (i) at high horizontal resolution, explicit diffusion is generally handled with a biharmonic operator which
1185 is tedious to rotate, mainly for stability reasons; (ii) the rotated operators in climate models are derived
1186 under the small slope approximation which is not always satisfied in the coastal regions (e.g. Lemarié
1187 et al., 2012b, Sec. 2.4.2); (iii) because the slopes can be large in coastal applications, the rotated operator
1188 will be prone to large dispersive errors and can become inaccurate (Beckers et al., 1998, 2000; Lemarié
1189 et al., 2012a).

1190 7.5.2 Numerically-induced mixing

1191 A non negligible amount of non-physical mixing of water masses can also be due to the advection
1192 operator. Indeed, as mentioned earlier, oceanic coastal models generally rely either on high-order linear
1193 upwind schemes or on flux correcting/limiting approaches to discretise horizontal advection. The associ-
1194 ated truncation errors are dissipative. Much effort have been recently directed toward the quantification
1195 and/or modification of physical orientation of this mixing of numerical nature (e.g. Burchard and Rennau,
1196 2008; Marchesiello et al., 2009; Ilicak et al., 2012; Klingbeil et al., 2014). For example, Marchesiello
1197 et al. (2009) showed that the dissipative truncation error associated to a third-order upwind scheme in a
1198 terrain-following coordinate model was greatly exceeding the small level of physically acceptable mixing
1199 observed in the oceanic interior. The physical results proved to be greatly improved by splitting the third-
1200 order upwind scheme between a centered and a diffusive part and when the diffusive part is rotated in the
1201 isopycnal direction (Marchesiello et al., 2009; Lemarié et al., 2012b). An alternative approach to have
1202 more control on the orientation of mixing for coastal applications is the use of quasi-Lagrangian approach
1203 (e.g. Hofmeister et al., 2010; Leclair and Madec, 2011). Besides the orientation of the diffusion tensor,
1204 Ilicak et al. (2012) emphasised that spurious diapycnal mixing can be aggravated if the grid Reynolds
1205 number is too large (i.e. if the velocity field is not smooth on the grid scale). Besides advective terms and
1206 explicit diffusion operators, other components of numerical models can be a source of "numerical mixing"
1207 (e.g. Soufflet et al., 2016). For example, the time-stepping algorithms are generally diffusive (with the ex-
1208 ception of the Leapfrog scheme for which diffusion is provided via the Asselin filter), the stabilization of
1209 the time-splitting procedure between the barotropic and baroclinic modes requires extra diffusion (which

1210 takes the form of a filtering of the fast barotropic variables).

1211 7.6 Bottom friction

1212 Due to the relatively thick bottom boundary layers in the coastal ocean, see (2.1), an accurate discreti-
 1213 sation of bottom friction is required. The no-slip bottom boundary condition for u and v (3.7) is typically
 1214 not directly discretised, because a vertical resolution on scales of millimetres would be required to obtain
 1215 sufficient accuracy. Instead, it is assumed that the velocity profiles in the lowest grid box of an ocean model
 1216 follow the law of the wall:

$$1217 \quad [u(z'), v(z')] = \frac{1}{\kappa} \ln \left(\frac{z' + z_0^b}{z_0^b} \right) [u_*^b, v_*^b], \quad (7.14)$$

1218 with the bottom roughness length, z_0^b , the bottom friction velocity vector, (u_*^b, v_*^b) and the distance from
 1219 the wall, $z' = z + H$. With (7.14), the discrete bottom boundary condition (3.8) has the form of a quadratic
 1220 friction law

$$1221 \quad \tau_{[x,y]}^b(h, u, v) = \left((u_*^b)^2 + (v_*^b)^2 \right)^{1/2} [u_*^b, v_*^b]$$

$$1222 \quad = \left(\frac{\kappa}{\ln \left(\frac{h/2 + z_0^b}{z_0^b} \right)} \right)^2 (u^2 + v^2)^{1/2} [u, v]$$

$$1223 \quad = c_D (u^2 + v^2)^{1/2} [u, v]. \quad (7.15)$$

In (7.15) $\tau_{[x,y]}^b$

1225 is the bed stress vector, c_D is the non-dimensional bottom drag coefficient, h is the thickness of the lowest
 1226 grid box, and (u, v) is the velocity vector in the lowest grid box. Note that for the limit of $h \rightarrow 0$ we
 1227 obtain $c_D \rightarrow \infty$ and thus retain the original no-slip condition (3.7). In situations when the near-bottom
 1228 velocity profile deviates strongly from the law of the wall, e.g. when stratification due to high sediment
 1229 concentrations or a wave-enhanced bottom boundary layer (or both) are present, the vertical resolution
 1230 needs to be sufficiently high. One other possibility would be to parameterise such unresolved processes
 1231 (Burchard et al. (2008); Warner et al. (2008)).

1232 In order to prevent instabilities, bottom friction is treated semi-implicitly in the model. An explicit
 1233 discretisation of the layer-integrated momentum equation (A.2) in the bottom layer,

$$1234 \quad \frac{(hu)^{n+1} - (hu)^{n+}}{\Delta t} = -\tau_x^b(h, u^{n+})$$

$$1235 \quad \iff (hu)^{n+1} = \left(1 - \Delta t \frac{\tau_x^b(h, u^{n+})}{(hu)^{n+}} \right) (hu)^{n+}, \quad (7.16)$$

1238 with u^{n+} already containing all other explicit contributions, shows the constraint $\Delta t < \frac{(hu)^{n+}}{\tau_x^b(h, u^{n+})} =$
 1239 $\frac{h}{c_D |u^{n+}|}$. Thus, for high vertical resolution towards the bottom, as typically required in coastal ocean mod-
 1240 elling (see Section 2.1), the time step can become strongly constrained. In contrast, with the semi-implicit

1241 treatment

1242

$$1243 \quad \frac{(hu)^{n+1} - (hu)^{n+}}{\Delta t} = -\frac{(hu)^{n+1}}{(hu)^{n+}} \tau_x^b(h, u^{n+})$$

1244

1245

$$\iff (hu)^{n+1} = \left(1 + \Delta t \frac{\tau_x^b(h, u^{n+})}{(hu)^{n+}}\right)^{-1} (hu)^{n+} \quad (7.17)$$

1246 the final velocity monotonically tends to zero for increasing Δt , c_D or decreasing h .

1247 The source term linearisation in (7.17) is equivalent to the so-called Patankar-trick (Patankar, 1980,
1248 Sec. 7.2-2), which is usually applied to guarantee positivity of turbulent quantities and biogeochemical
1249 tracer concentrations.

1250 7.7 Numerical treatment of turbulence closure equations

1251 On a Lorenz grid (see Figure 1) discrete turbulent quantities are best located at w -points, i.e. vertically
1252 between the tracer points of adjacent layers. Although this offers the prescription of Dirichlet boundary
1253 conditions for the turbulent kinetic energy (TKE) k and its dissipation rate ε directly at the bottom and
1254 the free surface, Burchard and Petersen (1999) and Burchard et al. (2005) demonstrated, that equivalent
1255 Neumann boundary conditions provide much higher accuracy in reproducing the law of the wall.

The temporal discretisation of the prognostic equations for the non-negative scalars k and ε also re-
quires specific care. These quantities often cover several orders of magnitude across fairly short time and
spatial scales such as in oscillating tidal flow. For example, a straightforward, explicit-in-time discretisa-
tion of the TKE equation (3.19)

might require very small time steps during slack tide, when production is small and dissipation is high, in
order to guarantee positivity of k (see analogy to (7.16)).

1256 Therefore, the so-called Patankar trick (see analogous source term linearisation in (7.17)) is used in almost
1257 all discretisations of turbulence closure budget equations, including those for other parameters such as the
1258 dissipation rate ε and the turbulence frequency ω , see Deleersnijder et al. (1997) and Burchard et al. (2005)
1259 for details.

1260 Another issue of the numerical treatment of turbulence closure models is the energy-consistency be-
1261 tween mean flow and turbulence. Physically, the kinetic energy extracted from the mean flow due to ver-
1262 tical stress divergence is a source of turbulent kinetic energy transferred as shear production P . The same
1263 applies to the exchange of energy between mean potential energy and turbulence kinetic energy which is
1264 transferred as buoyancy production B . Burchard (2002b) shows how a consistent energy exchange can be
1265 obtained also on the numerical level.

1266 8 Existing coastal ocean community models

1267 Previous sections have discussed the various choices that have to be made when designing a numerical
1268 model with a focus on coastal applications. The present section gives an overview of the specifics of some
1269 existing hydrostatic and non-hydrostatic structured-grid models to illustrate the diversity of methods in
1270 use in coastal models and their evolution over the years. We have strived here to present a fair description
1271 of past and ongoing developments, however the reader must be warned that omissions and inaccuracies in
1272 the model description are inherent to this type of exercise.

1273 8.1 Hydrostatic structured-grid models

1274 In this subsection examples of structured-grid oceanic models used in practice to tackle research or
1275 engineering applications related to coastal environments are given, see Tab. 1 for a list of the most
1276 popular models historically used in this context. In this list we can find models originally designed for
1277 shallow seas applications (e.g. BOM, COHERENS, GETM, HAMSOM, Mars3D, MOHID), as well as
1278 mesoscale oceanic models (like NCOM, POLCOMS, POM or ROMS), originally designed to cover shelf
1279 seas and open ocean regions, and later adapted to handle nearshore and coastal scales (e.g. Oey, 2005;
1280 Uchiyama et al., 2010; Warner et al., 2013). More recently, global climate models (e.g. NEMO, Hy-
1281 com) are also sometimes used to study shelf processes provided some adjustments in their numerical
1282 formulation (e.g. Leclair and Madec, 2011; Lahaye et al., 2011). Finally, models specifically designed for
1283 commercial/engineering applications (e.g. Delft3D, ECOM-si, MIKE 3, TRIM3D) can also be used for
1284 real case studies (e.g. Cheng et al., 1993). As summarised in Tab. 2, the choice of discrete algorithms in
1285 oceanic models bear the imprints of their original target application and development time. In the 90's the
1286 situation was very clear: climate models were generally discretised on a B-grid using a geopotential co-
1287 ordinate under the rigid-lid assumption and leapfrog (LF) time-stepping (Griffies, 2004) while mesoscale
1288 models, largely inspired by POM, made use of a C-grid, a terrain-following coordinate and an explicit
1289 free surface. At that time coastal and engineering models were predominantly C-grid models based on
1290 a semi-implicit free surface and baroclinic forward in time methods influenced by Backhaus (1985) and
1291 Casulli and Cheng (1992). Nowadays, the distinction between the different class of models is less clear
1292 because newly developed models are generally designed to handle a larger range of spatio-temporal scales
1293 permitted by the advances in computational power and the maturity of nesting strategies (see Sec. 6). In
1294 early 2000's, the emergence of models like ROMS, GETM or Hycom came with a thorough rethinking of
1295 several model components like time-stepping algorithms (Shchepetkin and McWilliams, 2005), vertical
1296 coordinate (Bleck, 2002; Burchard and Beckers, 2004), turbulent closure schemes (Umlauf and Burchard,
1297 2003), or open boundary conditions (Marchesiello et al., 2001) which increased further the diversity of
1298 models. Tab. 2 reflects the variety of models and modelling techniques that are presently used. However
1299 some general trends can be distinguished :

- 1300 ● Models originally developed with coastal applications in mind are characterized by 2-level (one-step)
1301 time-stepping with a coupled space and time treatment of advective terms. This choice combines
1302 simplicity and ease to implement monotonicity-preserving advection.
- 1303 ● The majority of models based on a coupled space and time approach favour the superbee slope limiter
1304 to impose the TVD property. This choice corresponds to the upper boundary of the TVD region
1305 and leads to the least numerical diffusion among the existing slope limiters (e.g. Cushman-Roisin
1306 and Beckers, 2011). However, this limiter tends to erroneously amplify the gradients. According to
1307 Durran (2010), the monotonized centered limiter is expected to provide superior results in terms of

accuracy. Other flux-limiter methods currently used for practical applications is the ultimate quickest scheme (or equivalently the so-called P2-PDM scheme). Note that the WENO or FCT approaches are still relatively marginally used.

- As motivated in Sec. 3.2.1, the overwhelming majority of coastal models rely on TKE-based vertical closure models. A dynamic equation for TKE is solved either in combination with a diagnostic mixing length or with a second dynamic equation for a length related quantity.
- The recently developed models are almost exclusively based on a split-explicit mode splitting (SPE; see Section 5.1.2) which allows more accuracy in the computation of fast barotropic waves (see final paragraph in Section 5.1.2) and is expected to provide enhanced scalability and performance on parallel computers.
- The vertical coordinate system is one of the aspects that focuses the most attention nowadays. The general trend is to allow more flexibility in the definition of the coordinate within the Arbitrary Lagrangian-Eulerian framework (see Sections 4.2.3 and 4.2.4).

8.2 Non-hydrostatic models

Within the last decade several existing coastal ocean models mentioned above were extended to abandon the hydrostatic pressure assumption (POM: Kanarska and Maderich (2003), BOM: Heggelund et al. (2004), ROMS: Kanarska et al. (2007), Symphonie: Auclair et al. (2011), GETM: Klingbeil and Burchard (2013)). Scaling analysis shows that the nonhydrostatic pressure contribution, formally defined by

$$\partial_z p_{\text{nh}} = -(\partial_t w + \partial_x(uw) + \partial_y(vw) + \partial_z(wv) - f_h u - F_z), \quad (8.1)$$

cannot be neglected when approaching sufficiently high spatial resolutions that promote processes with significant vertical accelerations (Marshall et al., 1997; Klingbeil and Burchard, 2013). Practical examples on coastal ocean scales are flows above irregular topography, high-frequency internal gravity waves or gravity plumes. In order to simulate these processes in a physically correct way, the vertical momentum balance must not be degenerated to (3.2) anymore.

For solving the full set of incompressible Navier-Stokes equations algorithms were implemented on top of the hydrostatic model kernels that do not require a complete rewrite of the existing kernels. These were usually based on either the classical projection method (Chorin, 1968; Témam, 1969) or the pressure correction method (van Kan, 1986). Both methods require the solution of a Poisson equation for either the nonhydrostatic pressure (Kanarska and Maderich, 2003; Heggelund et al., 2004) or its correction (Kanarska et al., 2007; Auclair et al., 2011), which should be derived by inserting the discrete momentum equations into the discrete incompressibility condition to force a divergence-free final velocity field. The specific characteristics of coastal ocean models demand for some adaptations and care, e.g. for the consistent coupling of the free surface to the corrected nonhydrostatic velocities or for the numerical treatment of the additional diagonals in the coefficient matrix that, in general, is neither symmetric nor positive-definite due to cross-terms caused by the non-orthogonal vertical coordinate transformation. Strategies to avoid the additional diagonals were presented by Heggelund et al. (2004) and Berntsen and Furnes (2005). Following Berntsen and Furnes (2005), Keilegavlen and Berntsen (2009) demonstrated that simulations with the nonhydrostatic pressure defined directly in σ -coordinates showed no significant deviations to results obtained with the pressure defined in z -coordinates. An alternative algorithm for weakly nonhydrostatic regimes (e.g. internal lee waves) that avoids the Poisson equation was presented by Klingbeil and Burchard (2013). They treat the nonhydrostatic pressure as the hydrostatic one, i.e. diagnose the time-lagged

Model	Acronym	website
BOM	Bergen Ocean Model	http://www.mi.uib.no/BOM/
COHERENS	Coupled Hydrodynamical Ecological model for Regional Shelf seas	http://odnature.naturalsciences.be/coherens/
Delft-3D	Deltares flow	http://oss.deltares.nl/web/delft3d
ECOM-si	Estuarine, Coastal and Ocean Model (semi-implicit)	http://woodshole.er.usgs.gov/operations/modeling/ecomsi.html
GETM	General Estuarine Transport Model	http://www.getm.eu/
HAMSOM	Hamburg Shelf Ocean Model	https://wiki.zmaw.de/ifm/TO/Hamsom/modelhistory
ROMS	Regional Oceanic Modeling System	
↔ Rutgers		https://www.myroms.org/
↔ UCLA		http://research.atmos.ucla.edu/cesr/ROMS_page.html
↔ AGRIF		http://www.romsagrif.org/
Mars3D	Model for Applications at Regional Scale	http://wwz.ifremer.fr/mars3d/
MIKE 3	Danish Hydraulic Institute	https://www.mikepoweredbydhi.com/
MOHID	Modelo Hidrodinâmico	http://www.mohid.com/
NCOM	Navy Coastal Ocean Model	http://www.dtic.mil/dtic/tr/fulltext/u2/a508063.pdf
POLCOMS	Proudman Oceanographic Laboratory Coastal Ocean Modelling System	http://cobs.noc.ac.uk/modl/polcoms/
POM	Princeton Ocean Model	http://www.ccpo.odu.edu/POMWEB/
Symphonie	Sirocco Ocean Model	http://sirocco.omp.obs-mip.fr/ocean_models/S-model
TRIM-3D	Tidal Residual, Intertidal Mudflat	
Hycom	Hybrid Coordinate Ocean Model	https://hycom.org/
NEMO	Nucleus for the European Modelling of the Ocean	http://www.nemo-ocean.eu/

Table 1

Summary of most significant oceanic models historically used for applications to three-dimensional coastal studies. The ROMS code has three variants referred to as ROMS-Rutgers, ROMS-UCLA, and ROMS-Agrif (see Shchepetkin and McWilliams, 2009b, for more details). Hycom and NEMO are examples for large scale models which are also applied to the coastal ocean.

BOM	Svendsen et al. (1996)	C	SPE	LF-AM3	LF-TR	TVD Superbee	TVD Superbee	s	MY2.5
COHERENS	Luyten et al. (1999)	C	SPI/SPE	2-level	-	TVD Superbee	TVD Superbee	s	$k-\epsilon$
Delft-3D	Gerritsen et al. (2004)	C	SPI	ADI	ADI	UP3	UP3 w/ Forester fltr	z & s	$k-\epsilon$
ECOM-si	Blumberg (1992)	C	SPI	2-level	θ -scheme	C2	C2	s	MY2.5
GETM	Burchard and Bolding (2002)	C	SPE	2-level	FB	TVD	TVD	adapt.	GOTM
HAMSOM	Backhaus (1985)	C	SPI	2-level	θ -scheme	TVD	TVD	z	$k-\epsilon$
ROMS (Rutgers)	Haidvogel et al. (2000)	C	SPE	LF-TR	LF-AM3	UP3	MPDATA	s	GLS
ROMS (UCLA)	Shchepetkin and McWilliams (2005)	C	SPE	LF-AM3	Gen FB	UP3	UP3	s	KPP
ROMS (Agrif)	Penven et al. (2006)	C	SPE	LF-AM3	Gen FB	UP3	WENO5Z	s	KPP
Mars3D	Lazure and Salomon (1991)	C	SPI	2-level	ADI	QK3	QK3	s	GLS
MIKE 3	Pietrzak et al. (2002)	C	SPI	2-level	ADI	Ultimate QK3	Ultimate QK3	s	$k-\epsilon$
MOHID	Martins et al. (2001)	C	SPI	2-level	ADI	upstream	TVD Superbee	s	GOTM
NCOM	Martin (2000)	C	SPI	LF	θ -scheme	SUP3	FCT(UP3)	hyb z/s	MY2.5
POLCOMS	Holt and James (2001)	B	SPE	2-level	FB	PPM w/ limiters	PPM w/ limiters	s	GOTM
POM	Blumberg and Mellor (1978)	C	SPE	LF	LF	C2	MPDATA	s	MY2.5
Symphonic	Johns et al. (1992) Marsaleix et al. (1998)	C	SPE	LF	LF	C4	SUP3	s	TKE
TRIM-3D	Cheng et al. (1993)	C	SPI	2-level	θ -scheme	SL	TVD Van-Leer	z	GLS
Hycom	Bleck (2002)	C	SPE	LF	LF	Enstrophy-conserving	FCT(C2)	hyb $z/s/\rho$	KPP
NEMO	Madec et al. (1991)	C	SPE	LF	LF	Enstrophy-conserving	FCT(C2)	z & s	GLS

1350 right-hand side of (8.1), integrate it vertically and insert it into the horizontal momentum equations.

1351 **9 Future perspectives**

1352 The present review of the numerics of structured-grid coastal ocean models gives an overview of the
1353 numerical methods available for today's coastal ocean models. There is no single model which combines
1354 all those methods. Thus, by just recombining existing methods, today's model platforms may be further
1355 improved.

1356 But what are the future challenges in coastal ocean modelling? There are various trends which will
1357 drive further developments. One driver is certainly the ever ongoing growth of computational resources
1358 allowing for higher spatial resolution and higher-order numerical schemes, better process representations
1359 (such as for turbulence-closure models and parameterisation of surface and internal waves), integration
1360 into regional Earth system models of growing complexity, application of more elaborate data assimilation
1361 schemes, and use of large ensemble simulations with high numbers of individual model simulations for
1362 better representation of model statistics.

1363 *Non-hydrostatic and Boussinesq assumption*

1364 The possible higher spatial resolution will in many coastal ocean scenarios allow for resolving non-
1365 hydrostatic processes. In cases where the horizontal resolution becomes substantially smaller than the
1366 water depth, hydrostatic models would lose their predictability when for example relatively short internal
1367 waves still propagate at their hydrostatic phase speed. Therefore, one challenge to the developers of coastal
1368 ocean models is to allow for efficient non-hydrostatic pressure calculation in situations where needed.
1369 As discussed in section 8.2, there are only a few of such examples among the structured-grid models.
1370 The challenge would therefore be that models automatically analyse whether in some regions the non-
1371 hydrostatic pressure contribution is relevant, and if so, the non-hydrostatic dynamics should be applied.
1372 On other (e.g., shallower) parts of the model domain it might be ignored. It should however be kept in
1373 mind that diagnosed non-hydrostatic pressure might also be a numerical artefact (Vitousek and Fringer,
1374 2011).

1375 Another possibility to consistently add non-hydrostatic effects, while avoiding the costly direct solution
1376 of a 3D Poisson equation for the pressure, is to relax both the hydrostatic and Boussinesq assumptions (Au-
1377 clair et al., 2016). Since relaxing the Boussinesq assumption reintroduces the acoustic waves, an acoustic
1378 mode must be considered on top of the internal and external modes. This three-mode approach has the
1379 advantage to be completely explicit (i.e. local in space) and thus to have very good properties in terms
1380 of scalability. However, it raises new challenges to derive consistent open boundary conditions to couple
1381 models based on different modeling assumptions.

1382 *Physics-dynamics coupling*

1383 The development of numerical models generally dissociates the dynamical kernel, which handles the
1384 resolved scales, from the "physics", that account for under-resolved processes. However, both components
1385 are strongly coupled since there is constantly a transfer of information back and forth from the dynamics to
1386 the physics so that the dynamical core must not violate physical principles. Energy-consistency is certainly

1387 one important example of such coupling. As discussed in section 7.1, most advection schemes are not
1388 variance conserving, which means for the momentum budget violation of kinetic energy conservation. The
1389 rate of numerical dissipation can be diagnosed (e.g. Klingbeil et al., 2014) and it can be shown that more
1390 complex advection schemes limit the numerical dissipation (Mohammadi-Aragh et al., 2015). Another
1391 source of energy-conservation violation is due to the exchange between mean kinetic energy and potential
1392 energy. This exchange is represented by the pressure-gradient term in the momentum equations and the
1393 advection terms of the temperature and salinity equations. Since those terms are discretised completely
1394 independently, energy-consistency is not given. Another issue is the energy consistency between loss of
1395 mean kinetic energy due to vertical stress divergence and production of turbulent kinetic energy (see
1396 section 7.7 and Burchard, 2002b). Generally better energy-consistency may also be achieved by more
1397 suitable choices for vertical coordinates. As discussed in section 4.2, generalised vertical coordinates give
1398 a high degree of freedom to construct an optimised vertical grid layout. This flexibility needs to be better
1399 exploited in the future to improve the performance of coastal ocean models.

1400 It should be briefly mentioned that also the physics of coastal ocean models (as well as for large scale
1401 ocean models) is generally not energy-consistent, since e.g. the energy lost by horizontal stress divergence
1402 is not reintroduced into any other energy compartment of the model. This is an important issue which
1403 could however not be further discussed in this numerical review (see e.g., the discussion by Eden et al.,
1404 2014).

1405 *Multi-resolution strategies*

1406 One other aspect of ongoing discussions in the coastal ocean developers community is the optimal
1407 layout for horizontal grids. In both, structured-grid and unstructured-grid models, substantial progress
1408 has been made in the past. While unstructured-grid models have the better ability to solve multi-scale
1409 problems, the numerical cost per nominal grid point is generally much larger than for structured-grid
1410 models. It does therefore depend on the kind of problem to decide which type of model is better suited.
1411 For complex domains such as lagoon systems or estuarine networks, unstructured-grid models are the
1412 better choice while for classical coastal or shelf sea scenarios structured-grid models are more efficient.
1413 Structured-grid models have gained flexibility due to more flexible grids (such as curvilinear grids, see
1414 section 4 or two-way nesting, see section 6.3). Flexible multi-level nesting strategies reducing the number
1415 of masked grid points (land points) in the model domain might in the future help to better tackle multi-
1416 scale problems using structured grids. And there are efforts to increase the efficiency of unstructured-grid
1417 models. Both types of models - structured-grid models with flexible nesting and unstructured-grid models -
1418 might in the future support horizontal mesh-adaptivity to resolve moving or intermittent dynamic features
1419 (as for example done in larger scale models to follow hurricanes). It depends on the success of such
1420 developments which type of model is gaining more ground in the future of coastal ocean modelling.

1421 *Coupling with other earth system compartments*

1422 Finally, stand-alone hydrodynamic coastal ocean models will always have a limited area of application.
1423 All such models are developed to also function as hydrodynamic core of coupled model systems. Most
1424 common is the coupling to biogeochemical models, where the hydrodynamic model provides advective
1425 and turbulent transports as well as the light regime and many other potential functional links between
1426 hydrodynamics and biogeochemistry. Without accurate physical and numerical representation of the hy-

1427 drodynamics (e.g., in terms of the mixed-layer depth), biogeochemical models will have no predictability.
1428 Links between hydrodynamics and biogeochemistry may be complex. One tool to flexibly provide such a
1429 link is FABM (Framework of Biogeochemical Models, Bruggeman and Bolding (2014)).

1430 Coupling to several other Earth system compartments is common, such as to statistical surface wave
1431 models, sea ice models, atmospheric models, benthic models, and hydrological models. Several compre-
1432 hensive system models exist, such as COAWST (Warner et al., 2008), interactively coupling hydrodynam-
1433 ics (from ROMS) with surfaces waves, atmosphere, biogeochemistry, sediment transport and benthos to
1434 study complex coastal ocean scenarios in hindcast and sensitivity mode, or NEMO-Nordic (Gröger et al.,
1435 2015), coupling hydrodynamics (from NEMO) with atmosphere, sea ice, biogeochemistry, and hydrology
1436 for the purpose of regional climate downscaling and sensitivity scenarios. It is obvious that all coupling
1437 interfaces to other compartments require hydrodynamic process adaptations on the side of the hydrody-
1438 namic module, and that those need to be numerically discretised with care. It is expected that in the future,
1439 such complex coupled model systems will be much more widely used, such that quite some pressure to
1440 further develop hydrodynamic model will be generated.

1441 Despite the substantial growth of computational resources, regional climate system models with run-
1442 times of typically more than a century and which maybe executed as large ensemble runs with many
1443 individual simulations will require high accuracy at relatively low resolution. Therefore the development
1444 of efficient and accurate numerical schemes at low resolution will be an important task also for the future.

1445 **Acknowledgements:** This paper is a contribution to the project M5 (Reducing spurious diapycnal
1446 mixing in ocean models) of the Collaborative Research Centre TRR 181 on Energy Transfer in Atmosphere
1447 and Ocean funded by the German Research Foundation. Further support has been granted by the project
1448 MOSSCO (Modular System for Shelves and Coasts) funded by the German Federal Ministry of Research
1449 and Education (BMBF) under the project identification number FKZ 03F0667B. F. Lemarié and L. Debreu
1450 acknowledge the support of the french national research agency (ANR) through contracts ANR-14-CE23-
1451 0010 (HEAT) and ANR-16-CE01-0007 (COCOA). We are grateful to Robert Hallberg (Princeton) for
1452 discussing principles of turbulence closure schemes for global ocean models with us. Furthermore, we
1453 would like to thank Martin Schmidt (Warnemünde) for many helpful discussions. Finally, we appreciate
1454 the very constructive comments from Sergey Danilov and three anonymous reviewers.

1455 A Set of layer-integrated equations

1456 The layer-integrated continuity equation (3.1) reads:

$$1457 \quad \partial_t h_k + \partial_x (h_k u_k) + \partial_y (h_k v_k) + (w_{k+1/2}^s - w_{k-1/2}^s) = 0, \quad (\text{A.1})$$

1458 The layer-integrated momentum equations (3.3) and (3.4) are:

$$\begin{aligned}
& \partial_t (h_k u_k) + \partial_x (h_k u_k u_k) + \partial_y (h_k v_k u_k) + \left(w_{k+1/2}^s \tilde{u}_{k+1/2} - w_{k-1/2}^s \tilde{u}_{k-1/2} \right) \\
& = h_k \tilde{F}_x^h(h_k, u_k, v_k) + \left(\tau_{x,k+1/2} - \tau_{x,k-1/2} \right)
\end{aligned} \tag{A.2}$$

1459

$$+ f h_k v_k - h_k \frac{1}{\rho_0} \partial_x p_a - g h_k \partial_x \eta + h_k F_{x,k}^{\text{IPG}},$$

1460

$$\partial_t (h_k v_k) + \partial_x (h_k u_k v_k) + \partial_y (h_k v_k v_k) + \left(w_{k+1/2}^s \tilde{v}_{k+1/2} - w_{k-1/2}^s \tilde{v}_{k-1/2} \right)$$

1461

$$= h_k \tilde{F}_y^h(h_k, u_k, v_k) + \left(\tau_{y,k+1/2} - \tau_{y,k-1/2} \right) \tag{A.3}$$

$$- f h_k u_k - h_k \frac{1}{\rho_0} \partial_y p_a - g h_k \partial_y \eta + h_k F_{y,k}^{\text{IPG}},$$

1462

with $\tilde{F}_{[x,y]}^h$, $\tau_{[x,y],k+1/2}$ and $F_{[x,y],k}^{\text{IPG}}$ defined in (4.4), (4.3) and (4.5).

1463

The layer-integrated temperature equation (3.10) is:

$$\begin{aligned}
& \partial_t (h_k \Theta_k) + \partial_x (h_k u_k \Theta_k) + \partial_y (h_k v_k \Theta_k) + \left(w_{k+1/2}^s \tilde{\Theta}_{k+1/2} - w_{k-1/2}^s \tilde{\Theta}_{k-1/2} \right) \\
& = -\partial_x \left(h_k J_{x,k}^\Theta \right) - \partial_y \left(h_k J_{y,k}^\Theta \right) - \left(J_{z,k+1/2}^\Theta - J_{z,k-1/2}^\Theta \right) \\
& \quad + \frac{1}{C_p \rho_0} \left(I_{k+1/2} - I_{k-1/2} \right).
\end{aligned} \tag{A.4}$$

1464

1465

The layer-integrated salinity equation (3.12) is:

$$\begin{aligned}
& \partial_t (h_k S_k) + \partial_x (h_k u_k S_k) + \partial_y (h_k v_k S_k) + \left(w_{k+1/2}^s \tilde{S}_{k+1/2} - w_{k-1/2}^s \tilde{S}_{k-1/2} \right) \\
& = -\partial_x \left(h_k J_{x,k}^S \right) - \partial_y \left(h_k J_{y,k}^S \right) - \left(J_{z,k+1/2}^S - J_{z,k-1/2}^S \right).
\end{aligned} \tag{A.5}$$

1466

1467 **References**

1468 **References**

- 1469 Adcroft, A., Hallberg, R., Harrison, M., 2008. A finite volume discretization of the pressure gradient force
1470 using analytic integration. *Ocean Modell.* 22, 106–113.
- 1471 Adcroft, A., Hill, C., Marshall, J., 1997. Representation of topography by shaved cells in a height coordi-
1472 nate ocean model. *Mon. Wea. Rev.* 125, 2293–2315.
- 1473 Adcroft, A.J., Campin, J.M., 2004. Rescaled height coordinates for accurate representation of free-surface
1474 flows in ocean circulation models. *Ocean Modell.* 7, 269–284.
- 1475 Adcroft, A.J., Hallberg, R.W., 2006. On methods for solving the oceanic equations of motion in general-
1476 ized vertical coordinates. *Ocean Modell.* 11, 224–233.
- 1477 Arakawa, A., Lamb, V.R., 1977. Computational design of the basic dynamical processes of the UCLA
1478 General Circulation Model. *Meth. Comput. Phys.* 17, 174–267.
- 1479 Auclair, F., Bordois, L., Dossmann, Y., Duhaut, T., Paci, A., Ulses, C., Nguyen, C., 2016. A non-
1480 hydrostatic non-Boussinesq algorithm for free-surface ocean modelling. *Ocean Modell.* In revision.
- 1481 Auclair, F., Estournel, C., Floor, J.W., Herrmann, M.J., Nguyen, C., Marsaleix, P., 2011. A non-hydrostatic
1482 algorithm for free-surface ocean modelling. *Ocean Modelling* 36, 49–70.
- 1483 BACC II Author Team, 2015. Second assessment of climate change for the Baltic Sea basin. Springer.
- 1484 Backhaus, J.O., 1976. Zur Hydrodynamik im Flachwassergebiet. Ein numerisches modell. *Dt. Hydrogr.*
1485 *Z.* 29, 222–238.
- 1486 Backhaus, J.O., 1985. A three-dimensional model for the simulation of shelf sea dynamics. *Dt. Hydrogr.*
1487 *Z.* 38, 165–187.
- 1488 Barnier, B., Marchesiello, P., Miranda, A.P.D., Molines, J.M., Coulibaly, M., 1998. A sigma-coordinate
1489 primitive equation model for studying the circulation in the south atlantic. part i: Model configuration
1490 with error estimates. *Deep-Sea Res.* 45, 543–572.
- 1491 Beckers, J.M., Burchard, H., Campin, J.M., Deleersnijder, E., Mathieu, P.P., 1998. Another reason why
1492 simple discretizations of rotated diffusion operators cause problems in ocean models. Comments on
1493 the paper *isoneutral diffusion in a z-coordinate ocean model* by Griffies et al. *J. Phys. Oceanogr.* 28,
1494 1552–1559.
- 1495 Beckers, J.M., Burchard, H., Deleersnijder, E., Mathieu, P.P., 2000. On the numerical discretization of
1496 rotated diffusion operators in ocean models. *Mon. Wea. Rev.* 128, 2711–2733.
- 1497 Beckers, J.M., Deleersnijder, E., 1993. Stability of a FBTCS scheme applied to the propagation of shallow-
1498 water inertia-gravity waves on various space grids. *J. Comp. Phys.* 108, 95–104.
- 1499 Beckmann, A., Döscher, R., 1997. A method for improved representation of dense water spreading over
1500 topography in geopotential-coordinate models. *J. Phys. Oceanogr.* 27, 581–591.
- 1501 Berntsen, J., 2011. A perfectly balanced method for estimating the internal pressure gradients in σ -
1502 coordinate ocean models. *Ocean Modell.* 38, 85–95.
- 1503 Berntsen, J., Furnes, G., 2005. Internal pressure errors in sigma-coordinate ocean models – sensitivity of
1504 the growth of the flow to the time stepping method and possible non-hydrostatic effects. *Continental*
1505 *Shelf Research* 25, 829–848.
- 1506 Beron-Vera, F., Ochoa, J., Ripa, P., 1999. A note on boundary conditions for salt and freshwater balances.
1507 *Ocean Modell.* 1, 111–118.
- 1508 Blaas, M., Dong, C., Marchesiello, P., McWilliams, J.C., Stolzenbach, K.D., 2007. Sediment-transport
1509 modeling on southern californian shelves: A roms case study. *Cont. Shelf Res.* 27, 832–853.

- 1510 Blayo, E., 2000. Compact finite difference schemes for ocean models: 1. ocean waves. *J. Comp. Phys.*
1511 164, 241–257.
- 1512 Blayo, E., Debreu, L., 2005. Revisiting open boundary conditions from the point of view of characteristic
1513 variables. *Ocean Modell.* 9, 231–252.
- 1514 Bleck, R., 2002. An oceanic general circulation model framed in hybrid isopycnic-Cartesian coordinates.
1515 *Ocean Modell.* 4, 55–88.
- 1516 Bleck, R., Smith, L.T., 1990. A wind-driven isopycnic coordinate model of the north and equatorial atlantic
1517 ocean: 1. model development and supporting experiments. *J. Geophys. Res.* 95, 3273–3285.
- 1518 Blumberg, A.F., 1992. A Primer for ECOM-si. Technical Report. HydroQual, Inc.
- 1519 Blumberg, A.F., Mellor, G.L., 1978. A coastal ocean numerical model, in: Sündermann, J., Holz, K.P.
1520 (Eds.), *Mathematical Modelling of Estuarine Physics*. Springer-Verlag, New York, pp. 203–214.
- 1521 Blumberg, A.F., Mellor, G.L., 1987. A description of a coastal ocean circulation model, in: Heaps, N.S.
1522 (Ed.), *Three dimensional ocean models*. American Geophysical Union, Washington, D.C., pp. 1–16.
- 1523 Bolding, K., Burchard, H., Pohlmann, T., Stips, A., 2002. Turbulent mixing in the Northern North Sea: a
1524 numerical model study. *Cont. Shelf Res.* 22, 2707–2724.
- 1525 Bott, A., 2010. Improving the time-splitting errors of one-dimensional advection schemes in multidimen-
1526 sional applications. *Atmos. Res.* 97, 619–631.
- 1527 Botta, N., Klein, R., Langenberg, S., Lützenkirchen, S., 2004. Well balanced finite volume methods for
1528 nearly hydrostatic flows. *J. Comp. Phys.* 196, 539–565.
- 1529 Brown, J.A., Campana, K.A., 1978. An economical time-differencing system for numerical weather pre-
1530 diction. *Mon. Wea. Rev.* 106, 1125–1136.
- 1531 Bruggeman, J., Bolding, K., 2014. A general framework for aquatic biogeochemical models. *Environ-*
1532 *mental Modelling & Software* 61, 249–265.
- 1533 Burchard, H., 2001. Simulating the wave-enhanced layer under breaking surface waves with two-equation
1534 turbulence models. *J. Phys. Oceanogr.* 31, 3133–3145.
- 1535 Burchard, H., 2002a. Applied turbulence modelling in marine waters. volume 100 of *Lecture Notes in*
1536 *Earth Sciences*. Springer, Berlin, Heidelberg, New York.
- 1537 Burchard, H., 2002b. Energy-conserving discretisation of turbulent shear and buoyancy production. *Ocean*
1538 *Modell.* 4, 347–361.
- 1539 Burchard, H., Badewien, T.H., 2015. Thermohaline residual circulation of the Wadden Sea. *Ocean Dyn.*
1540 65, 1717–1730.
- 1541 Burchard, H., Baumert, H., 1995. On the performance of a mixed-layer model based on the k - ϵ turbulence
1542 closure. *J. Geophys. Res.* 100, 8523–8540.
- 1543 Burchard, H., Baumert, H., 1998. The formation of estuarine turbidity maxima due to density effects in
1544 the salt wedge. A hydrodynamic process study. *J. Phys. Oceanogr.* 28, 309–321.
- 1545 Burchard, H., Beckers, J.M., 2004. Non-uniform adaptive vertical grids in one-dimensional numerical
1546 ocean models. *Ocean Modell.* 6, 51–81.
- 1547 Burchard, H., Bolding, K., 2002. GETM – a general estuarine transport model. Scientific Documentation.
1548 Technical Report. European Commission.
- 1549 Burchard, H., Bolding, K., Villarreal, M.R., 2004. Three-dimensional modelling of estuarine turbidity
1550 maxima in a tidal estuary. *Ocean Dyn.* 54, 250–265.
- 1551 Burchard, H., Craig, P.D., Gemrich, J.R., van Haren, H., Mathieu, P.P., Meier, H.E.M., Nimmo Smith,
1552 W.A.M., Prandke, H., Rippeth, T.P., Skillingstad, E.D., Smyth, W.D., Welsh, D.J.S., Wijesekera, H.W.,
1553 2008. Observational and numerical modelling methods for quantifying coastal ocean turbulence and
1554 mixing. *Progr. Oceanogr.* 76, 399–442.

- 1555 Burchard, H., Deleersnijder, E., Stoyan, G., 2005. Some numerical aspects of turbulence-closure models,
1556 in: Baumert, H.Z., Simpson, J.H., Sündermann, J. (Eds.), *Marine Turbulence: Theories, Observations
1557 and Models*. Cambridge University Press, Cambridge, Cambridge, pp. 197–206.
- 1558 Burchard, H., Petersen, O., 1997. Hybridization between σ - and z -coordinates for improving the internal
1559 pressure gradient calculation in marine models with steep bottom slopes. *Int. J. Numer. Meth. Fl.* 25,
1560 1003–1023.
- 1561 Burchard, H., Petersen, O., 1999. Models of turbulence in the marine environment – A comparative study
1562 of two-equation turbulence models. *J. Mar. Syst.* 21, 29–53.
- 1563 Burchard, H., Petersen, O., Rippeth, T.P., 1998. Comparing the performance of the Mellor-Yamada and
1564 the k - ϵ two-equation turbulence models. *J. Geophys. Res.* 103, 10543–10554.
- 1565 Burchard, H., Rennau, H., 2008. Comparative quantification of physically and numerically induced mixing
1566 in ocean models. *Ocean Modell.* 20, 293–311.
- 1567 Capet, X., Campos, E.J., Paiva, A.M., 2008. Submesoscale activity over the Argentinian shelf. *Geophys.*
1568 *Res. Lett.* 35, 10.1029/2008GL034736.
- 1569 Carpenter, J.R., Merckelbach, L., Callies, U., Clark, S., Gaslikova, L., Baschek, B., 2016. Potential impacts
1570 of offshore wind farms on North Sea stratification. *PloS one* 11(8), e0160830.
- 1571 Casulli, V., Cattani, E., 1994. Stability, accuracy and efficiency of a semi-implicit method for three-
1572 dimensional shallow water flow. *Computers Math. Appl.* 27, 99–112.
- 1573 Casulli, V., Cheng, R.T., 1992. Semi-implicit finite difference methods for three-dimensional shallow
1574 water flow. *Int. J. Numer. Meth. Fluids* 15, 629–648.
- 1575 Cheng, R.T., Casulli, V., Gartner, J.W., 1993. Tidal, Residual, Intertidal Mudflat (TRIM) model and its
1576 applications to San Francisco Bay, California. *Estuar., Coast. Shelf S.* 36, 235–280.
- 1577 Chorin, A.J., 1968. Numerical Solution of the Navier-Stokes Equations. *Mathematics of Computation* 22,
1578 745–762.
- 1579 Conley, D.J., Paerl, H.W., Howarth, R.W., Boesch, D.F., Seitzinger, S.P., Havens, K.E., Lancelot, C.,
1580 Likens, G.E., 2009. Controlling eutrophication: nitrogen and phosphorus. *Science* 323(5917), 1014–
1581 1015.
- 1582 Craig, P.D., 1989. A model for diurnally forced vertical current structure near 30° latitude. *Cont. Shelf*
1583 *Res.* 9, 965–980.
- 1584 Cushman-Roisin, B., Beckers, J.M., 2011. Introduction to geophysical fluid dynamics: physical and nu-
1585 merical aspects. volume 101. Academic Press.
- 1586 Danabasoglu, G., Yeager, S.G., Bailey, D., Behrens, E., Bentsen, M., Bi, D., Biastoch, A., Böning, C.,
1587 Bozec, A., Canuto, V.M., et al., 2014. North Atlantic simulations in coordinated ocean-ice reference
1588 experiments phase II (CORE-II). Part I: mean states. *Ocean Modell.* 73, 76–107.
- 1589 Daru, V., Tenaud, C., 2004. High order one-step monotonicity-preserving schemes for unsteady compress-
1590 ible flow calculations. *J. Comp. Phys.* 193, 563–594.
- 1591 Davies, H.C., 1976. A lateral boundary formulation for multi-level prediction models. *Q. J. R. Meteorolog.*
1592 *S.* 102, 405–418.
- 1593 Debreu, L., Blayo, E., 2008. Two-way embedding algorithms: a review. *Ocean Dyn.* 58, 415–428.
- 1594 Defne, Z., Ganju, N.K., 2015. Quantifying the residence time and flushing characteristics of a shallow,
1595 back-barrier estuary: application of hydrodynamic and particle tracking models. *Estuaries and Coasts*
1596 38, 1719–1734.
- 1597 Deleersnijder, E., 1993. Numerical mass conservation in a free-surface sigma coordinate marine model
1598 with mode splitting. *Journal of Marine Systems* 4, 365–370.
- 1599 Deleersnijder, E., Beckers, J.M., 1992. On the use of the σ -coordinate system in regions of large bathy-

metric variations. *J. Mar. Syst.* 3, 381–390.

1601 Deleersnijder, E., Beckers, J.M., Campin, J.M., El Mohajir, M., Fichefet, T., Luyten, P., 1997. Some
1602 mathematical problems associated with the development and use of marine models, in: Diaz, J.I. (Ed.),
1603 The mathematics of models for climatology and environment. Springer, Berlin, Heidelberg. volume 48
1604 of *NATO ASI Series*, pp. 41–86.

1605 Delhez, E.J.M., Grégoire, M., Nihoul, J.C.J., Beckers, J.M., 1999. Dissection of the GHER turbulence
1606 closure scheme. *J. Mar. Syst.* 21, 379–397.

1607 Demange, J., Debreu, L., Marchesiello, P., Lemarié, F., Blayo, E., 2014. Numerical representation of
1608 internal waves propagation. Research report. INRIA. Available online at [http://hal.inria.fr/
1609 hal-01063417/PDF/RR-8590.pdf](http://hal.inria.fr/hal-01063417/PDF/RR-8590.pdf).

1610 Diaz, R.J., Rosenberg, R., 2008. Spreading dead zones and consequences for marine ecosystems. *science*
1611 321, 926–929.

1612 Dukhovskoy, D.S., Moreay, S.L., Martin, P.J., O’Brien, James J. Cooper, C., 2009. Application of a
1613 vanishing, quasi-sigma, vertical coordinate for simulation of high-speed, deep currents over the Sigsbee
1614 Escarpment in the Gulf of Mexico. *Ocean Modelling* 28, 250–265.

1615 Dukowicz, J.K., 2001. Reduction of density and pressure gradient errors in ocean simulations. *J. Phys.*
1616 *Oceanogr.* 31, 1915–1921.

1617 Durran, D.R., 2010. *Numerical Methods for Fluid Dynamics With Applications to Geophysics*. Springer.
1618 2nd edition.

1619 Durski, S.M., Glenn, S.M., Haidvogel, D.B., 2004. Vertical mixing schemes in the coastal ocean: Compar-
1620 ison of the level 2.5 Mellor-Yamada scheme with an enhanced version of the K profile parameterisation.
1621 *J. Geophys. Res.* 109, C01015, doi:10.1029/2002JC001702.

1622 Eden, C., Czeschel, L., Olbers, D., 2014. Toward energetically consistent ocean models. *J. Phys. Oceanogr.*
1623 44, 3160–3184.

1624 Eden, C., Greatbatch, R.J., 2008. Towards a mesoscale eddy closure. *Ocean Modell.* 20, 223–239.

1625 Espelid, T.O., Berntsen, J., Barthel, K., 2000. Conservation of energy for schemes applied to the propaga-
1626 tion of shallow-water inertia-gravity waves in regions with varying depth. *Int. J. for Numer. Meth. Eng.*
1627 49, 1521–1545.

1628 Ezer, T., Mellor, G.L., 2004. A generalised coordinate ocean model and a comparison of the bottom
1629 boundary layer dynamics in terrain-following and in z -level grids. *Ocean Modell.* 6, 379–403.

1630 Fairall, C.W., Bradley, E.F., Rogers, D.P., Edson, J.B., Young, G.S., 1996. Bulk parameterization of air-sea
1631 fluxes for Tropical Ocean-Global Atmosphere Coupled-Ocean Atmosphere Response Experiment. *J.*
1632 *Geophys. Res.* 101, 3747–3764.

1633 Feagin, R.A., Sherman, D.J., Grant, W.E., 2005. Coastal erosion, global sea-level rise, and the loss of sand
1634 dune plant habitats. *Frontiers in Ecology and the Environment* 3, 359–364.

1635 Fennel, W., Seifert, T., Kayser, B., 1991. Rossby radii and phase speeds in the Baltic Sea. *Cont. Shelf*
1636 *Res.* 11, 23–36.

1637 Flather, R., 1976. A tidal model of the north-west european continental shelf. *Memoires de la Societe*
1638 *Royale des Sciences de Liege* 6, 141–164.

1639 Flather, R.A., Heaps, N.S., 1975. Tidal computations for Morecambe Bay. *Geophys. J. Roy. Astron. Soc.*
1640 42, 489–517.

1641 Fox-Kemper, B., Danabasoglu, G., Ferrari, R., Griffies, S., Hallberg, R., Holland, M., Maltrud, M., Pea-
1642 cock, S., Samuels, B., 2011. Parameterization of mixed layer eddies. iii: Implementation and impact in
1643 global ocean climate simulations. *Ocean Modelling* 39(1), 61–78.

1644 Gao, X., Chen, C.T.A., 2012. Heavy metal pollution status in surface sediments of the coastal Bohai Bay.

1645 Water Research 46, 1901–1911.

1646 Gaspar, P., Gregoris, Y., Lefevre, J., 1990. A simple eddy kinetic energy model for simulations of the
1647 oceanic vertical mixing: Tests at station Papa and long-term upper ocean study site. *J. Geophys. Res.*
1648 95, 16179–16193.

1649 Gent, P.R., McWilliams, J.C., 1990. Isopycnal mixing in ocean circulation models. *J. Phys. Oceanogr.* 20,
1650 150–155.

1651 Gerdes, R., 1993. A primitive equation ocean circulation model using a general vertical coordinate trans-
1652 formation. 1. Description and testing of the model. *J. Geophys. Res.* 98, 14683–14701.

1653 Gerritsen, H., De Goede, E., Genseberger, M., Uittenbogaard, R., 2004. Validation Document Delft3D-
1654 FLOW. Technical Report. WL Delft Hydraulics.

1655 Gottlieb, S., Shu, C.W., 1998. Total variation diminishing runge-kutta schemes. *Math. Comput.* 67, 73–85.

1656 Gräwe, U., Flöser, G., Gerkema, T., Duran-Matute, M., Badewien, T., Schulz, E., Burchard, H., 2016.
1657 A numerical model for the entire Wadden Sea: skill assessment and analysis of hydrodynamics. *J.*
1658 *Geophys. Res.* 121, 5231–5251.

1659 Gräwe, U., Holtermann, P., Klingbeil, K., Burchard, H., 2015. Advantages of vertically adaptive coordi-
1660 nates in numerical models of stratified shelf seas. *Ocean Modell.* 92, 56–68.

1661 Griffies, S., Adcroft, A., 2008. Formulating the equations of ocean models, in: Hecht, M., Hasumi, H.
1662 (Eds.), *Ocean Modeling in an Eddying Regime*. American Geophysical Union, Washington, D.C.. vol-
1663 ume 177 of *Geophysical Monograph Series*, pp. 281–317.

1664 Griffies, S.M., 2004. *Fundamentals of ocean climate models*. volume 518. Princeton University Press.

1665 Griffies, S.M., 2007. Elements of mom4p1. Technical Report. NOAA/GFDL. Version prepared on
1666 September 27, 2007.

1667 Griffies, S.M., Boning, C., Bryan, F.O., Chassignet, E.P., Gerdes, R., Hasumi, H., Hirst, A., Treguier, A.M.,
1668 Webb, D., 2000. Developments in ocean climate modelling. *Ocean Modell.* 2, 123–192.

1669 Griffies, S.M., Gnanadesikan, A., Pacanowski, R.C., Larichev, V.D., Dukowicz, J.K., Smith, R.D., 1998.
1670 Isoneutral diffusion in a z -coordinate ocean model. *J. Phys. Oceanogr.* 28, 805–830.

1671 Gröger, M., Dieterich, C., Meier, M.H., Schimanke, S., 2015. Thermal air-sea coupling in hindcast simu-
1672 lations for the North Sea and Baltic Sea on the NW European shelf. *Tellus A* 67.

1673 Haidvogel, D.B., Arango, H.G., Hedstrom, K., Beckmann, A., Malanotte-Rizzoli, P., Shchepetkin, A.F.,
1674 2000. Model evaluation experiments in the north atlantic basin: simulations in nonlinear terrain-
1675 following coordinates. *Dynam. Atmos. Ocean* 32, 239–281.

1676 Halpern, B.S., Walbridge, S., Selkoe, K.A., Kappel, C.V., Micheli, F., D’agrosa, C., Bruno, J.F., Casey,
1677 K.S., Ebert, C., Fox, H.E., Fujita, R., Heinemann, D., Lenihan, H.S., Madin, E.M.P., Perry, M.T., Selig,
1678 E.R., Spalding, M., Steneck, R., Watson, R., 2008. A global map of human impact on marine ecosys-
1679 tems. *Science* 319(5865), 948–952.

1680 Haney, R.L., 1991. On the pressure gradient force over steep topography in sigma coordinate ocean models.
1681 *J. Phys. Oceanogr.* 21, 610–619.

1682 Harcourt, R.R., 2014. A second-moment closure model of Langmuir Turbulence. *J. Phys. Oceanogr.* 43,
1683 673–697.

1684 van Haren, H., Maas, L., Zimmerman, J.T.F., Malschaert, H.R.H., 1999. Strong inertial currents and
1685 marginal internal wave stability in the central North Sea. *Geophys. Res. Lett.* 26, 2993–2996.

1686 Harten, A., 1983. High resolution schemes for hyperbolic conservation laws. *J. Comput. Phys.* 49, 357–
1687 393.

1688 Heggelund, Y., Vikebø, F., Berntsen, J., Furnes, G., 2004. Hydrostatic and non-hydrostatic studies of
1689 gravitational adjustment over a slope. *Continental Shelf Research* 24, 2133–2148.

- 1690 Hirt, C.W., Amsden, A.A., Cook, J.L., 1974. An Arbitrary Lagrangian-Eulerian Computing Method for
1691 All Flow Speeds. *J. Comput. Phys.* 14, 227–253.
- 1692 Hofmeister, R., Bolding, K., Hetland, R.D., Schernewski, G., Siegel, H., Burchard, H., 2013. The dynam-
1693 ics of cooling water discharge in a shallow, non-tidal embayment. *Cont. Shelf Res.* 71, 68–77.
- 1694 Hofmeister, R., Burchard, H., Beckers, J.M., 2010. Non-uniform adaptive vertical grids for 3d numerical
1695 ocean models. *Ocean Modell.* 33, 70–86.
- 1696 Holt, J., Harle, J., Proctor, R., Michel, S., Ashworth, M., Batstone, C., Allen, I., Holmes, R., Smyth,
1697 T., Haines, K., Bretherton, D., Smith, G., 2009. Modelling the global coastal ocean. *Philosophical
1698 Transactions of the Royal Society of London A: Mathematical, Physical and Engineering Sciences* 367,
1699 939–951.
- 1700 Holt, J.T., James, I.D., 2001. An s coordinate density evolving model of the northwest european continental
1701 shelf: 1. model description and density structure. *J. Geophys. Res.* 106, 14015–14034.
- 1702 Holt, J.T., James, I.D., 2006. An assessment of the fine-scale eddies in a high-resolution model of the shelf
1703 seas west of Great Britain. *Ocean Modell.* 13, 271–291.
- 1704 Horner-Devine, A.R., Hetland, R.D., MacDonald, D.G., 2015. Mixing and transport in coastal river
1705 plumes. *Annu. Rev. Fluid Mech.* 47, 569–594.
- 1706 Hundsdorfer, W., Trompert, R.A., 1994. Method of lines and direct discretization: A comparison for linear
1707 advection. *Appl. Numer. Math.* 13, 469–490.
- 1708 Huthnance, J.M., 1995. Circulation, exchange and water masses at the ocean margin: the role of physical
1709 processes at the shelf edge. *Progr. Oceanogr.* 35, 353–431.
- 1710 Ilicak, M., Adcroft, A.J., Griffies, S.M., Hallberg, R.W., 2012. Spurious diapycnal mixing and the role of
1711 momentum closure. *Ocean Modell.* 45–46, 37–58.
- 1712 Jackson, J.B.C., Kirby, M.X., Berger, W.H., Bjorndal, K.A., Botsford, L.W., Bourque, B.J., Bradbury,
1713 R.H., Cooke, R., Erlandson, J., Estes, J.A., Hughes, T.P., Kidwell, S., Lange, C.B., Lenihan, H.S., Pan-
1714 dolfi, J.M., Peterson, C.H., Steneck, R.S., Tegner, M.J., Warner, R.R., 2001. Historical overfishing and
1715 the recent collapse of coastal ecosystems. *science* 293(5530), 629–637.
- 1716 Jackson, L., Hallberg, R., Legg, S., 2008. A parameterization of shear-driven turbulence for ocean climate
1717 models. *J. Phys. Oceanogr.* 38, 1033–1053.
- 1718 James, I., 2000. A high-performance explicit vertical advection scheme for ocean models: how {PPM}
1719 can beat the {CFL} condition. *Appl. Math. Model.* 24(1), 1 – 9.
- 1720 Jay, D.A., Musiak, J.D., 1994. Particle trapping in estuarine tidal flows. *J. Geophys. Res.* 99, 20445–
1721 20461.
- 1722 Jensen, T.G., 1998. Open boundary conditions in stratified ocean models. *J. Mar. S.* 16, 297–322.
- 1723 Johns, B., Marsaleix, P., Estournel, C., Vhil, R., 1992. On the wind-driven coastal upwelling in the gulf of
1724 lions. *J. Mar. S.* 3, 309–320.
- 1725 Jungclaus, J.H., Backhaus, J.O., 1994. Application of a transient reduced gravity plume model to the
1726 denmark strait overflow. *J. Geophys. Res.* 99, 12375–12396.
- 1727 Kållberg, P., 1977. Test of a lateral boundary relaxation scheme in a barotropic model. Internal Report.
1728 ECMWF Research Department.
- 1729 van Kan, J., 1986. A second-order accurate pressure correction scheme for viscous incompressible flow.
1730 *Journal of Science and Statistical Computation* 7, 870–891.
- 1731 Kanarska, Y., Maderich, V., 2003. A non-hydrostatic numerical model for calculating free-surface strati-
1732 fied flows. *Ocean Dynamics* 53, 176–185.
- 1733 Kanarska, Y., Shchepetkin, A., McWilliams, J., 2007. Algorithm for non-hydrostatic dynamics in the
1734 Regional Oceanic Modeling System. *Ocean Modell.* 18, 143–174.

- 1735 Kantha, L.H., Clayson, C.A., 2000a. Numerical models of oceans and oceanic processes. volume 66 of
1736 *International Geophysics Series*. Academic Press.
- 1737 Kantha, L.H., Clayson, C.A., 2000b. Small-scale processes in geophysical fluid flows. volume 67 of
1738 *International Geophysics Series*. Academic Press.
- 1739 Kasahara, A., 1974. Various Vertical Coordinate Systems Used For Numerical Weather Prediction. *Mon.*
1740 *Wea. Rev.* 102, 509–522.
- 1741 Keilegavlen, E., Berntsen, J., 2009. Non-hydrostatic pressure in σ -coordinate ocean models. *Ocean Mod-*
1742 *elling* 28, 240–249.
- 1743 Klingbeil, K., Burchard, H., 2013. Implementation of a direct nonhydrostatic pressure gradient discretisa-
1744 tion into a layered ocean model. *Ocean Modell.* 65, 64–77.
- 1745 Klingbeil, K., Mohammadi-Aragh, M., Gräwe, U., Burchard, H., 2014. Quantification of spurious dissi-
1746 pation and mixing - discrete variance decay in a finite-volume framework. *Ocean Modell.* 81, 49–64.
- 1747 Knight, P.J., Howarth, M.J., Rippeth, T.P., 2002. Inertial currents in the Northern North Sea. *J. Sea Res.*
1748 47, 269–284.
- 1749 Kondo, J., 1975. Air-sea bulk transfer coefficients in diabatic conditions. *Bound. Layer Meteor.* 9, 91–112.
- 1750 Lahaye, S., Gouillon, F., Baraille, R., Pichon, A., Pineau-Guillou, L., Morel, Y., 2011. A numerical scheme
1751 for modeling tidal wetting and drying. *J. Geophys. Res.* 116. C03028.
- 1752 Large, W.G., McWilliams, J.C., Doney, S.C., 1994. Oceanic vertical mixing: a review and a model with
1753 nonlocal boundary layer parameterisation. *Rev. Geophys.* 32, 363–403.
- 1754 Lazure, P., Salomon, J.C., 1991. Coupled 2-d and 3-d modeling of coastal hydrodynamics. *Oceanol. Acta*
1755 14, 173–180.
- 1756 Leclair, M., Madec, G., 2011. \tilde{z} -coordinate, an arbitrary lagrangian-eulerian coordinate separating high
1757 and low frequency motions. *Ocean Modell.* 37, 139–152.
- 1758 Lemarié, F., Debreu, L., Madec, G., Demange, J., Molines, J., Honnorat, M., 2015. Stability constraints
1759 for oceanic numerical models: implications for the formulation of time and space discretizations. *Ocean*
1760 *Modell.* 92, 124–148.
- 1761 Lemarié, F., Debreu, L., Shchepetkin, A., McWilliams, J., 2012a. On the stability and accuracy of the
1762 harmonic and biharmonic isoneutral mixing operators in ocean models. *Ocean Modell.* 52-53, 9–35.
- 1763 Lemarié, F., Kurian, J., Shchepetkin, A.F., Molemaker, M.J., Colas, F., McWilliams, J.C., 2012b. Are
1764 There Inescapable Issues Prohibiting the use of Terrain-Following Coordinates in Climate Models ?
1765 *Ocean Modell.* 42, 57–79.
- 1766 Lenhart, H.J., Mills, D.K., Baretta-Bekker, H., Van Leeuwen, S.M., Van Der Molen, J., Baretta, J.W.,
1767 Blaas, M., Desmit, X., Kühn, W., Lacroix, G., et al., 2010. Predicting the consequences of nutrient
1768 reduction on the eutrophication status of the North Sea. *J. Mar. Syst.* 81, 148–170.
- 1769 Lilly, D.K., 1965. On the computational stability of numerical solutions of time-dependent non-linear
1770 geophysical fluid dynamics problems. *Mon. Wea. Rev.* 93, 11–25.
- 1771 Lin, S.J., 1997. A finite-volume integration method for computing pressure gradient force in general
1772 vertical coordinates. *Quart. J. Roy. Meteorol. Soc.* 123, 1749–1762.
- 1773 Lorenz, E.N., 1960. Energy and Numerical Weather Prediction. *Tellus* 12, 364–373.
- 1774 Lotze, H.K., Lenihan, H.S., Bourque, B.J., Bradbury, R.H., Cooke, R.G., Kay, M.C., Kidwell, S.M., Kirby,
1775 M.X., Peterson, C.H., Jackson, J.B.C., 2006. Depletion, degradation, and recovery potential of estuaries
1776 and coastal seas. *Science* 312, 1806–1809.
- 1777 Lundquist, K.A., Chow, F.K., Lundquist, J.K., 2010. An immersed boundary method for the weather
1778 research and forecasting model. *Mon. Wea. Rev.* 138, 796–817.
- 1779 Luyten, P., Jones, J., Proctor, R., Tabor, A., Tett, P., Wild-Allen, K., 1999. COHERENS - A coupled

- 1780 hydrodynamical-ecological model for regional and shelf seas: User Documentation. Technical Report.
1781 MUMM Report, Management Unit of the Mathematical Models of the north Sea.
- 1782 MacCready, P., Geyer, W.R., 2010. Advances in estuarine physics. *Annu. Rev. Fluid Mech.* 2, 35–58.
- 1783 Madala, R.V., Piacsek, S.A., 1977. A semi-implicit numerical model for baroclinic oceans. *J. Comp. Phys.*
1784 23, 167–178.
- 1785 Madec, G., Delecluse, P., Crepon, M., Chartier, M., 1991. A three-dimensional numerical study of deep-
1786 water formation in the northwestern mediterranean sea. *J. Phys. Oceanogr.* 21, 1349–1371.
- 1787 Marchesiello, P., Debreu, L., Couvelard, X., 2009. Spurious diapycnal mixing in terrain-following coor-
1788 dinate models: The problem and a solution. *Ocean Modell.* 26, 159–169.
- 1789 Marchesiello, P., McWilliams, J.C., Shchepetkin, A., 2001. Open boundary conditions for long-term
1790 integration of regional oceanic models. *Ocean Modell.* 3, 1–20.
- 1791 Marsaleix, P., Auclair, F., Estournel, C., Nguyen, C., Ulses, C., 2011. An accurate implementation of
1792 the compressibility terms in the equation of state in a low order pressure gradient scheme for sigma
1793 coordinate ocean models. *Ocean Modell.* 40, 1–13.
- 1794 Marsaleix, P., Auclair, F., Floor, J.W., Herrmann, M.J., Estournel, C., Pairaud, I., Ulses, C., 2008. Energy
1795 conservation issues in sigma-coordinate free-surface ocean models. *Ocean Modell.* 20, 61–89.
- 1796 Marsaleix, P., Estournel, C., Kondrachoff, V., Vehil, R., 1998. A numerical study of the formation of the
1797 Rhône River plume. *J. Marine Syst.* 14, 99–115.
- 1798 Marshall, J., Hill, C., Perelman, L., Adcroft, A.J., 1997. Hydrostatic, quasi-hydrostatic, and nonhydrostatic
1799 ocean modeling. *Journal of Geophysical Research* 102 (C3), 5733–5752.
- 1800 Martin, P.J., 1985. Simulation of the mixed layer at OWS November and Papa with several models. *J.*
1801 *Geophys. Res.* 90, 903–916.
- 1802 Martin, P.J., 2000. Description of the Navy Coastal Ocean Model Version 1.0. Technical Report. NRL
1803 Report.
- 1804 Martinho, A.S., Batteen, M.L., 2006. On reducing the slope parameter in terrain-following numerical
1805 ocean models. *Ocean Modell.* 13, 166–175.
- 1806 Martins, F., Leitão, P., Silva, A., Neves, R., 2001. 3D modeling in the Sado estuary using a new generic
1807 vertical discretization approach. *Oceanologica Acta* 24, S51–S62.
- 1808 Martinsen, E.A., Engedahl, H., 1987. Implementation and testing of a lateral boundary scheme as an open
1809 boundary condition in a barotropic ocean model. *Coast. Eng.* 11, 603–627.
- 1810 Mason, E., Molemaker, J., Shchepetkin, A.F., Colas, F., McWilliams, J.C., Sangrà, P., 2010. Procedures
1811 for offline grid nesting in regional ocean models. *Ocean Modell.* 35, 1–15.
- 1812 Mathis, M., Elizalde, A., Mikolajewicz, U., Pohlmann, T., 2015. Variability patterns of the general circu-
1813 lation and sea water temperature in the North Sea. *Progr. Oceanogr.* 135, 91–112.
- 1814 McCalpin, J.D., 1994. A comparison of second-order and fourth-order pressure gradient algorithms in a
1815 σ -coordinate ocean model. *Int. J. Numer. Meth. Fl.* 18, 361–383.
- 1816 Meier, H.E.M., Kjellström, E., Graham, L.P., 2006. Estimating uncertainties of projected Baltic Sea salin-
1817 ity in the late 21st century. *Geophys. Res. Lett.* 33(15), 10.1029/2006GL026488.
- 1818 Mellor, G.L., 2002. Oscillating bottom boundary layers. *J. Phys. Oceanogr.* 32, 3075–3088.
- 1819 Mellor, G.L., Blumberg, A.F., 1985. Modeling vertical and horizontal diffusivities with the sigma coordi-
1820 nate system. *Mon. Wea. Rev.* 113, 1379–1383.
- 1821 Mellor, G.L., Ezer, T., Oey, L.Y., 1994. The pressure gradient conundrum of sigma coordinate ocean
1822 models. *J. Atmos. Ocean. Technol.* 11, 1126–1134.
- 1823 Mellor, G.L., Yamada, T., 1982. Development of a turbulence closure model for geophysical fluid prob-
1824 lems. *Rev. Geophys.* 20, 851–875.

- 1825 Mesinger, F., Arakawa, A., 1976. Numerical Methods used in atmospheric models, vol. 1. Technical
1826 Report. World Meteor. Org. GARP Publ. Ser. 17.
- 1827 Mohammadi-Aragh, M., Klingbeil, K., Brüggemann, N., Eden, C., Burchard, H., 2015. The impact of
1828 advection schemes on restratification due to lateral shear and baroclinic instabilities. *Ocean Modell.* 94,
1829 112–127.
- 1830 Nataf, F., 2013. Absorbing boundary conditions and perfectly matched layers in wave propagation prob-
1831 lems. *Direct and Inverse problems in Wave Propagation and Applications* 14, 219–231.
- 1832 Neumann, T., Fennel, W., Kremp, C., 2002. Experimental simulations with an ecosystem model
1833 of the Baltic Sea: a nutrient load reduction experiment. *Global Biogeochemical Cycles* 16,
1834 10.1029/2001GB001450.
- 1835 Nicholls, R.J., Hoozemans, F.M.J., Marchand, M., 1999. Increasing flood risk and wetland losses due to
1836 global sea-level rise: regional and global analyses. *Global Environmental Change* 9, S69–S87.
- 1837 Nihoul, J.C., Waleffe, F., Djenidi, S., 1986. A 3d-numerical model of the northern bering sea. *Environ-*
1838 *mental Software* 1, 76–81.
- 1839 O’Dea, E.J., Arnold, A.K., Edwards, K.P., Furner, R., Hydler, P., Martin, M.J., Siddorn, J.R., Storkey,
1840 D., While, J., Holt, J.T., Liu, H., 2012. An operational ocean forecast system incorporating NEMO
1841 and SST data assimilation for the tidally driven European North-West shelf. *Journal of Operational*
1842 *Oceanography* 5, 3–17.
- 1843 Oey, L.Y., 2005. A wetting and drying scheme for POM. *Ocean Modell.* 9, 133–150.
- 1844 Olbers, D., Willebrand, J., Eden, C., 2012. *Ocean dynamics*. Springer-Verlag Berlin Heidelberg.
- 1845 Olinger, J., Sundström, A., 1978. Theoretical and practical aspects of some initial boundary value problems
1846 in fluid dynamics. *SIAM J. Appl. Math.* 35, 419–446.
- 1847 Orlandi, I., 1976. A simple boundary condition for unbounded hyperbolic flows. *J. Comput. Phys.* 21,
1848 251–269.
- 1849 Oschlies, A., 2002. Improved representation of upper ocean dynamics and mixed layer depths in a model
1850 of the North Atlantic on switching from eddy-permitting to eddy-resolving grid resolution. *J. Phys.*
1851 *Oceanogr.* 32, 2277–2298.
- 1852 Palma, E.D., Matano, R.P., 2000. On the implementation of open boundary conditions for a general
1853 circulation model: The three-dimensional case. *J. Geophys. Res.* 105, 8605–8627.
- 1854 Patankar, S.V., 1980. *Numerical Heat Transfer and Fluid Flow*. McGraw-Hill, New York.
- 1855 Paulson, C.A., Simpson, J.J., 1977. Irradiance measurements in the upper ocean. *J. Phys. Oceanogr.* 7,
1856 952–956.
- 1857 Peaceman, D.W., Rachford, Jr., H.H., 1955. The numerical solution of parabolic and elliptic differential
1858 equations. *SIAM Journal* 3, 28–41.
- 1859 Pearson, B., Fox-Kemper, B., Bachman, S., Bryan, F., 2017. Evaluation of scale-aware subgrid mesoscale
1860 eddy models in a global eddy-rich model. *Ocean Modelling* 115, 42–58.
- 1861 Penven, P., Debreu, L., Marchesiello, P., McWilliams, J.C., 2006. Evaluation and application of the roms
1862 1-way embedding procedure to the central california upwelling system. *Ocean Modell.* 12, 157–187.
- 1863 Perkins, A.L., Smedstad, L.F., Blake, D.W., Heburn, G.W., Wallcraft, A.J., 1997. A new nested boundary
1864 condition for a primitive equation ocean model. *J. Geophys. Res.* 102, 3483–3500.
- 1865 Pietrzak, J., Jakobson, J.B., Burchard, H., Vested, H.J., Petersen, O., 2002. A three-dimensional hydrostatic
1866 model for coastal and ocean modelling using a generalised topography following co-ordinate system.
1867 *Ocean Modell.* 4, 173–205.
- 1868 Quante, M., Colijn, F. (Eds.), 2016. *North Sea Region Climate Change Assessment*. Springer.
- 1869 Raymond, W.H., Kuo, H.L., 1984. A radiation boundary condition for multi-dimensional flows. *Q.J.R.*

- 1870 Meteorol. Soc. 110, 535–551.
- 1871 Rennau, H., Schimmels, S., Burchard, H., 2012. On the effect of structure-induced resistance and mixing
1872 on inflows into the Baltic Sea: a numerical model study. *Coastal Engineering* 60, 53–68.
- 1873 Rippeth, T.P., Fisher, N., Simpson, J.H., 2001. The semi-diurnal cycle of turbulent dissipation in the
1874 presence of tidal straining. *J. Phys. Oceanogr.* 31, 2458–2471.
- 1875 Rodi, W., 1987. Examples of calculation methods for flow and mixing in stratified flows. *J. Geophys. Res.*
1876 92, 5305–5328.
- 1877 Roquet, F., Madec, G., McDougall, T.J., Barker, P.M., 2015. Accurate polynomial expressions for the
1878 density and specific volume of seawater using the TEOS-10 standard. *Ocean Modell.* , 29–43.
- 1879 Ross, M.A., Mehta, A.J., 1989. On the mechanics of lutoclines and fluid mud. *J. Coastal Res.* , 51–62.
- 1880 Rueda, F.J., Sanmiguel-Rojas, E., Hodges, B.R., 2007. Baroclinic stability for a family of two-level,
1881 semi-implicit numerical methods for the 3d shallow water equations. *Int. J. Numer. Meth. Fluids* 54,
1882 237–268.
- 1883 Schär, C., Leuenberger, D., Fuhrer, O., Lüthi, D., Girard, C., 2002. A new terrain-following vertical
1884 coordinate formulation for atmospheric prediction models. *Mon. Wea. Rev.* 130, 2459–2480.
- 1885 Scotti, A., Pineda, J., 2004. Observation of very large and steep internal waves of elevation near the
1886 Massachusetts coast. *Geophys. Res. Lett.* 31, 10.1029/2004GL021052.
- 1887 Screen, J.A., Simmonds, I., 2010. The central role of diminishing sea ice in recent Arctic temperature
1888 amplification. *Nature* 464, 1334–1337.
- 1889 Shapiro, G., Luneva, M., Pickering, J., Storkey, D., 2013. The effect of various vertical discretization
1890 schemes and horizontal diffusion parameterization on the performance of a 3-d ocean model: the black
1891 sea case study. *Ocean Sci.* 9(2), 377–390.
- 1892 Shchepetkin, A.F., 2015. An adaptive, courant-number-dependent implicit scheme for vertical advection
1893 in oceanic modeling. *Ocean Modell.* 91, 38–69.
- 1894 Shchepetkin, A.F., McWilliams, J.C., 2003. A method for computing horizontal pressure-gradient force
1895 in an oceanic model with a non-aligned vertical coordinate. *J. Geophys. Res.* 108 (C3), 3090–3124.
- 1896 Shchepetkin, A.F., McWilliams, J.C., 2005. The Regional Oceanic Modeling System: A split-explicit,
1897 free-surface, topography-following-coordinate ocean model. *Ocean Modell.* 9, 347–404.
- 1898 Shchepetkin, A.F., McWilliams, J.C., 2009a. Computational kernel algorithms for fine-scale, multiprocess,
1899 longtime oceanic simulations, in: Ciarlet, P.G. (Ed.), *Computational methods for the atmosphere and the
1900 oceans Special Volume*. Elsevier. volume XIV of *Handbook of numerical analysis*, pp. 121–183.
- 1901 Shchepetkin, A.F., McWilliams, J.C., 2009b. Correction and commentary for "ocean forecasting in terrain-
1902 following coordinates: Formulation and skill assessment of the regional ocean modeling system" by
1903 Haidvogel et al., *J. Comp. Phys.* 227, pp. 3595-3624. *J. Comput. Phys.* 228, 8985–9000.
- 1904 Sheng, J., Greatbatch, R.J., Zhai, X., Tang, L., 2005. A new two-way nesting technique for ocean modeling
1905 based on the smoothed semi-prognostic method. *Ocean Dyn.* 55, 162–177.
- 1906 Shu, C.W., 1987. TVB uniformly high-order accurate schemes for conservation laws. *Math. Comput.* 49,
1907 105–121.
- 1908 Shu, C.W., 1988. Total-variation-diminishing time discretizations. *SIAM J. Sci. Stat. Comput.* 9, 1073–
1909 1084.
- 1910 Simons, T.J., 1974. Verification of Numerical Models of Lake Ontario: Part I. Circulation in Spring and
1911 Early Summer. *Journal of Physical Oceanography* 4, 507–523.
- 1912 Simpson, J.H., Brown, J., Matthews, J., Allen, G., 1990. Tidal straining, density currents, and stirring in
1913 the control of estuarine stratification. *Estuaries* 13, 125–132.
- 1914 Smagorinsky, J., 1963. General circulation experiments with the primitive equations. *Mon. Wea. Rev.* 91,

- 1915 99–164.
- 1916 Smyth, W.D., Skillingstad, E.D., Crawford, G.B., Wijesekera, H., 2002. Nonlocal fluxes and stokes drift
1917 effects in the K -profile parameterization. *Ocean Dyn.* 52, 104–115.
- 1918 Song, Y., Haidvogel, D.B., 1994. A semi-implicit ocean circulation model using a generalised topography-
1919 following coordinate. *J. Comput. Phys.* 115, 228–244.
- 1920 Soufflet, Y., Marchesiello, P., Lemarié, F., Jouanno, J., Capet, X., Debreu, L., Benshila, R., 2016. On
1921 effective resolution in ocean models. *Ocean Modell.* 98, 36–50.
- 1922 Starr, V.P., 1945. A quasi-lagrangian system of hydrodynamical equations. *Journal of Meteorology* 2,
1923 227–237.
- 1924 Stelling, G.S., Duinmeijer, S.P.A., 2003. A staggered conservative scheme for every Froude number in
1925 rapidly varied shallow water flows. *Int. J. Numer. Meth. Fluids* 43, 1329–1354.
- 1926 Stelling, G.S., Van Kester, J.A.T.M., 1994. On the approximation of horizontal gradients in sigma co-
1927 ordinates for bathymetry with steep bottom slopes. *Int. J. Numer. Methods Fluids* 18, 915–935.
- 1928 Stockdon, H.F., Holman, R.A., Howd, P.A., Sallenger, A.H., 2006. Empirical parameterization of setup,
1929 swash, and runup. *Coastal Engineering* 53(7), 573–588.
- 1930 Suresh, A., Huynh, H., 1997. Accurate monotonicity-preserving schemes with runge-kutta time stepping.
1931 *J. Comp. Phys.* 136, 83–99.
- 1932 Svendsen, E., Berntsen, J., Skogen, M., dlandsvik, B., Martinsen, E., 1996. Joint numerical sea modelling
1933 model simulation of the skagerrak circulation and hydrography during skagex. *J. Marine Syst.* 8, 219–
1934 236.
- 1935 Sydeman, W.J., García-Reyes, M., Schoeman, D.S., Rykaczewski, R.R., Thompson, S.A., Black, B.A.,
1936 Bograd, S.J., 2014. Climate change and wind intensification in coastal upwelling ecosystems. *Science*
1937 345, 77–80.
- 1938 Témam, R., 1969. Sur l'Approximation de la Solution de Équations de Navier-Stokes par la Méthode de
1939 Pas Fractionnaires (II). *Arch. Rational Mech. Anal.* 32, 377–385.
- 1940 Témam, R., Tribbia, J., 2003. Open boundary conditions for the primitive and boussinesq equations. *J.*
1941 *Atmos. Sci.* 60, 2647–2660.
- 1942 Uchiyama, Y., McWilliams, J.C., Shchepetkin, A.F., 2010. Wave-current interaction in an oceanic circula-
1943 tion model with a vortex-force formalism: Application to the surf zone. *Ocean Modell.* 34, 16–35.
- 1944 Umlauf, L., Burchard, H., 2003. A generic length-scale equation for geophysical turbulence models. *J.*
1945 *Mar. Res.* 61, 235–265.
- 1946 Umlauf, L., Burchard, H., 2005. Second-order turbulence models for geophysical boundary layers. A
1947 review of recent work. *Cont. Shelf Res.* 25, 795–827.
- 1948 Van Maren, D.S., Oost, A.P., Wang, Z.B., Vos, P.C., 2016. The effect of land reclamations and sediment
1949 extraction on the suspended sediment concentration in the ems estuary. *Mar. Geol.* 376, 147–157.
- 1950 Vitousek, S., Fringer, O., 2011. Physical vs numerical dispersion in nonhydrostatic ocean modeling. *Ocean*
1951 *Modell.* 40, 72–86.
- 1952 Wahl, T., Haigh, I.D., Woodworth, P.L., Albrecht, F., Dillingh, D., Jensen, J., Nicholls, R.J., Weisse, R.,
1953 Wöppelmann, G., 2013. Observed mean sea level changes around the North Sea coastline from 1800 to
1954 present. *Earth-Science Reviews* 124, 51–67.
- 1955 Waldron, K.M., Paegle, J., Horel, J.D., 1996. Sensitivity of a spectrally filtered and nudged limited-area
1956 model to outer model options. *Mon. Wea. Rev.* 124, 529–547.
- 1957 Walters, R.A., Lane, E.M., Hanert, E., 2009. Useful time-stepping methods for the Coriolis term in a
1958 shallow water model. *Ocean Modell.* 28, 66–74.
- 1959 Wang, S., Dieterich, C., Döscher, R., Höglund, A., Hordoir, R., Meier, H.E.M., Samuelsson, P., Schimanke,

- 1960 S., 2015. Development and evaluation of a new regional coupled atmosphere-ocean model in the North
1961 Sea and Baltic Sea. *Tellus A* 67, 10.3402/tellusa.v67.24284.
- 1962 Warner, J.C., Defne, Z., Haas, K., Arango, H.G., 2013. A wetting and drying scheme for ROMS. *Com-*
1963 *puters & Geosci.* 58, 54–61.
- 1964 Warner, J.C., Sherwood, C.R., Arango, H.G., Signell, R.P., 2005. Performance of four turbulence closure
1965 models implemented using a generic length scale method. *Ocean Modell.* 8, 81–113.
- 1966 Warner, J.C., Sherwood, C.R., Signell, R.P., Harris, C.K., Arango, H.G., 2008. Development of a three-
1967 dimensional, regional, coupled wave, current, and sediment-transport model. *Computers & Geosci.* 34,
1968 1284–1306.
- 1969 Weller, H., Shahrokhi, A., 2014. Curl-free pressure gradients over orography in a solution of the fully
1970 compressible euler equations with implicit treatment of acoustic and gravity waves. *Mon. Wea. Rev.*
1971 142, 4439–4457.
- 1972 Wheless, G.H., Klinck, J.M., 1995. The evolution of density-driven circulation over sloping bottom to-
1973 pography. *J. Phys. Oceanogr.* 25, 888–901.
- 1974 White, L., Adcroft, A., Hallberg, R., 2009. High-order regridding-remapping schemes for continuous
1975 isopycnal and generalized coordinates in ocean models. *J. Comput. Phys.* 228, 8665–8692.
- 1976 White, L., Adcroft, A.J., 2008. A high-order finite volume remapping scheme for nonuniform grids: The
1977 piecewise quartic method (PQM). *J. Comput. Phys.* 227, 7394–7422.
- 1978 Wilcox, D.C., 1998. *Turbulence Modeling for CFD*. DCW Industries. 2 edition.
- 1979 Wilkin, J.L., Arango, H.G., Haidvogel, D.B., Lichtenwalner, C., Glenn, S.M., Hedström, K.S., 2005. A
1980 regional ocean modeling system for the long-term ecosystem observatory. *J. Geophys. Res.* 110.
- 1981 Wiltshire, K.H., Manly, B.F.J., 2004. The warming trend at Helgoland Roads, North Sea: phytoplankton
1982 response. *Helgol. Mar. Res.* 58, 269–273.
- 1983 Winterwerp, J.C., Wang, Z.B., van Braeckel, A., van Holland, G., Kösters, F., 2013. Man-induced regime
1984 shifts in small estuariesII: a comparison of rivers. *Ocean Dyn.* 63, 1293–1306.